SOCIAL RECOGNITION

AND TRANSCRIPTOMIC CELL TYPES

IN THE DEVELOPING ZEBRAFISH VISUAL SYSTEM

Johannes Maximilian Kappel

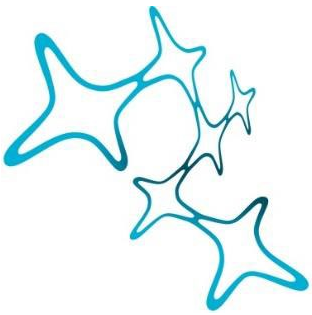

Graduate School of
Systemic Neurosciences
LMU Munich

Dissertation der
Graduate School of Systemic Neurosciences der
Ludwig-Maximilians-Universität München
28. April 2023

Supervisor
Prof. Dr. Herwig Baier
Genes – Circuits – Behavior
Max Planck Institute for Biological Intelligence

First Reviewer: Prof. Dr. Herwig Baier
Second Reviewer: Prof. Dr. Alexander Borst
Third Reviewer: Prof. Dr. Philip Washbourne

Date of Submission: 28.04.23
Date of Defense: 27.11.23

Summary

The foundations of our everyday experience and the experience of any animal lie in the structure and function of the underlying sensory systems in the brain that selectively extract and profoundly filter information from our environment, being it a ray of light, a sound wave or an odorant particle. Sensory neural networks evolved over hundreds of millions of years, from unicellular organisms that sense light gradients to human visual cortex with billions of neurons and trillions of synaptic connections. Like any biological system, sensory brain networks comprise emergent properties: The selective transcription of a gene combination in an individual neuron results in a cell morphology that is suited for filtering motion direction; a network of neurons that combine their filter properties generate adaptive behavioral responses to environmental stimuli. Here, I present two studies that uncover fundamental workings of the visual system in developing zebrafish on two levels of emergence. In the first study, I identified a neuronal circuit for selective recognition of social visual signals that is essential for social behavior in the juvenile zebrafish thalamus. By using a combination of brain-wide activity mapping and large-scale volumetric two-photon imaging, I pinpointed a cluster of thalamic neurons that exhibited selective activation to social motion cues. Upon ablation of these cells, animals lost social attraction. Anatomical reconstruction of this nucleus revealed that upstream information comes from the tectum, the major hub for sensorimotor transformation. In the second study, I investigated how transcriptomic cell types give rise to functional cell types in the tectum. I connected functional and transcriptomic identities on a single-cell level in intact brain tissues by combining functional imaging and high-resolution *in situ* RNA labeling. I investigated the functional profiles of transcriptomically identified neurons by combining hierarchical clustering, dimensionality reduction and non-linear classification algorithms. Neurons from the same transcriptomic type responded preferentially to specific combinations of stimuli based on their anatomical localization, indicating that positional information drives phenotypic diversity in transcriptomic cell types of the tectum. Together, these studies provide fundamental examples for the functional organization of the vertebrate brain, from transcriptomic cell types to sensation and from sensory circuits to social behavior.

Contents

1. Introduction

1.1 The neural basis of social behaviors

Social behaviors exist in all sexually reproducing species. They are either conciliatory or antagonistic and existential for the health, survival, and reproduction of animal and manifest at multiple scales, from casual conversations between two humans to social hierarchies in insect colonies to collective dynamics in flocks of birds. Across these scales, brains of individual animals mediate social behaviors, instructing interactions between two or more conspecifics.

Such interactions are inherently complex due to many variables within interaction partners such as behavioral state or social rank: For instance, an encounter with a mouse pup can evoke either brood care or infanticide in a male mouse, depending on the internal state (Elwood and Stolzenberg, 2020). Social stimuli from conspecifics can are complex and multisensory, including auditory or olfactory communication, visual non-verbal body communication or touch. Traditional schemes of brain function as a feed forward transformation of a sensory stimulus into a behavioral response are often not applicable for the neural basis of social behaviors. Here, two or more animals, interact with each other through behavior and thus form a feedback loop (Chen and Hong, 2018, Fig. 1A). In this loop, decision-making processes in the brain must factor in past behaviors of both interaction partners to generate adaptive behavioral outcomes. This leads to ambiguity about the experimental inference of causal links between a social stimulus and the behavioral response: Is the behavior from one animal a causal stimulus for the following behavior from the conspecific partner or are both behaviors elicited by yet another behavioral event earlier in the interaction (Fig. 1B)? The computational complexity of untangling this ambiguity warrants the hypothesis that nervous systems have adapted to enable social interactions. One evolutionary adaptation to social behaviors in the brain could be the emergence of one ore multiple specialized brain regions that are dedicated to mediating interactions with conspecifics. Indeed, a set of homologous brain regions in the limbic system, first identified in rodents, is involved in mediating multiple social behaviors (Newman, 1999).

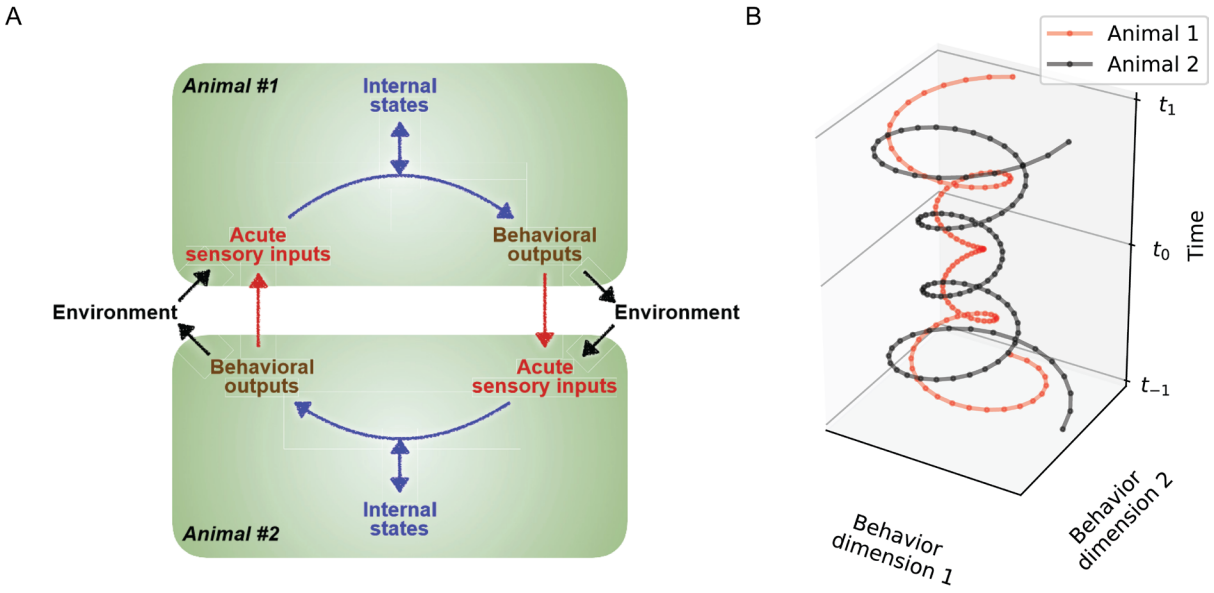

Figure 1: Complexity of social interactions

(A) Schematic visualizing the reciprocal feedback loop in a social interaction between two animals. Conspecific sensory information detected by the other individual triggers an adaptive behavioral response. The response in turn generates sensory cues for the other individual, perpetuating the loop. Adapted with permission (Chen and Hong, 2018).

(B) Schematic trajectories of two interacting animals through a 2-dimensional behavioral space. At a certain point in time t_1, the current behavioral state of one animal could be the result of the individual or combined behavioral states at t_0 or t_{-1}.

This network of brain nodes is formed by the medial amygdala (MeA), medial bed nucleus of stria terminalis (mBNST), lateral septum (LS), anterior hypothalamus (AH), ventromedial hypothalamus (VMH), preoptic area (POA) and the periaqueductal gray (PAG). In rodents, by definition, neurons within these nuclei harbor gonadal hormone receptors, their activity is modulated by social interactions and these nodes were shown to be functionally interconnected. Initial lesion studies established that individual nodes of the so-called social behavior network (SBN) are necessary for mediating different social behaviors such as female sexual behavior, aggression, territorial marking, and maternal behavior. The initial overarching hypothesis was that differential activity of the individual nodes of the network collectively mediates all social behaviors (Fig. 2A). Goodson, O'Connell and Hofmann extended the SBN hypothesis to the five main vertebrate lineages based

on connectivity and neurochemical findings (Goodson, 2005; O'Connell and Hofmann, 2012). Further, the mesolimbic reward system consisting of the ventral tegmental area, basolateral amygdala, nucleus accumbens, striatum, hippocampus and ventral pallidum was described as an evolutionary conserved network connected to the SBN, and, in combination, these two systems were named social decision-making network (SDM-N) (O'Connell and Hofmann, 2012). While the SBN and SDM-N have been useful frameworks to promote the idea of a network of homologous nodes for social behaviors across vertebrates, the lack of cellular resolution in the evidence, the unclear application of criteria to qualify as a node across taxa and other factors make the models less nuanced and less applicable to circuit-level questions (Kelly, 2022).

One open question is whether the same neuronal pathways in SBN nodes perform computations for mediating multiple social behaviors or, alternatively, separate more specific pathways work in parallel (Fig. 2B). Consider a male mouse meeting an adult conspecific in an open field: Depending on the opposite sex, the male mouse might either attack the opponent or engage in mating behavior. In one scenario, the same set of neurons would mediate the overall decision to engage socially with any conspecific, while parallel, separate circuits would command the respective behaviors, attack or mate. Alternatively, completely different sets of neurons that are intermingled in the same brain structures decide on social engagement and the entailing sex-specific behaviors, attack or mate.

While specific anatomical structures of many vertebrate brains govern multiple social behaviors, it is still unclear to which extent there is a division of labor on the circuit level for social behaviors (Fig. 2B). In the brain of the fruit fly *Drosophila melanogaster*, P1^{a} neurons promote both aggression and mating through the elevation of a social state (Hoopfer et al., 2015), suggesting a convergent node for neural control of social behavior (Fig. 2B). Support for parallel channels comes from studies of aggression circuits in the ventrolateral subdivision of the ventromedial hypothalamus (VMHvl) in rodents (Lin et al., 2011). A large body of work implicate VMHvl neurons that contain estrogen (ESR)- and progesterone-receptors in both aggression and mating (Anderson, 2016) (Fig. 2C). Yet, activation of the individual transcriptomic cell types within this brain area could not confirm a causal effect of a single cell type on multiple social behaviors (Liu et al., 2022).

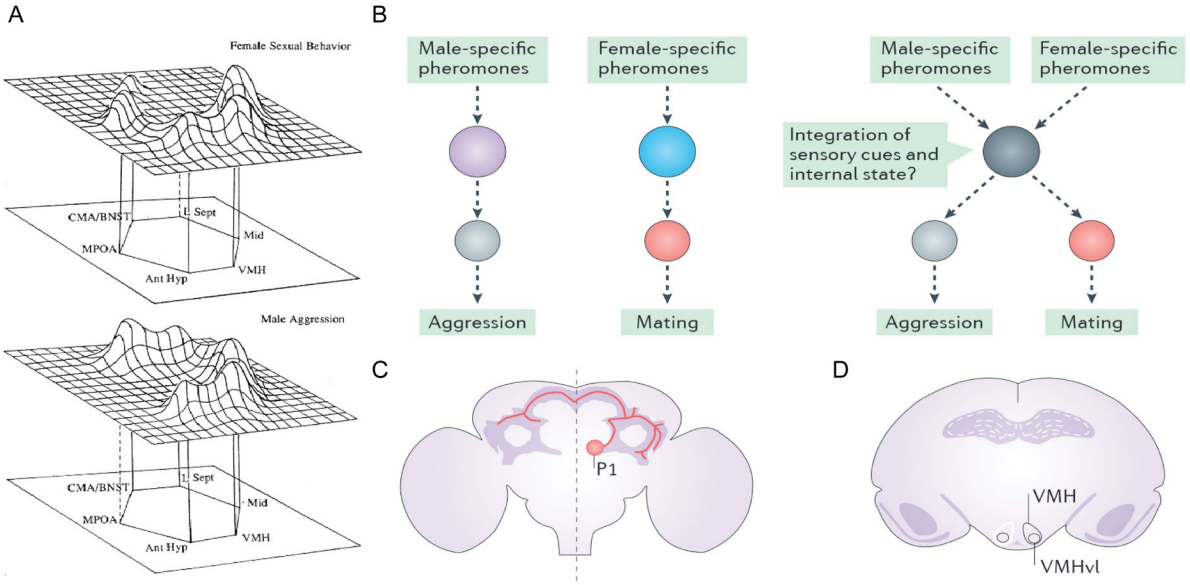

Figure 2: Network models for regulation of social behaviors

(A) The social behavior network (SBN) consists of six nodes and is thought to mediate multiple social behaviors through differential activity within nodes. Adapted with permission (Newman, 1999).

(B) Two extreme layouts of circuit architecture for mediating two social behaviors, mating and aggression. Left: Individual circuits for mating and aggression do not share any connectivity or nodes except for reciprocal inhibition. Right: Neural pathways for mating and aggression converge onto a common node that controls both behaviors. B-D adapted with permission (Anderson, 2016).

(C) A homogeneous set of anatomically and molecularly defined neurons in the Drosophila brain termed P1 cluster has shared functionality for both mating and aggression behavior.

(D) Location of the ventrolateral subdivision of the ventromedial hypothalamus (VMHvl) in mice. Individual neurons in this region either trigger sexual or aggression behavior.

1.2 Role of neocortex

While the subcortical brain areas of the SBN are in focus of social behavior research, the role of the pallium - and in mammals, reptiles and birds especially neocortex - in social behavior and decision-making is a prevailing topic. The social brain hypothesis therefore proposes group living as the main driver of the evolutionary expansion of the neocortex (Byrne, 1996; Dunbar and Shultz, 2007) to meet the computational demands that come with constant social interaction. Astonishingly, relative neocortex volume strongly correlates with group size in monkeys and apes, though alternative explanations for this link are possible (Dunbar and Shultz, 2007). More specifically,

numerous studies have pointed at the ventromedial prefontal cortex (vmPFC) as important for social decision-making, planning and other social cognitive tasks in mice, monkeys and humans (Adolphs, 1999; Báez-Mendoza et al., 2021; Franklin et al., 2017; Grossman et al., 2022; Krueger et al., 2009; Milne and Grafman, 2001; Murugan et al., 2017; Zhao et al., 2022). From vmPFC, top-down control is exerted through projections into PAG, amygdala, nucleus accumbens and other nodes of the SBN and SDM-N.

1.3 The sensory basis of social behaviors

Conspecific animals release a multitude of high-dimensional sensory stimuli. Mating dances, vocalizations, pheromones or aggressive displays are just a few of the many ways in which animals communicate (Fig. 3). While central circuits for social behaviors are widely studied, less is known to what extent sensory systems in animal brains are adapted to processing conspecific sensory information in dedicated circuits.

Classically, the relationship between a (sensory) neuron and an environmental stimulus is described through the concept of the receptive field. This framework was coined by Sherrington to describe a patch of skin that evokes a specific behavioral reflex (Sherrington, 1906). Hartline extended this concept to the stimulus location in visual space that evokes activity in retinal ganglion cells (Hartline, 1938). Work from Hubel and Wiesel pioneered the investigation of more complex, orientation- and direction-selective receptive fields in neurons of the cat primary visual cortex area V1 (Hubel and Wiesel, 1962). The concept of neuronal *tuning* to specific sensory features beyond the spatial location of an object has since been commonplace, extending the receptive field to spectral bands within light, shapes or auditory frequencies.

Receptive fields of individual neurons can also be tuned to conspecific features. Few examples from the literature describe different levels of abstraction for the relationship between conspecific stimuli and neuronal tuning:
In the Drosophila visual system, a specific subclass of projection neurons is tuned to object sizes and speeds that match a mate during courtship (Ribeiro et al., 2018).

Activation of these neurons triggers elements of female courtship, indicating that mate-recognition by this circuit might be sufficient to drive behavior. This provides one of the cleanest examples for a dedicated circuit for social recognition and behavior (Ribeiro et al., 2018; Hindmarsh Sten et al., 2021). Cowley and colleagues expand this finding by suggesting that many subclasses of visual projection neurons act as filters for visual features of conspecifics that in combination activate elements of courtship behavior (Cowley et al., 2022) (Fig. 3A). However, the question of specificity remains unclear, i.e. whether subclasses of visual projection neurons solely respond to social features in a natural setting or have additional purposes.
In the mouse medial amygdala (MeA), one node of the SBN, individual neurons as well as ensembles encode conspecific information such as sex and age in an experience-dependent manner (Bergan et al., 2014; Li et al., 2017). In this case, the sensory basis of his representation is well described: Olfactory sensory neurons in the vomeronasal organ express odorant receptors that specifically bind pheromones of conspecifics. These neurons project to the mitral/tufted cells in the accessory olfactory bulb, which in turn connect to MeA (Halpern, 1987; Dulac and Torello, 2003) (Fig. 3B). Thus, dedicated olfactory circuits at the periphery detect pheromones that induce abstract social representations in MeA (Fig. 3C).
One example for visual social processing in vertebrate brains comes from primates, where individual neurons in inferior temporal (IT) cortex respond specifically to faces (Tsao et al., 2003, 2006) (Fig. 3D). This region further harbors a general topographic mapping of representations for animate i.e. living objects versus inanimate objects (Bao et al., 2020).

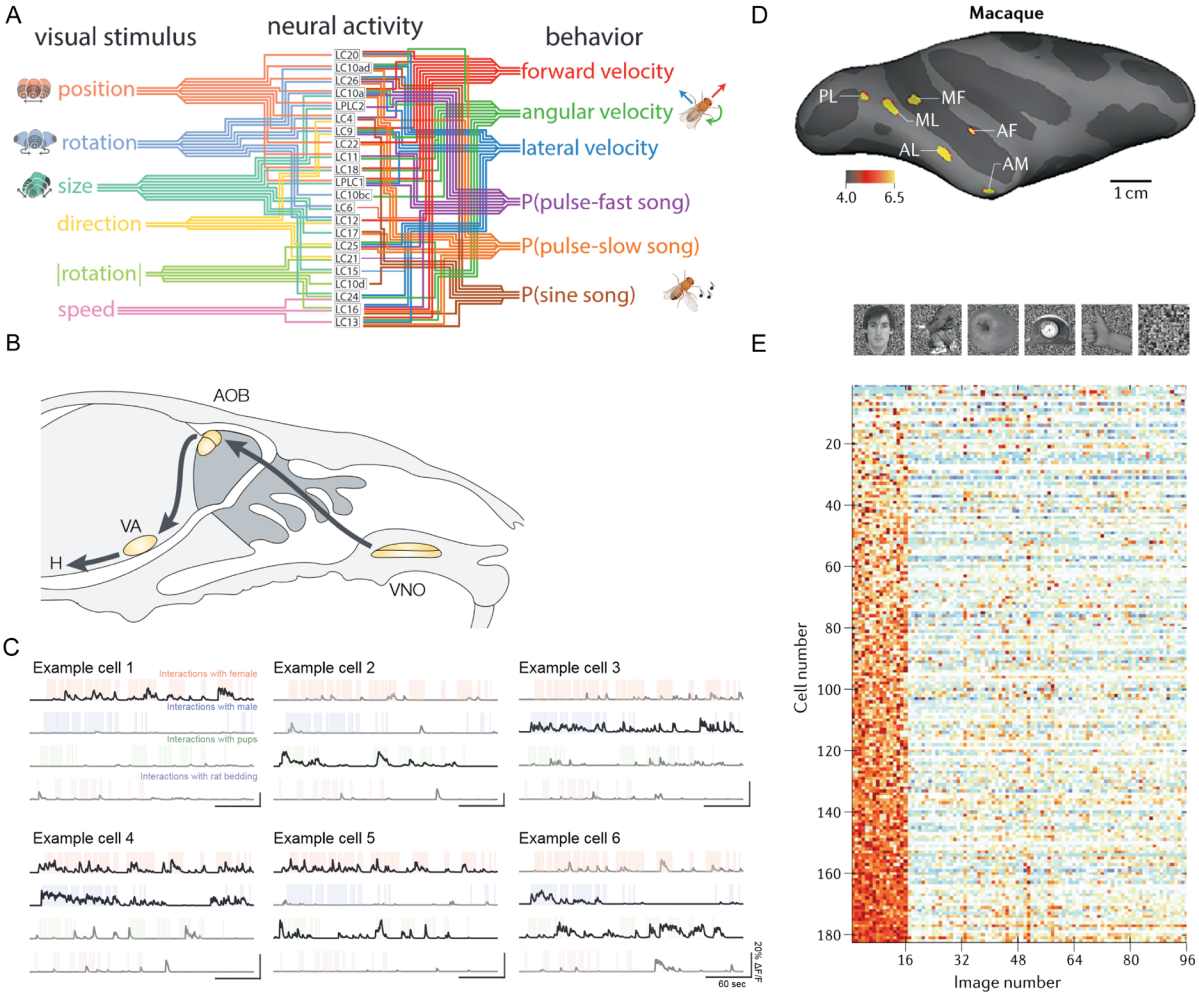

Figure 3: Sensory processing of social cues across species

(A) Combinatorial encoding scheme of conspecific visual cues through lobular columnar (LC) neuron types in the Drosophila lobula and subsequent activation of courtship modules. Adapted with permission (Cowley et al., 2022).

(B) Neural pathway dedicated for recognition of conspecific pheromones in rodents. VNO: Vomeronasal organ, AOB: accessory olfactory bulb, VA: ventral amygdala, H: Hypothalamus. Adapted with permission (Dulac and Torello, 2003).

(C) Example responses of individual medial amygdala neurons to different social cues in the awake mouse. Adapted with permission (Li et al., 2017).

(D) Anatomical location of the face cell patches in monkey IT cortex. Color represents negative common logarithm of the significance value for the fMRI signal for faces versus objects. PI: posterior lateral, ML: middle lateral, MF: middle fundus, AL: anterior lateral, AF: anterior fundus face patches. D-E adapted with permission (Hesse and Tsao, 2020).

(E) Example responses of individual face cells in IT cortex to images of different objects, starting with faces.

The superior temporal sulcus (STS) region, anatomically close to IT cortex, processes biological motion as well as still images of faces and body parts in both humans and primates and is implicated in interpreting actions of conspecifics (Allison et al., 2000). While the face cells in IT cortex are selective for this abstract conspecific feature, it is unclear how this representation mediates social behaviors and how this information gets there.

Together, these studies illustrate different levels of abstraction for the representation of conspecifics. While the mouse VMO is an example of a dedicated structure for olfactory social information, little is known about processing of social visual cues in the early visual system of vertebrate animals and potential connections to circuits that guide social behaviors. Yet, evidence suggests that even humans extract social information from highly reduced visual stimuli: Biological motion is a stimulus that consists of point illumination of body joints that move naturalistically (Johansson, 1973; Neri et al., 1998). This rudimentary body movement devoid of any texture or shape contains sufficient information to extract age, sex and other features in humans (Dittrich et al., 1996; Mather and Murdoch, 1997). This suggests neural circuits in the visual system that extract and classify conspecific motion parameters. Interestingly, biological motion is also a salient visual stimulus in other species, from chicks (Regolin et al., 2000) to developing zebrafish (Larsch and Baier, 2018).

1.4 Zebrafish as a model system for studying social behavior

Zebrafish perform various social behaviors in laboratory settings such as shoaling, aggression, social learning or mating (Geng and Peterson, 2019). These behaviors can be investigated in relatively simple setups using modern tracking algorithms based on computer vision (Lopes and Monteiro, 2021) and deep learning (Romero-Ferrero et al., 2019). The most basic social behavior in zebrafish is the basic drive to move towards conspecifics up to a preferred distance, termed social affiliation or shoaling. This simple distance rule underlies the formation of fish shoals (Katz et al., 2011). Shoaling emerges seven days post fertilization (dpf) and increases during the following two weeks of development (Engeszer et al., 2007; Hinz and de Polavieja, 2017).

Despite this faithful model of the behavior, it is not immediately clear which stimuli trigger social attraction. Social preference assays revealed that adult zebrafish prefer conspecific pigment patterns that they experience on conspecifics during early life (Engeszer et al., 2004) and bind individual visual features of conspecifics such as motion direction and shape into a coherent representation (Neri, 2012). The sight of conspecifics is sufficient to drive social affiliation already in developing zebrafish (Fig 4). Three-week-old juvenile zebrafish stay close conspecifics behind a transparent divider in a U-maze (Dreosti et al., 2015). Of the many possible stimuli emitted by these separated conspecifics, burst-and-glide motion, typical of developing zebrafish, is a sufficient stimulus to drive social affiliation behavior in juvenile zebrafish (Larsch and Baier, 2018). Importantly, the stimulus size and type of motion that triggered the strongest social response matched same-age conspecifics, raising the question whether dedicated visual circuitry for detecting conspecific visual features exists already in developing zebrafish.

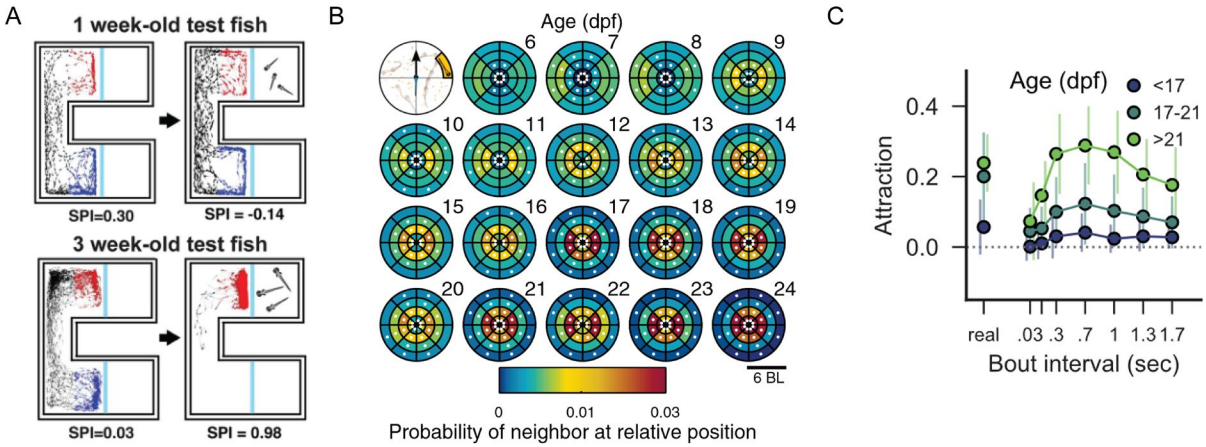

Figure 4: Social behavior emerges during the first three weeks of larval zebrafish development

(A) Juvenile but not larval zebrafish are attracted by the visual display of same-age conspecifics. Positions over time for a 7 dpf and 21 dpf animal in either an empty U-maze or a U-maze with an empty arm and an arm with conspecifics, respectively. SPI: Social preference index. Adapted with permission (Dreosti et al., 2015).

(B) Inter-animal distance gradually decreases during larval zebrafish development. Polar density plots with the focal animal in the center facing upwards for increasing age. Color denotes probability of conspecifics in a certain area with respect to the focal animal. Adapted with permission (Hinz and de Polavieja, 2017).

(C) Behavioral attraction to bout motion emerges in juvenile zebrafish. Attraction is measured as the inverse of inter-animal distance. The bout frequency (interval) is modulated with fixed overall speed. The frequency with maximal behavioral attraction is similar to real frequency of conspecific bout motion. Adapted with permission (Larsch and Baier, 2018).

Past research on circuits underlying social behaviors in fish used *in situ* labelling of immediate early gene expression to identify brain nuclei activated during hierarchy formation in cichlids (Bshary et al., 2014; Maruska et al., 2013). However, developing zebrafish offer a large set of advantages for investigating neuronal circuits for behavior. Short generation cycles with 200-500 eggs per week per female make it feasible to implement genetic tools for recording and controlling activity in populations of neurons (Kawakami et al., 2016). These factors make developing zebrafish an attractive model for investigating circuit mechanisms of social recognition and behavior.

1.5 The structure and function of the larval zebrafish visual system

Light travels to the zebrafish brain through the lens of the eye, thus creating an image on the retina. Visual information is already heavily processed in the outer nuclear layer of the retina: the four different cone types that absorb photons each create a specific color representation of the scene through their spectral tuning (Yoshimatsu et al., 2021). Photoreceptors connect to bipolar cells (BCs) that reside in the inner nuclear layer and combinations of BCs connect with the output cells of the eye, retinal ganglion cells (RGCs). Synaptic connections between photoreceptors, BCs and RGCs give rise to the outer and inner plexiform layer, respectively. Horizontal and amacrine cells modulate the feed-forward pathway by performing various computations at the outer and inner plexiform layer, respectively. In consequence, individual retinal ganglion cells (RGCs) as the output cells of the eye represent highly processed channels of visual information. There are about 50 different morphological RGC types based on stereotyped dendritic and axonal projection patterns, each transmitting subsets of the total visual information to a select subset of the 10 retinal AFs in the zebrafish brain (Robles et al., 2014) (Fig. 5A). This raises the possibility that each morphological type corresponds to a specific visual feature channel. Indeed, early work in toads found that specialized

RGCs in the retina encode visual features of prey objects or predators and in consequence trigger either hunting or escape routines (Ewert, 1987).

Studies in larval zebrafish found similar specializations in the eye: RGCs that innervate the retinal arborization field 7 in the pretectum selectively fire in response to small, prey-like objects and their activity is essential for initiating movements of hunting routines (Antinucci et al., 2019; Semmelhack et al., 2014). A dark looming visual stimulus selectively drives activity in RGCs that innervate AF 6 and AF 8 in the pretectum (Temizer et al., 2015), hinting at dedicated retinal information channels for escape behavior. Another example of an RGC type with a specific role for behavior are transcriptionally defined *eomesa*+ RGCs which are necessary for phototaxis (Kölsch et al., 2021). Similarly, the mouse retina harbours specialized feature detectors for local motion or approaching objects (Münch et al., 2009; Ölveczky et al., 2003).

In zebrafish, individual RGCs broadcast filtered information to multiple 'retinorecipient' brain regions including the hypothalamus, thalamus, pretectum, and tectum (superior colliculus homolog) (Baier and Wullimann, 2021). The tectum is the main retinorecipient brain area in fish and considered a center for transforming sensory stimuli into motor commands (Gahtan et al., 2005; Helmbrecht et al., 2018). It is a highly ordered structure with four main layers, the stratum opticum (SO), stratum fibrosum et griseum superficiale (SFGS), stratum griseum centrale (SGC) and stratum album centrale (SAC) and 10 sublaminae (Burrill and Easter Jr., 1994) (Fig. 5B). RGCs innervate the anterior to posterior anatomical axis of the tectum based on their cell body location in the eye, generating a topographic representation of visual space in the tectum (Robles et al., 2014; Stuermer, 1988). Tectal cell bodies form a folded sheet, the stratum periventriculare (SPV), which surrounds the highly layered synaptic neuropil area. The SPV contains two main anatomical cell types, periventricular interneurons (PVINs) and periventricular projection neurons (PVPNs) (Nevin et al., 2010; Scott and Baier, 2009). They are further characterized by differential branching patterns within the tectal neuropil layers and axonal projections to other brain regions or the contralateral tectal hemisphere (Förster et al., 2020; Helmbrecht et al., 2018; Kunst et al., 2019).

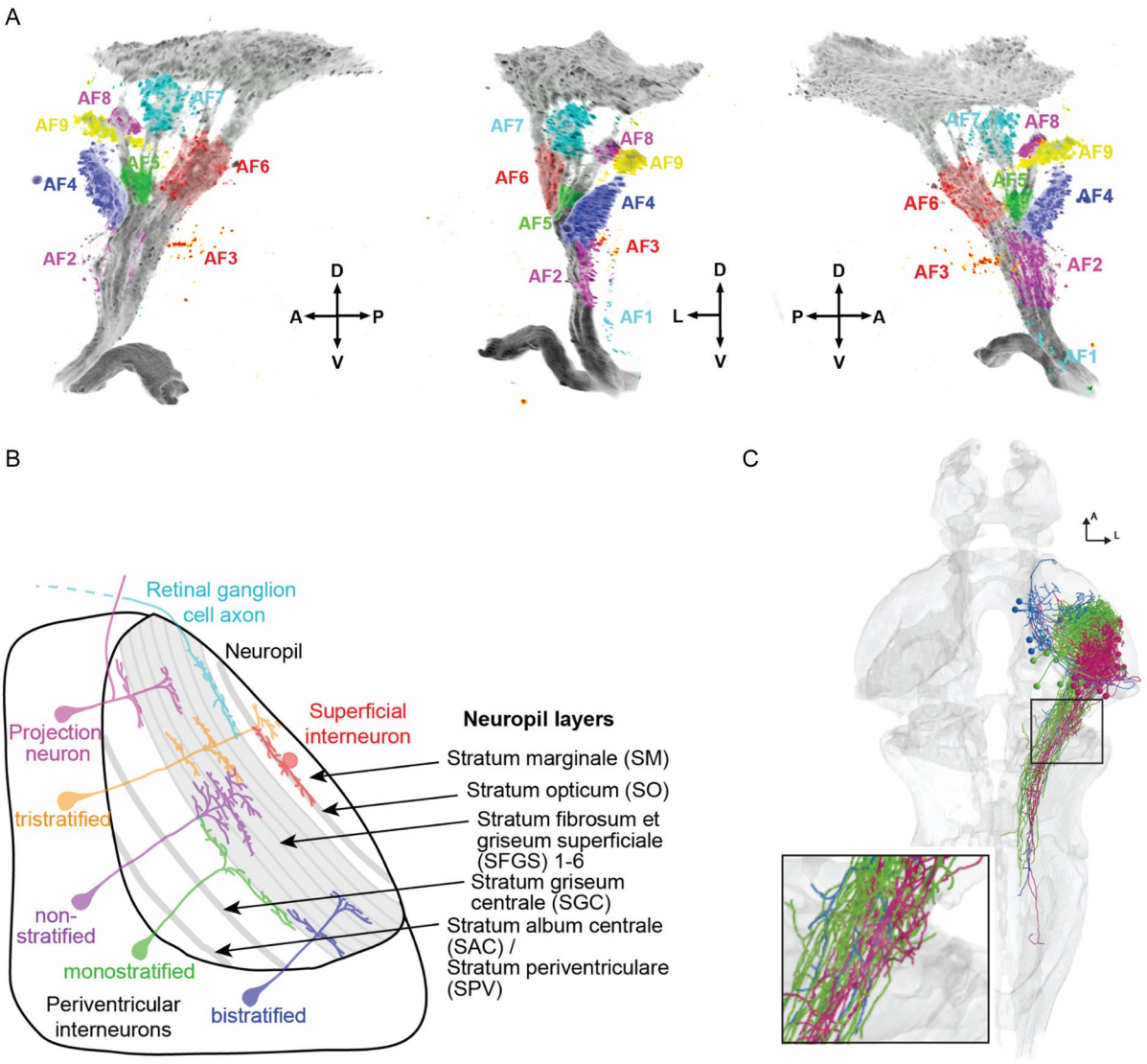

Figure 5: Structural organization of the larval zebrafish visual system

(A) Confocal stack of the retinal projectome in three views including the color-coded 10 retinal arborization fields (AFs) of the larval zebrafish. Adapted with permission (Baier and Wullimann, 2021).

(B) Morphological cell types in the larval zebrafish tectum based on selective arborizations in different neuropil layers. Adapted with permission (Förster et al., 2020).

(C) Axons of projection neurons in the tectum show topographical organization according to cell body position along the tectal anterior-posterior axis. Adapted with permission (Helmbrecht et al., 2018).

Topographic RGC input into the most superficial tectal layers (SO and SFGS) creates a visual map in tectal neuron activity (Niell and Smith, 2005). PVPN axon projections to the hindbrain are also topographically organized: Their activity causes

steering movements that are dependent on the axon location along a mediolateral axis, thus creating a topographic motor map (Helmbrecht et al., 2018) (Fig. 5C).

This high degree of anatomical and functional organization is well suited for ethologically relevant computations. The probably best-studied phenomenon is the tectal control of hunting behavior (Gahtan et al., 2005). Small, moving prey objects evoke responses in large swaths of the tectum (Muto et al., 2013). Inhibitory superficial interneurons (SINs) in the tectal neuropil are receptive to large stimuli and thus able to act as a spatial filter for small stimuli (Del Bene et al., 2010). The preference to small dots of individual tectal cells is further dependent on their anatomical localization and the resulting retinotopic receptive field. Neurons located in the posterior tectum with receptive fields in the lateral parts of the visual field tend to respond to smaller objects, while anterior tectal neurons are more likely to respond to larger visual stimuli (Förster et al., 2020). This posterior-anterior mapping is in concordance with the prey size on the respective parts of the retina at the beginning and the end of the hunting routine, respectively. Further, responses of anterior tectal assemblies to prey-like stimuli coincide with convergent eye saccades, a hallmark of the hunting routine (Bianco and Engert, 2015).

Just like hunting prey, evading predators through a startle response is an essential behavior under tectal control in larval zebrafish (Dunn et al., 2016; Temizer et al., 2015). RGC and thalamic projections to the tectum are essential for triggering escape responses and the appropriate escape direction, respectively (Heap et al., 2018; Temizer et al., 2015). Tectal neurons collectively encode the critical looming size at which escapes occur over time (Dunn et al., 2016). When challenged with two looming stimuli on opposing sides, individual tectal neurons switch their response preference according to relative stimulus sizes, thereby conveying a saliency signal (Fernandes et al., 2021). Interhemispheric tectal connectivity loops through the nucleus isthmi facilitate this computation and is the basis for a behavioral winner-take-all strategy.

Ventral to the tectum, the pretectum and thalamus form two other major visual structures that receive RGC input. Their substantially smaller retinal arborization fields suggest that only a subset of all retinal information reaches them.
In zebrafish, many pretectal neurons are mostly responsive to global visual motion

cues that result from self-motion such as translations or rotations (Kubo et al., 2014; Naumann et al., 2016). Those are equipped with large, often binocular receptive fields that are suited for self-motion extraction and form a topographic anatomical map of rotational direction (Wang et al., 2019; Zhang et al., 2022). Pretectal neurons are essential for eliciting adaptive behavioral responses to global motion cues, namely the optokinetic reflex for gaze stabilization in response to rotational motion (Kubo et al., 2014) and the optomotor response to stabilize body position upon translational motion (Naumann et al., 2016). In contrast, neurons of a distinct pretectal nucleus close to AF 7 respond to local motion of prey-like objects and elicit hunting routines upon activation (Antinucci et al., 2019; Semmelhack et al., 2014). Less is known about the structure and function of zebrafish thalamus. It an anatomically heterogeneous structure with several subdivisions, which is broadly separated into GABAergic prethalamus and glutamatergic thalamus proper (Mueller, 2012). Within thalamus proper, the anterior and dorsal posterior nuclei receive visual and the central posterior nucleus auditory input (Wullimann and Mueller, 2004). Direct retinal information reaches solely the anterior nucleus via AF 4 (Mueller, 2012). RGCs projecting to AF 4 and neurons in the thalamic anterior nucleus are involved in processing ambient luminance change such as dimming and looming stimuli as well as the resulting behaviors phototaxis and escapes, respectively (Heap et al., 2018; Suryadi et al., 2020; Zhang et al., 2017). The dorsal posterior nucleus does not receive retinal input (Wullimann and Mueller, 2004). In other fish species, the tectum is the main presynaptic visual partner of this nucleus (Northcutt, 2006; Striedter, 1990). It might be phylogenetically related to the mammalian pulvinar complex, a nucleus in the dorsal thalamus that is postsynaptic to the superior colliculus and implicated in visual attention (Benarroch, 2015; Mueller, 2012).

Whether any of the RGC types, AFs or retinorecipient brain regions contain dedicated circuits for processing conspecific stimuli such as burst-and-glide motion remains to be established. Since shoaling behavior is dependent on a precise balance of attraction and repulsion to keep a preferred distance to conspecifics, it is reasonable to assume that separate circuits in the visual system of larval zebrafish signal whether a conspecific is too far away or too close. In the latter case, previously identified circuits for detecting looming stimuli might also mediate social avoidance. In consequence, a separate ‘attraction circuit’ would detect conspecifics

from far away and and induce approach behavior. The OT would be a likely brain region to harbor neurons that localize a salient social signal and initiate directed approach.

1.6 Volumetric 2-photon microscopy for large-scale functional imaging

One well-suited strategy to screen the larval zebrafish visual system for neurons that detect social cues would be volumetric calcium imaging. The larval zebrafish is particularly well suited for imaging neuronal activity due to its transparency and small size, allowing for whole-brain activity recordings at cellular resolution in embedded (Ahrens et al., 2013; Bruzzone et al., 2021; Portugues et al., 2014) or unrestrained animals (Cong et al., 2017; Kim et al., 2017). Recent technical advances enable functional two-photon recordings of brain activity in juvenile and even adult zebrafish (Bergmann et al., 2018; Chow et al., 2020; Huang et al., 2020).

Since the invention of two-photon microscopy by Denk and colleagues in 1990, this technology has revolutionized the field of neuroscience (Denk et al., 1990). Measuring neuronal activity of neurons in the intact brain was now possible with unprecedented penetration depth and spatial resolution. Key is the concept of the two-photon effect, where the absorption of two photons in the infrared range (700-1300 nm) by a fluorophore yield the same energy as the absorption of one photon in the blue spectrum (450 - 500 nm). Using pulsed lasers with femtosecond precision increases the probability of two infrared photons hitting the same fluorophore at the same time, and still restricted to a narrow focal point. This way, fluorophores in genetically encoded calcium indicators (GECIs) such as GCaMP are excited only in small subvolumes, leading to very high spatial resolution. Fast scanning of the laser beam using motorized mirrors in combination with photon multiplier tube (PMT) detection of green emission light from GECIs enables rapid 2D and even 3D reconstruction of brain activity over time, limited only by the respective GECI calcium binding dynamics. Advances in optical technologies enable recording in larger and deeper brain areas through light wave front shaping (Hampson et al., 2021), or mesoscale imaging of whole cortical areas (Lu et al., 2020). The most recent development are miniature two-photon microscopes that allow recording in freely moving animals, even to the point of volumetric imaging (Skocek et al., 2018; Zong

et al., 2022). Further, imaging of whole brains in invertebrate species is feasible (Kato et al., 2015).

1.7 Precise registration and alignment of brains for functional anatomy

Through the innovation in hardware for recording brains came the need for analytical software tools that could bring order to the vast amounts of functional and structural data that large-scale two-photon imaging produces. It has proven very useful to mend brain data into one common anatomical reference frame (Randlett et al., 2015; Marquart et al., 2017). A shared coordinate system for all data leads to interpretability in variation between individual animals, localization of functional nodes of activity and intersection between functional and anatomical modalities. Initially developed for medical applications such as magnetic resonance imaging (MRI) or computer tomography (CT), several registration applications were adopted for aligning brain data of model organisms into one reference such as CMTK (Rohlfing and Maurer, 2003), Elastix (Klein et al., 2010), ANTs (Avants et al., 2011) and greedy (Venet et al., 2019). The underlying algorithms combine linear and non-linear transformations to achieve registration of two or more brain volumes with up to cellular precision (Lovett-Barron et al., 2017). The computed transformation matrices can be used to register secondary imaging channels such as transgene expression patterns, functional ROI pixels or anatomical reconstructions of individual neurons into the reference coordinate system (Panser et al., 2016). Taken together, functional two-photon calcium imaging in combination with brain registrations is well suited for investigating visual circuits for to social recognition because it enables the rapid and precise identification of functional nodes within brain areas or even whole brains. Yet, even neurons within an anatomically localized functional cluster can fulfill vastly different roles: For example, consider the VMHvl neurons that either elicit mating or aggression described earlier, which are intermingled in a small nucleus (see Figure 2). Untangling different cell types within a localized cluster or brain area can then guide understanding how one or multiple functional properties emerge from that set of neurons.

1.8 Identification of neuronal cell types through single-cell RNA sequencing and spatial transcriptomics

Understanding the inner workings of a machine, one ideally knows about all the cogs and screws within the device that act in concert. Likewise, to understand a neuronal circuit or a brain area in the context of social behavior and beyond, it may be desirable to have a complete 'parts list', i.e. a catalogue of its neurons cell types. Neuronal cell types can be identified across different modalities such as their morphology, connectivity, neurotransmitter identity or transcriptome. First attempts to categorize neurons date back to the very inception of neuroscience with Cajal's classic drawings of different neuronal morphologies. The new frontier is molecular: with the advent of single-cell RNA sequencing (scRNAseq), there has been an explosion in endeavors to generate catalogues of neuronal cell types based on their gene expression profile:

For instance, researchers from the Allen Brain Observatory found consensus transcriptomic classes of neurons in motor cortex of human, marmoset and mouse (Bakken et al., 2021). Other studies reported conserved and clade-exclusive neuron types by comparing transcriptomic cell types in reptile, amphibian and mammalian brains, collectively enabling insights into brain evolution (Hain et al., 2022; Tosches et al., 2018). For the larval zebrafish brain, transcriptomic cell types have been described in the eye (Kölsch et al., 2021), tectum (Martin et al., 2022), hindbrain (Tambalo et al., 2020) and even throughout early development (Raj et al., 2018). The resulting cell catalogues are valuable resources for understanding neuronal cell type diversity. By comparing gene expression profile of single neurons in homologue brain regions between species, one can further infer which neuronal cell types are conserved throughout evolution and might execute similar functions in the brain (Hahn et al., 2023; Pandey et al., 2023; Tosches et al., 2018).

However, when it comes to understanding how this diversity enables brain function, the integration of multiple modalities is key. Recent studies combine several techniques to achieve such cross-modality, from generating transgenic animals to filling individual neurons with dyes to linking two-photon imaging with spatial transcriptomics. For example, by combining scRNAseq and transgenic labeling, Kölsch et al. discovered a transcriptomic retinal cell type that is necessary for phototaxis through functional imaging and targeted ablations (Kölsch et al., 2021). A

study focused on transcriptomic cell types in mouse visual cortex area V1 revealed that cell type specific activity correlates with behavioral state of the animal (Bugeon et al., 2022). Here, the authors incorporated a technique that visualizes RNA molecules in intact tissues or tissue slices with up to single-molecule precision and puts recorded and sequenced cells in their spatial context. The need to visualize as many genes as possible led to the development of various multiplexing and barcoding techniques such as MERFISH (Chen et al., 2015). Here, multiple rounds of probe annealing with separate fluorescent markers enable combinatorial encoding of hundreds of genes. In a different approach, fluorescent molecules are recruited and amplified with a linker molecule directly to a specific RNA molecule in a process called hybridization chain reaction (HCR). This and similar techniques enable the encoding of up to five marker genes in one round of fluorophore staining within intact 3D tissues (Choi et al., 2018; Wang et al., 2012). Recent projects have shown that this technique is suitable for whole-brain staining of developing zebrafish (Lovett-Barron et al., 2017; Shainer et al., 2023). In the same animal, whole-brain gene expression data can be overlayed with functional time series through registration into a common reference frame. This technique yields multimodal investigation of cell type composition, only limited by the number of marker genes.

Taken together, the intersection of novel research techniques enables a holistic view on the molecular and functional organization of the developing zebrafish brain.

2. Publications

2.1 Visual recognition of social signals by a tectothalamic neural circuit

Johannes M. Kappel, Dominique Förster, Katja Slangewal, Inbal Shainer, Fabian Svara, Joseph C. Donovan, Shachar Sherman, Michał Januszewski, Herwig Baier* & Johannes Larsch*

*Corresponding authors

This article was published in *Nature* on August 4th 2022 (Kappel et al., 2022).

Article

Visual recognition of social signals by a tectothalamic neural circuit

https://doi.org/10.1038/s41586-022-04925-5

Received: 3 August 2021

Accepted: 2 June 2022

Published online: 13 July 2022

Open access

Check for updates

Johannes M. Kappel[1], Dominique Förster[1], Katja Slangewal[1,4], Inbal Shainer[1], Fabian Svara[1,2], Joseph C. Donovan[1], Shachar Sherman[1], Michał Januszewski[3], Herwig Baier[1]✉ & Johannes Larsch[1]✉

Social affiliation emerges from individual-level behavioural rules that are driven by conspecific signals[1–5]. Long-distance attraction and short-distance repulsion, for example, are rules that jointly set a preferred interanimal distance in swarms[6–8]. However, little is known about their perceptual mechanisms and executive neural circuits[3]. Here we trace the neuronal response to self-like biological motion[9,10], a visual trigger for affiliation in developing zebrafish[2,11]. Unbiased activity mapping and targeted volumetric two-photon calcium imaging revealed 21 activity hotspots distributed throughout the brain as well as clustered biological-motion-tuned neurons in a multimodal, socially activated nucleus of the dorsal thalamus. Individual dorsal thalamus neurons encode local acceleration of visual stimuli mimicking typical fish kinetics but are insensitive to global or continuous motion. Electron microscopic reconstruction of dorsal thalamus neurons revealed synaptic input from the optic tectum and projections into hypothalamic areas with conserved social function[12–14]. Ablation of the optic tectum or dorsal thalamus selectively disrupted social attraction without affecting short-distance repulsion. This tectothalamic pathway thus serves visual recognition of conspecifics, and dissociates neuronal control of attraction from repulsion during social affiliation, revealing a circuit underpinning collective behaviour.

Many animals live in groups, the result of a basic social affiliative drive, which requires detection and approach of conspecifics. Social affiliation is a prerequisite of consummatory actions such as aggression, mating or play[3], and is also a proximal cause of swarm, flock and herd formation. Although neural circuits that mediate such behaviours have received much attention[3,15], relatively little is known about the sensory detection of social signals (beyond pheromones)[15,16], and how such cues feed into the regulation of social distance. One important class of visual social signals is biological motion, which comprises conspecific movement patterns that trigger complex approach and pursuit behaviours[17–19], and elicit a social percept in humans[9,10]. Biological motion is also a key driver of zebrafish shoaling, a collective behaviour with well-characterized interaction rules in groups or pairs of animals[2,6,11,20], offering a model to investigate visual neural circuits underpinning social affiliation.

Neuronal activity during social affiliation

To identify the relevant neural circuits in juvenile zebrafish aged 21 days, we generated unbiased maps of recent neuronal activity after shoaling with real or virtual conspecifics (Fig. 1a). Virtual conspecifics were projected black dots moving either with fish-like biological motion, or continuously, which are highly attractive and weakly attractive, respectively[2] (Fig. 1b). We then recorded a snapshot of neuronal activity by rapid fixation and labelling of *c-fos* (official gene symbol, *fosab*) mRNA[21] using third-generation in situ hybridization chain reaction[22] (HCR) analysis in the forebrain, midbrain and anterior hindbrain (Fig. 1a,c and Extended Data Fig. 1). Visual inspection of the registered and merged *c-fos* signal from all of the animals identified 31 distinct clusters with robust activity in response to one or more stimulus conditions (Fig. 1c and Extended Data Fig. 1).

Splitting the data by stimulus group revealed that social context differentially activated these clusters. Activation by real and virtual conspecifics overlapped in a subset of clusters, including the lateral rostral hypothalamus (cluster Hrl) and intermediate hypothalamus (cluster Hi3), while showing a distinct pattern in other areas. In the optic tectum (TeO), virtual conspecifics activated a ventrolateral cluster, matching the retinotopic representation of the ventrally projected black dot visual stimulus[23]. By contrast, real conspecifics moving at the same elevation as the imaged fish activated the anterior and dorsal TeO more strongly (Fig. 1d). Virtual and real conspecifics activated a cluster in the dorsal thalamus (DT), and real conspecifics also activated an anterior cluster in the ventral thalamus (VT) (Fig. 1d). The DT *c-fos* cluster overlapped with an expression hotspot of the gene *cortistatin* (*cort*, also known as somatostatin 7 (*sst7*)), which we co-labelled using a third, multiplexed HCR probe and used subsequently as a DT landmark[24]

[1]Max Planck Institute for Biological Intelligence (formerly Max Planck Institute of Neurobiology), Planegg, Germany. [2]Max Planck Institute for Neurobiology of Behavior – caesar, Bonn, Germany. [3]Google Research, Zurich, Switzerland. [4]Present address: Centre for the Advanced Study of Collective Behaviour, University of Konstanz, Konstanz, Germany. ✉e-mail: herwig.baier@bi.mpg.de; johannes.larsch@bi.mpg.de

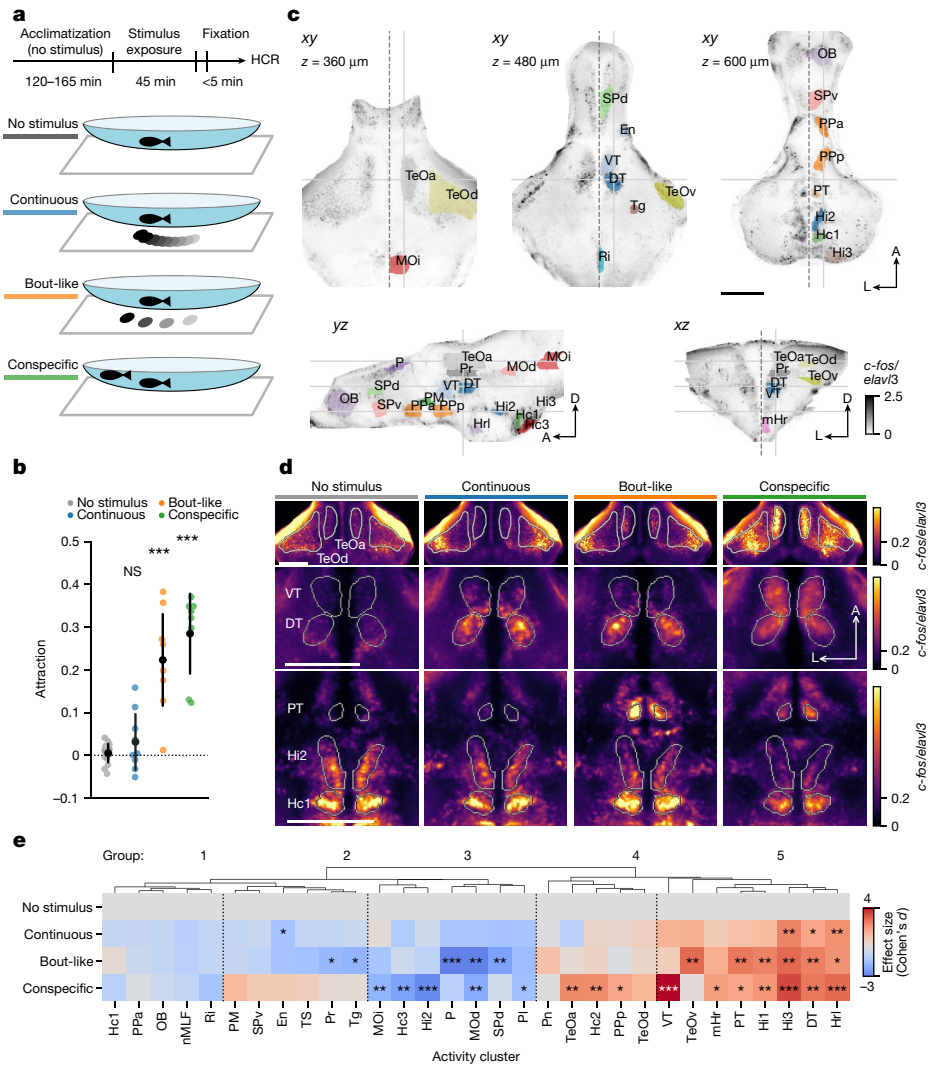

Fig. 1 | Fish-like motion activates a conserved social behaviour network. **a**, Schematic of stimulus presentation for activity mapping. **b**, Attraction towards stimuli shown in **a**. $n = 17$ (no stimulus) or $n = 9$ (continuous; bout-like) single animals; and $n = 8$ animals tested in 4 pairs (conspecific). Data are mean (black dots) ± 1 s.d. Exact P values were calculated using two-tailed t-tests compared with the no-stimulus group: $P = 0.16$ (continuous); $P = 5.2 \times 10^{-8}$ (bout-like); $P = 8.1 \times 10^{-11}$ (conspecific). Bonferroni-corrected α values: NS, $P > 0.05/3$ (NS); ***$P < 0.001/3$. **c**, Representative slices of maximum-intensity-normalized *c-fos* signal merged across all 28 registered animals. The views are horizontal (top row), sagittal (bottom left) and coronal (bottom right). The solid grey lines indicate the corresponding planes across the slices. The dashed line indicates the midline. Coloured patches indicate activity clusters (Extended Data Fig. 1). A, anterior; D, dorsal; L, lateral. **d**, The average normalized *c-fos* signal at the three representative horizontal planes indicated in **c**. $n = 6$ (no stimulus), $n = 8$ (continuous), $n = 6$ (bout-like) and $n = 8$ (conspecific) animals. **e**, The effect size (Cohen's d) of normalized bulk *c-fos* induction compared with the no-stimulus condition. Negative values indicate a lower signal compared with the no-stimulus condition. The dendrogram represents hierarchical clustering. Statistical analysis was performed using two-tailed t-tests in each activity cluster versus the no-stimulus group. *$P < 0.05/3$, **$P < 0.01/3$, ***$P < 0.001/3$ (α values were Bonferroni-corrected per activity cluster). Animal numbers are the same as in **d**. Additional statistical information is provided as Source Data. Scale bars, 200 µm. DT, dorsal thalamus; En, entopeduncular nucleus; Hc1, caudal hypothalamus 1; Hc2, caudal hypothalamus 2; Hc3, caudal hypothalamus 3; Hi1, intermediate hypothalamus 1; Hi2, intermediate hypothalamus 2; Hi3, intermediate hypothalamus 3; Hrl, rostral hypothalamus, lateral; mHr, rostral hypothalamus, medial; MOd, medulla oblongata, dorsal; MOi, medulla oblongata, intermediate; nMLF, nucleus of the medial longitudinal fasciculus; OB, olfactory bulb; P, pallium; Pl, pallium, lateral; PM, magnocellular preoptic nucleus; Pn, pineal; PPa, anterior parvocellular preoptic nucleus; PPp, posterior parvocellular preoptic nucleus; Pr, pretectum; PT, posterior tuberculum; Ri, inferior raphe; SPd, subpallium, dorsal; SPv, subpallium, ventral; TeOa, tectum, anterior; TeOd, tectum, dorsal; TeOv, tectum, ventral; Tg, lateral tegmentum; TS, torus semicircularis; VT, ventral thalamus.

(Extended Data Fig. 2a,b). One cluster in the posterior tuberculum (PT) stood out as selectively active with bout-like motion and real conspecifics. By contrast, *c-fos* in the intermediate hypothalamic cluster Hi2 was highest for the no-stimulus condition and inversely related to stimulus attraction (Fig. 1d).

To quantify these trends, we calculated the average bulk *c-fos* intensity per cluster in each animal (Extended Data Figs. 1e and 2c). Statistical analysis of the *c-fos* signal revealed significant modulation of activity in 21 clusters by at least one stimulus relative to the no-stimulus condition (Fig. 1e). Hierarchical clustering of all areas separated five major groups of clusters that were qualitatively (1) not modulated relative to the absence of stimulus, (2) weakly suppressed by virtual conspecifics, (3) suppressed by most stimuli, (4) activated more by real conspecifics than virtual ones and (5) activated by most stimuli (Fig. 1e).

Together, this unbiased global activity map identified brain networks whose activity is modulated by real and virtual conspecifics with putative roles in social affiliation. These include posterior preoptic and rostral hypothalamic areas that are likely to be homologous to

paraventricular and anterior hypothalamic nuclei commonly assigned to the conserved social behaviour network[12–14] (Hrl, mHr, PPp). Clusters in groups 3 and 4, which were modulated exclusively by real conspecifics (Hc3, Hi2, PPp, Hc2), might reflect neuronal responses beyond those necessary for acute social affiliation. They may contribute to perception of threat or homeostatic stress mechanisms, potentially through visual cues that are not present in bout-like dot stimuli or additional sensory modalities such as olfaction and mechanosensation[16,21,25,26]. Thus, the set of clusters activated by virtual conspecifics highlights a core network underlying the visuomotor transformation associated with shoaling, beginning with the recognition of conspecifics.

Thalamic neurons encode biological motion

Our *c-fos* labelling method highlights putative visual input pathways for social affiliation. Biological motion probably enters the brain through the TeO and DT[27], therefore providing an opportunity to investigate sensory detection of this social cue. To understand stimulus selectivity of individual neurons in these visual areas, we turned to volumetric two-photon calcium imaging of juvenile brain activity in response to presentation of virtual conspecifics.

Fish that expressed nuclear-localized GCaMP6s in almost all neurons (carrying the transgene *elavl3:H2B-GCaMP6s*) were immobilized on the stage of a microscope equipped with a custom-built remote focusing set-up for rapid image acquisition (Extended Data Fig. 3). We imaged simultaneously in 6 imaging planes at 5 Hz, extending 600 × 600 × 200 um (*x*,*y*,*z*) (Fig. 2a). This volume included the retinorecipient brain areas highlighted by our *c-fos* analysis, DT and TeO, as well as pretectum, nucleus isthmi, VT and habenulae (Fig. 2b and Extended Data Fig. 4). Analysis of 28,306 registered neurons across 11 animals revealed that responses to virtual conspecifics were most prominent in the TeO (51% of active neurons), followed by pretectum (12%), DT (10%) and nucleus isthmi (10%) (Extended Data Fig. 4), qualitatively matching the *c-fos* mapping results (Fig. 2c).

To identify neurons that encode biological motion, we computed a bout preference index (BPI) as the normalized difference in the response to behaviourally attractive bout-like motion versus unattractive continuous motion (Fig. 2d,e). The majority of neurons did not differentiate between bout frequencies (mean BPI 0.01 ± 0.07). However, 13 ± 5% of all neurons scored BPI > 0.5, corresponding to a threefold increase in $\Delta F/F$ for bout-like motion compared with continuous motion in these neurons. We next focused our attention on these putative bout preference neurons (BPNs). In a subset of animals, we determined that the BPN population was largely unresponsive to looming and moving grating control stimuli (Extended Data Fig. 5a). Most BPNs were located in the TeO (36%) and DT (18%) (Extended Data Fig. 4). Gaussian kernel density estimation (KDE) yielded the DT as the anatomical area of highest BPN density (Fig. 2f). Within the DT, BPNs were concentrated in a posterior cluster, overlapping with DT *c-fos* activity (Fig. 1c). By contrast, tectal BPNs were distributed broadly along the anteroposterior and dorsoventral axes with lower relative frequency (Extended Data Fig. 4c). The anatomical overlap of *c-fos* and GCaMP signals in the TeO and DT suggests that virtual conspecifics in the open-loop configuration activate key circuits for social recognition even in immobilized animals.

If activity of DT-BPNs drives shoaling behaviour, their tuning should match specific parameters of biological motion. DT-BPNs had a response peak at a stimulus bout frequency of 1.2 ± 1.6 Hz, closely matching the juvenile's typical swim bout frequency of around 1.25 Hz, which also most effectively elicits shoaling[2] (Fig. 2g). To examine whether DT-BPNs encode acceleration or average speed of virtual conspecifics, we collected a separate dataset and systematically varied each parameter independently (Fig. 2h). At continuous motion, DT-BPNs were barely modulated by stimuli moving at 2 to 150 mm s^{-1}. At 1.5 Hz, DT-BPNs yielded maximal responses at 7.2 ± 1.7 mm s^{-1} (Fig. 2h), similar to a juvenile's typical swim speed at around 5 mm s^{-1} and, again, matching the behavioural tuning[2]. Morphing acceleration from continuous to bout-like along Gaussian speed profiles at fixed average speed of 5 mm s^{-1} and 1.5 Hz bout frequency modulated DT-BPN responses as a function of acceleration with a maximum at the highest possible acceleration of 12 m s^{-2} (projector limit). Taken together, DT-BPNs detect biological motion through periodic acceleration at fish-like speed and bout frequency, and are therefore tailored for the detection of juvenile zebrafish during shoaling.

To relate DT-BPN responses to naturalistic visual percepts, we tested another set of animals with 'dot shoaling' stimuli on trajectories that recapitulate positions of conspecifics relative to a real focal animal during shoaling (Extended Data Fig. 5b). DT-BPNs were strongly and persistently activated by such stimuli (Extended Data Fig. 5d). Self-motion during shoaling also generates global motion with temporal dynamics similar to the fish-like cues. To examine whether global motion activates DT-BPNs, we rotated whole-field stimuli with matched bout-like motion and spatial frequency (Extended Data Fig. 5c). Global motion strongly activated pretectal neurons[27] but not DT-BPNs (Fig. 2i), suggesting that the latter encode fish-like biological motion and not self-motion-induced visual signals.

Zebrafish shoaling with real or virtual conspecifics emerges at around two weeks of age[2,6,28], whereas younger fish show mainly interanimal repulsion[2,29]. We therefore hypothesized that functional maturation of BPNs coincides with this transition. Contrary to this prediction, BPNs already existed in larvae, but with lower fractions compared with the juveniles (10 ± 3% of all recorded neurons). Furthermore, BPNs were similarly distributed in the brain, with the KDE centre in the DT (Fig. 2j). Registration of the larval data to the Max Planck Zebrafish Brain Atlas[30,31] (https://mapzebrain.org) confirmed localization of the DT-BPN cluster to the *vglut2a*-positive DT area, ventrally touching the *gad1b*-positive VT[32]. The larval DT-BPN cluster was molecularly defined by the expression of *cort*, as seen in juveniles, and *pth2* (Extended Data Fig. 5e), a gene of which thalamic expression tracks the density of conspecifics in zebrafish through mechanosensory signals[33]. Overlap with *pth2* raises the possibility of multimodal integration of conspecific signals in DT. Furthermore, the mean frequency tuning curve across all larval DT-BPNs and mean tuning peak were similar to juveniles (Extended Data Fig. 5f). Finally, we determined that DT-BPNs also developed in socially isolated larvae, demonstrating that tuning to conspecific motion in DT is largely independent of social experience (Extended Data Fig. 5g). Thus, functional BPN maturation precedes shoaling, and the developmental transition is either gradual in nature or requires a change in additional circuit nodes. The presence of BPNs in pre-juvenile stages provides an opportunity to investigate the circuit with the experimental tools and resources available in larvae.

EM reconstruction of the biological motion circuit

Across vertebrates, the thalamus acts as a gateway for state-dependent sensory information[32,34]. We hypothesized that DT-BPNs could serve that role for social cues, connecting visual brain areas and the conserved social behaviour network[12,27]. To reveal the anatomy of the DT-BPN circuit, we analysed an electron microscopy (EM) whole-brain dataset of a larval zebrafish at 5 days post-fertilization (d.p.f.), acquired at synaptic resolution[35]. We registered the larval DT onto the EM volume to identify the cell body location of putative BPNs (pBPN) in the DT (Extended Data Fig. 6a–c). We randomly selected and completely traced 34 cells in this region (Fig. 3a,b). All of these cells extended their primary neurite ventrolaterally and showed both dendritic and axonal arborizations in a thalamic neuropil region, posterior to retinal arborization field AF4 (Fig. 3b,c). In this region, we randomly selected presynaptic contact sites on putative BPN dendrites, supported by an automated synapse segmentation[35] (Methods), and identified their partner neurons (Fig. 3c). A total of 26.7% of input synapses were provided by other DT neurons (Extended Data Fig. 6d) and, similarly, 26.7% arrived from

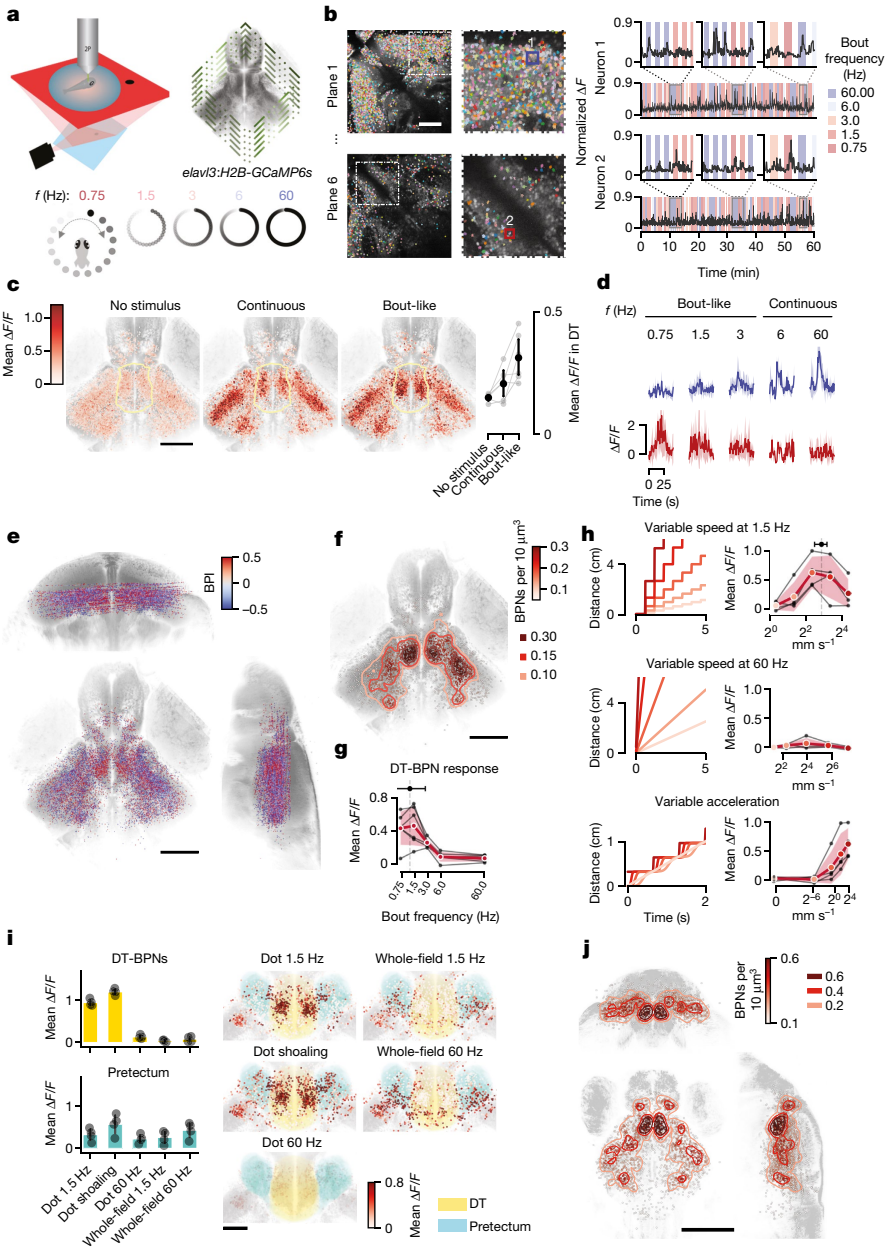

Fig. 2 | Dorsal thalamus neurons are activated by fish-like motion. **a**, Schematic of the experimental set-up. **b**, Example imaging planes in the TeO and DT with all segmented neuronal ROIs, representative for $n = 11$ animals (left). Right, representative normalized $\Delta F/F$ traces of one tectal and one thalamic neuron. **c**, Horizontal view of all responsive neurons ($n = 28{,}306$ total, $2{,}573 \pm 1{,}175$ per fish) from 11 fish (18–22 d.p.f.) aligned to a juvenile reference brain (left). Colour indicates mean baseline $\Delta F/F$ (no stimulus), and responses to continuous and bout-like motion. The yellow line indicates the DT. Right, mean responses of all DT neurons per fish ($n = 258 \pm 198$, 2,837 total) from $n = 6$ animals with a number of recorded DT-BPNs of >30. Data are mean ± 1 s.d. **d**, Mean $\Delta F/F$ responses of example neurons from **b** to all stimulus frequencies. **e**, The distribution of all responsive neurons from $n = 11$ fish in the reference brain. The colour map shows the BPI. Opacity scales with absolute BPI (0–0.5). **f**, The distribution of BPNs (312 ± 143 neurons per fish, 3,437 total). Colour reflects a Gaussian KDE; contours delineate densities of 0.1, 0.15 and 0.3 BPNs per 1,000 µm³. $n = 11$ fish. **g**, DT-BPN tuning to stimulus frequency. The mean peak across neurons was 1.2 Hz ± 1.6 Hz. $n = 563$ neurons. The black lines represent the mean values of individual animals. Data are from a subset of animals in **e** with a number of recorded DT-BPNs of >30. $n = 6$ animals. **h**, DT-BPN tuning to average speed at 1.5 Hz or 60 Hz and acceleration. The cartoons show stimulus displacement over time. Data are mean ± 1 s.d. of all of the neurons shown above. $n = 291$ neurons. The black lines indicate individual animals. $n = 4$ fish, 73 ± 10 neurons per fish. **i**, DT-BPN and PreT responses to local dot motion and whole-field motion and their anatomical distribution. Circles (left) show the mean of individual animals. $n = 4$ fish, 77 ± 15 (DT-BPNs), 114 ± 48 (PreT) neurons per fish. Data are mean ± 1 s.d. **j**, The distribution of BPNs in 7 d.p.f. larvae ($n = 4$ fish, 230 ± 87 neurons per fish) as in **f**. Scale bars, 100 µm (**b** and **i**) and 200 µm (**c**, **e**, **f** and **j**).

tectal periventricular projection neurons (PVPNs; Fig. 3d). We also identified synaptic input from the VT (16.7%), ipsi- and contralateral nucleus isthmi (10%; Extended Data Fig. 6e), superior ventral medulla oblongata (6.7%), torus semicircularis (6.7%), hypothalamus (3.3%) and cerebellum (3.3%). Overall, the majority of input synapses were established by ipsilateral neurons (76.7%). Identified PVPNs ($n = 13$) send their axons ventrally through the postoptic commissure, and make ipsi- or contralateral connections to putative BPNs within the thalamic neuropil region. A single PVPN can be presynaptic to several putative BPNs (Fig. 3e), and a single BPN can receive input from several PVPNs, both ipsi- and contralaterally (Extended Data Fig. 6f). Next, we quantified presynaptic partners of DT-projecting PVPNs: 55% of all input

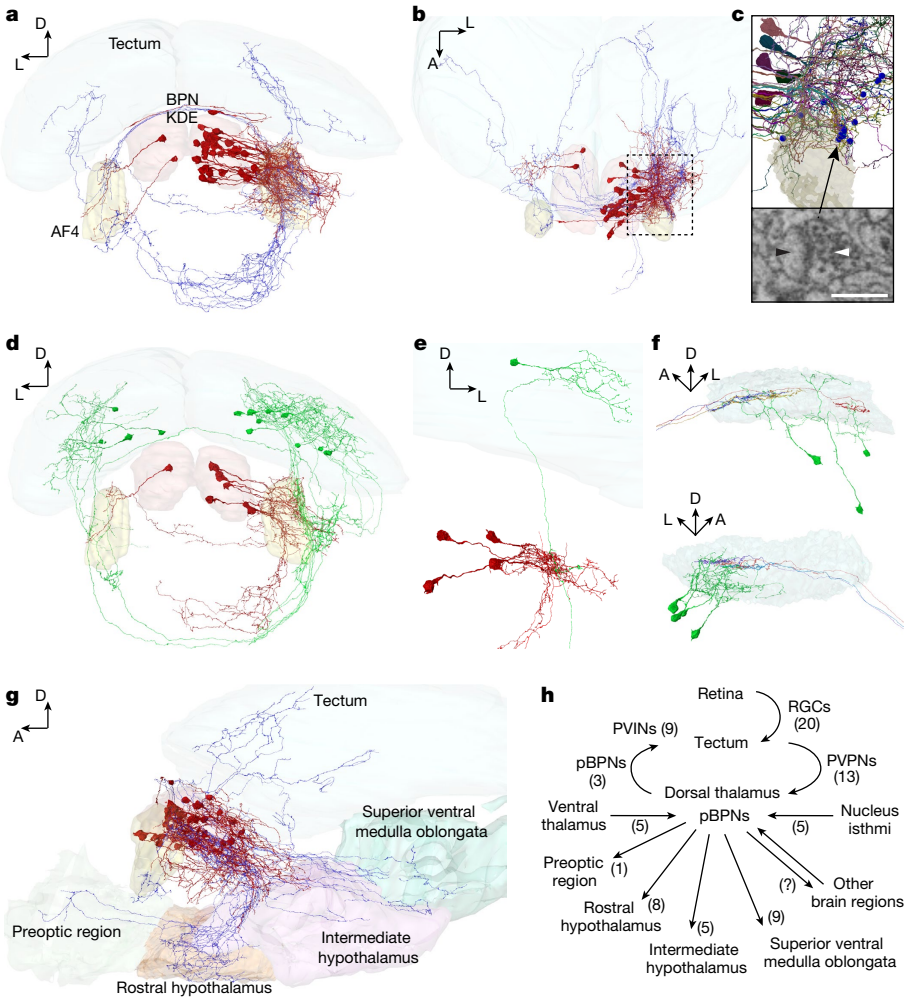

Fig. 3 | Connectivity of the larval thalamic bout-preference region. **a**, Frontal view of an EM reconstruction of neurons in the bout-preference region (BPN KDE, red) of the DT. Axons are shown in blue. **b**, Top view of the neurons shown in **a**. **c**, Magnified view of the thalamic arborization field, outlined in **b**. Synapses with identified presynaptic partners are shown as blue spheres. One representative synapse of a tectal PVPN axon (white arrow) onto a putative BPN's dendrite (pBPN, black arrow) is indicated below (randomly chosen). **d**, Frontal view of tectal PVPNs (green) and their postsynaptic pBPN partners (red). **e**, Example of a single PVPN (green), which makes ipsilateral synaptic contacts to at least four identified pBPNs (red). **f**, Side view of the left (top) and the right (bottom) tectal SFGS layers, showing the PVPNs (green) and their presynaptic retinal ganglion cell axons (different colours). PVPN axons are not shown for clarity. **g**, Side view of the pBPNs (red, axons in blue) and their axonal target regions (Supplementary Video 2). AF4 (yellow) is shown as a reference. **h**, Circuit diagram. Identified cell types are indicated next to arrows with cell numbers in parentheses. For **c**, scale bar, 0.5 µm.

synapses arrived from a specific class of retinal ganglion cells, which exclusively arborized in the SFGS3/4 layer of the tectum[36] (Fig. 3f); 35% were from tectal periventricular interneurons and, interestingly, 10% of input synapses arrived from other PVPNs, which also projected to the DT and contacted pBPNs.

We further investigated the downstream target regions of putative DT-BPNs. Of the 34 traced DT neurons, 24 had long projection axons and made synaptic contacts in other brain areas, whereas 10 neurons had local ($n = 3$) or premature ($n = 7$) axonal projections. Our analysis revealed the superior ventral medulla oblongata ($n = 9$ cells), rostral hypothalamus ($n = 8$), intermediate hypothalamus ($n = 5$), contralateral thalamus ($n = 3$), preoptic region ($n = 1$) and the tectum ($n = 3$) as axonal targets (Fig. 3g,h). Putative BPNs that projected to the tectum targeted the SFGS layer, where they contacted tectal periventricular interneurons (Extended Data Fig. 6g).

To complement the EM tracings, we next analysed the morphology of traced neurons residing in the BPN-KDE of the light microscopy mapzebrain atlas[30]. We identified 13 putative BPNs that all extended their primary neurites ventrolaterally into a neuropil area posterior of AF4, consistent with the EM data. Of these neurons, 12 projected into other brain areas, including the tectum ($n = 1$), preoptic area ($n = 1$), rostral hypothalamus ($n = 1$), intermediate hypothalamus ($n = 3$), superior ventral medulla oblongata ($n = 5$) and inferior ventral medulla oblongata ($n = 2$) (Extended Data Fig. 6h,i).

These findings suggest a pathway for the detection of biological motion: retinal information reaches DT-BPNs through tectal PVPNs and is subsequently transmitted to brain areas that are proposed to regulate social behaviour, including the preoptic region, and clusters in the rostral, intermediate and caudal hypothalamus, which showed *c-fos* signal during shoaling behaviour (Fig. 1f). Gradual maturation of DT projections and/or addition of synapses, such as those connecting the ventral forebrain at around 14 d.p.f., may then underlie the emergence of shoaling at the juvenile stage[37].

Social attraction requires the biological motion circuit

As TeO and DT-BPNs are activated by fish-like motion, we hypothesized that this pathway is necessary for shoaling. To test this hypothesis, we ablated TeO and DT in juvenile animals and analysed effects on free-swimming interactions with virtual conspecifics.

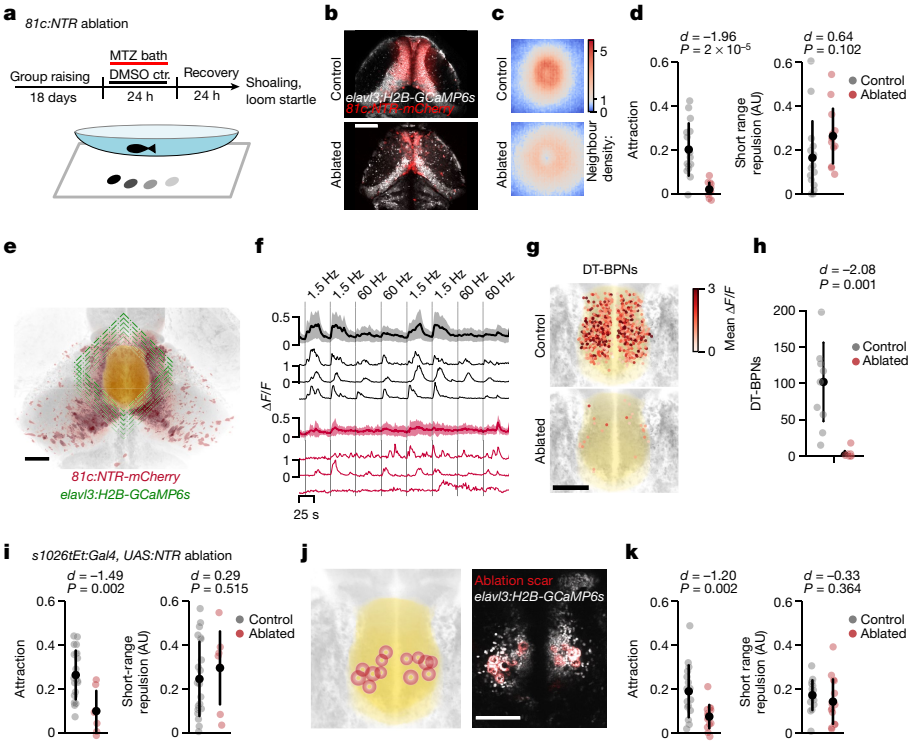

Fig. 4 | The TeO–DT circuit is necessary for social attraction. a, Schematic of the shoaling test after chemogenetic ablation. ctr., control. **b**, Two-photon image of 21 d.p.f. *SAGFF(lf)81c:Gal4, UAS:NTR-mCherry* and *elavl3:H2B-GCaMP6s* animals 24 h after ablation versus control treatment. Representative of three similar fish. **c**,**d**, Reduced neighbour density (**c**) and attraction (**d**) in *81c:NTR*-ablated animals. Short-range repulsion is intact. $n = 13$ (ablated) and $n = 15$ (control) animals. The neighbour maps in **c** show the probability of finding the stimulus in space with the animal at the centre of the map, heading up. Each map is 60 mm × 60 mm. AU, arbitrary units. **e**, Schematic of volumetric two-photon imaging in the DT after *81c:NTR* ablation. **f**, Mean and example Δ*F* traces of all DT-BPNs for ablated and control animals show that *81c:NTR* ablation strongly reduces responses to bout-like motion. The vertical lines mark the start of stimulus presentation. The shaded areas denote 1 s.d. around the mean. $n = 25$ (ablated) and $n = 849$ (control). **g**,**h**, Fewer DT-BPNs in *81c:NTR* (-ablated) animals. **g**, The anatomical location of all DT-BPNs across animals coloured by mean Δ*F*/*F* to bout-like motion. $n = 25$ (ablated) and $n = 849$ (control). The yellow area shows the DT. **h**, Quantification of DT-BPNs per animal. $n = 7$ (ablated) and 9 (control) animals. Cohen's *d* effect size is shown. The *P* value was calculated using the two-sided Mann–Whitney *U*-test. **i**, Attraction is strongly reduced in *s1026tEt:NTR*-ablated animals. Short-range repulsion is intact. $n = 7$ (ablated), $n = 21$ (control) animals. **j**, Bilateral two-photon laser ablation of neurons in the DT-BPN region in juvenile zebrafish. **k**, Reduced attraction after DT laser ablation. $n = 7$ (ablated) and $n = 9$ (embedding control) animals. Short-range repulsion is intact. Data in **d**, **h**, **i** and **k** represent individual animals and mean ± 1 s.d. Cohen's *d* effect size is shown. The *P* values were calculated using two-tailed Student's *t*-tests with no correction. For **b**, **e**, **g** and **j**, scale bars, 100 µm.

We genetically targeted tectal cells for chemogenetic ablation using the *SAGFF(lf)81c* enhancer trap line to drive expression of nitroreductase. *SAGFF(lf)81c* is strongly expressed in tectal neurons and weakly expressed in parts of the pretectum, habenula, anterior DT and anterior VT (Fig. 4b and Extended Data Fig. 8). Although ablated animals appeared healthy and had slightly faster swim kinetics, they showed a severe loss of attraction towards virtual conspecifics ($P < 0.001$; Fig. 4c,d and Extended Data Fig. 7). To investigate the spatial scale of this behavioural defect, we computed neighbour density maps that represent relative spacing with virtual conspecifics. In the controls, neighbour maps revealed a central zone of short-range (5–15 mm) repulsion, surrounded by a ring of long-distance attraction (10–30 mm). In ablated animals, this balance was shifted. The ring of attraction was strongly reduced, whereas the zone of repulsion was intact (Extended Data Fig. 7a,b). Moreover, looming-induced startle responses were at the control level in ablated animals (Extended Data Fig. 7c). Finally, we confirmed that *SAGFF(lf)81c* ablation disrupted shoaling with a real conspecific ($P < 0.001$; Extended Data Fig. 7d).

To understand the neural correlates of these effects, we recorded neuronal responses to continuous and bout-like motion in DT after *SAGFF(lf)81c* ablation. We found that ablation reduces the number of DT-BPNs by more than 95% ($P = 0.0014$, 4 ± 6 versus 94 ± 4 cells per animal) (Fig. 4f,g). We observed similar trends for dot motion at 1.5 and 60 Hz (continuous), at which tectal ablation significantly reduced the number of top-scoring neurons ($P < 0.01$). Responses to looming and translational grating motion in the surrounding pretectum were also reduced in ablated 21 d.p.f. juveniles but not in ablated 7 d.p.f. larvae (Extended Data Fig. 8). These results are consistent with our inferred wiring diagram, which places tectal PVPNs upstream of DT-BPNs as their main sensory driver.

Next, we tested the necessity of DT for shoaling by chemogenetic ablation using the *s1026tEt* enhancer trap line to drive expression of neuronally restricted nitroreductase. The *s1026tEt* Gal4 insertion drives strong and selective expression of a UAS-linked nitroreductase transgene in DT of juvenile zebrafish (Extended Data Fig. 8a). We found that ablation of *s1026tEt* cells in juveniles caused a selective loss of attraction ($P = 0.002$) and a modest increase in swim bout frequency, whereas short-range repulsion and visual escapes remained intact (Fig. 4i and Extended Data Fig. 7e). Finally, we tested the necessity of DT-BPNs directly by laser-ablation of the DT-BPN area in 21 d.p.f. animals. After ablation, we found a selective loss of attraction, whereas short-range repulsion, visual escapes and overall swim kinetics remained intact ($P = 0.002$; Fig. 4j,k and Extended Data Fig. 7e). Together, these results suggest that *SAGFF(lf)81c* neurons and DT-BPNs are essential elements of a pathway that mediates the affiliative aspect of shoaling, but are dispensable for collision avoidance during shoaling and visual escape from a looming threat.

Discussion

Affiliation with conspecifics is a core building block of social behaviours that offer benefits for collectives, such as efficient food detection or evasion of predators[3,8,38]. As a consequence, animals need to robustly recognize neighbours in cluttered environments during highly dynamic interactions. These interactions rely on the balance of attraction and repulsion into an appropriate distance[1,4,5]. Although empirical models of collective behaviour have postulated distinct individual-level behavioural rules[5,7,8], the neuronal implementation of such coordination has remained unclear, largely because mutual interactions mask causal relationships between conspecific signals and receiver responses. Our results in shoaling zebrafish now highlight fish-like motion[2,11] as a salient trigger signal of an attraction pathway that converges on a multimodal[33], socially activated DT cluster and feeds into hypothalamic areas that are probably homologous with nodes of the proposed social behaviour network[12–14,21]. Neuronal activity in this circuit therefore represents an inherently kinetic metric of neighbouring animals, in contrast to current shoaling models that emphasize positional information[1,4,6,20]. By contrast, short-range repulsion engages a separate circuit, probably overlapping with the collision-avoidance pathway[39–41]. These results add support for the emerging importance of visual motion cues in social recognition[10,42–44]. The correspondence of sensory activation in freely shoaling versus immobilized animals with virtual conspecifics suggests that this approach can also reveal the role of neural circuit nodes in the downstream network during shoaling for an understanding how collective dynamics emerge from neuronal computations in individuals.

Online content

Any methods, additional references, Nature Research reporting summaries, source data, extended data, supplementary information, acknowledgements, peer review information; details of author contributions and competing interests; and statements of data and code availability are available at https://doi.org/10.1038/s41586-022-04925-5.

1. Strandburg-Peshkin, A. et al. Visual sensory networks and effective information transfer in animal groups. *Curr. Biol.* **23**, R709–R711 (2013).
2. Larsch, J. & Baier, H. Biological motion as an innate perceptual mechanism driving social affiliation. *Curr. Biol.* **28**, 3523–3532 (2018).
3. Wei, D., Talwar, V. & Lin, D. Neural circuits of social behaviors: Innate yet flexible. *Neuron* **109**, 1600–1620 (2021).
4. Bastien, R. & Romanczuk, P. A model of collective behavior based purely on vision. *Sci. Adv.* **6**, eaay0792 (2020).
5. Heras, F. J. H., Romero-Ferrero, F., Hinz, R. C. & de Polavieja, G. G. Deep attention networks reveal the rules of collective motion in zebrafish. *PLoS Comput. Biol.* **15**, e1007354 (2019).
6. Hinz, R. C. & de Polavieja, G. G. Ontogeny of collective behavior reveals a simple attraction rule. *Proc. Natl Acad. Sci. USA* https://doi.org/10.1073/pnas.1616926114 (2017).
7. Reynolds, C. W. Flocks, herds and schools: a distributed behavioral model. In *Proceedings of the 14th Annual Conference on Computer Graphics and Interactive Techniques* 25–34 (Association for Computing Machinery, 1987); https://doi.org/10.1145/37401.37406
8. Krause, J. & Ruxton, G. D. *Living in Groups* (OUP Oxford, 2002).
9. Johansson, G. Visual perception of biological motion and a model for its analysis. *Percept. Psychophys.* **14**, 201–211 (1973).
10. Troje, N. F. & Westhoff, C. The inversion effect in biological motion perception: evidence for a 'life detector'? *Curr. Biol.* **16**, 821–824 (2006).
11. Nunes, A. R. et al. Perceptual mechanisms of social affiliation in zebrafish. *Sci. Rep.* **10**, 3642 (2020).
12. O'Connell, L. A. & Hofmann, H. A. The Vertebrate mesolimbic reward system and social behavior network: A comparative synthesis. *J. Comp. Neurol.* **519**, 3599–3639 (2011).
13. Herget, U., Wolf, A., Wullimann, M. F. & Ryu, S. Molecular neuroanatomy and chemoarchitecture of the neurosecretory preoptic-hypothalamic area in zebrafish larvae: Zebrafish NPO. *J. Comp. Neurol.* **522**, 1542–1564 (2014).
14. Kelly, A. M. A consideration of brain networks modulating social behavior. *Horm. Behav.* **141**, 105138 (2022).
15. Chen, P. & Hong, W. Neural circuit mechanisms of social behavior. *Neuron* **98**, 16–30 (2018).
16. Gerlach, G. & Wullimann, M. F. Neural pathways of olfactory kin imprinting and kin recognition in zebrafish. *Cell Tissue Res.* **383**, 273–287 (2021).
17. Ribeiro, I. M. A. et al. Visual projection neurons mediating directed courtship in *Drosophila*. *Cell* **174**, 607–621 (2018).
18. Coen, P., Xie, M., Clemens, J. & Murthy, M. Sensorimotor transformations underlying variability in song intensity during *Drosophila* courtship. *Neuron* **89**, 629–644 (2016).
19. Hindmarsh Sten, T., Li, R., Otopalik, A. & Ruta, V. Sexual arousal gates visual processing during *Drosophila* courtship. *Nature* **595**, 549–553 (2021).
20. Harpaz, R., Nguyen, M. N., Bahl, A. & Engert, F. Precise visuomotor transformations underlying collective behavior in larval zebrafish. *Nat. Commun.* **12**, 6578 (2021).
21. Tunbak, H., Vazquez-Prada, M., Ryan, T. M., Kampff, A. R. & Dreosti, E. Whole-brain mapping of socially isolated zebrafish reveals that lonely fish are not loners. *eLife* **9**, e55863 (2020).
22. Choi, H. M. T. et al. Third-generation in situ hybridization chain reaction: multiplexed, quantitative, sensitive, versatile, robust. *Development* **145**, dev165753 (2018).
23. Stuermer, C. A. Retinotopic organization of the developing retinotectal projection in the zebrafish embryo. *J. Neurosci.* **8**, 4513–4530 (1988).
24. Sherman, S., Kawakami, K. & Baier, H. Retinal input influences pace of neurogenesis but not cell-type configuration of the visual forebrain. Preprint at *bioRxiv* https://doi.org/10.1101/2021.11.15.468630 (2021).
25. Wee, C. L. et al. Zebrafish oxytocin neurons drive nocifensive behavior via brainstem premotor targets. *Nat. Neurosci.* **22**, 1477–1492 (2019).
26. Lovett-Barron, M. et al. Multiple convergent hypothalamus–brainstem circuits drive defensive behavior. *Nat. Neurosci.* **23**, 959–967 (2020).
27. Baier, H. & Wullimann, M. F. Anatomy and function of retinorecipient arborization fields in zebrafish. *J. Comp. Neurol.* **529**, 3454–3476 (2021).
28. Dreosti, E., Lopes, G., Kampff, A. R. & Wilson, S. W. Development of social behavior in young zebrafish. *Front. Neural Circuits* **9**, 39 (2015).
29. Marques, J. C., Lackner, S., Félix, R. & Orger, M. B. Structure of the zebrafish locomotor repertoire revealed with unsupervised behavioral clustering. *Curr. Biol.* **28**, 181–195 (2018).
30. Kunst, M. et al. A cellular-resolution atlas of the larval zebrafish brain. *Neuron* **103**, 21–38 (2019).
31. Shainer, I. et al. A single-cell resolution gene expression atlas of the larval zebrafish brain. Preprint at *bioRxiv* https://doi.org/10.1101/2022.02.11.479024 (2022).
32. Mueller, T. What is the thalamus in zebrafish? *Front. Neurosci.* **6**, 64 (2012).
33. Anneser, L. et al. The neuropeptide Pth2 dynamically senses others via mechanosensation. *Nature* **588**, 653–657 (2020).
34. McGinley, M. J. Brain states: sensory modulations all the way down. *Curr. Biol.* **30**, R1263–R1266 (2020).
35. Svara, F. et al. Automated synapse-level reconstruction of neural circuits in the larval zebrafish brain. *Nat. Methods* (in the press).
36. Robles, E., Laurell, E. & Baier, H. The retinal projectome reveals brain-area-specific visual representations generated by ganglion cell diversity. *Curr. Biol.* **24**, 2085–2096 (2014).
37. Goode, C. et al. Late onset of synaptotagmin 2a expression at synapses relevant to social behavior. *J. Compar. Neurol.* **529**, 2176–2188 (2021).
38. Handegard, N. O. et al. The dynamics of coordinated group hunting and collective information transfer among schooling prey. *Curr. Biol.* **22**, 1213–1217 (2012).
39. Temizer, I., Donovan, J. C., Baier, H. & Semmelhack, J. L. A visual pathway for looming-evoked escape in larval zebrafish. *Curr. Biol.* **25**, 1823–1834 (2015).
40. Heap, L. A. L., Vanwalleghem, G., Thompson, A. W., Favre-Bulle, I. A. & Scott, E. K. Luminance changes drive directional startle through a thalamic pathway. *Neuron* **99**, 293–301 (2018).
41. Fernandes, A. M. et al. Neural circuitry for stimulus selection in the zebrafish visual system. *Neuron* **109**, 805–822.e6 (2021).
42. Ning, J. et al. Behavioral signatures of structured feature detection during courtship in *Drosophila*. *Curr. Biol.* **32**, 1211–1231 (2022).
43. Blakemore, S.-J. & Decety, J. From the perception of action to the understanding of intention. *Nat. Rev. Neurosci.* **2**, 561–567 (2001).
44. Sliwa, J. & Freiwald, W. A. A dedicated network for social interaction processing in the primate brain. *Science* **356**, 745–749 (2017).

Methods

Animal care and transgenic zebrafish

Adult, juvenile and larval zebrafish (*Danio rerio*) were housed and handled according to standard procedures. All animal experiments were performed under the regulations of the Max Planck Society and the regional government of Upper Bavaria (Regierung von Oberbayern), approved protocols: ROB-55.2Vet-2532.Vet 03-15-16, ROB-55.2Vet-2532.Vet 02-16-31, and ROB55.2Vet-2532.Vet 02-16-122. Experimental animals were outcrosses to TL or TLN (nacre) unless otherwise noted. The following transgenic lines were used: *Tg(elavl3:H2B-GCaMP6s)jf5*[45], *SAGFF(lf)81c* (TeO Gal4 line)[46], Tg(*UAS-E1B:NTR-mCherry)c264*[47], *Et(fos:Gal4-VP16)s1026t* (DT Gal4 line)[48], *Tg(UAS:BGi-epNTR-TagRFPT-utr.zb3)mpn420* (this study).

Larvae were raised in Danieau solution under a 14–10 h light–dark cycle at 28.5 °C until 6 d.p.f. For experiments in juveniles, animals were then raised under standard facility conditions at 28.5 °C in groups of 20–25 individuals. The fish were fed by feeding robots once a day with artemia and 2–3 times a day with dry food.

Shoaling assay and behaviour quantification

Shoaling with real and virtual conspecifics was assayed as previously described[2]. In brief, 15 or 35 individual animals were transferred individually into shallow watch glass dishes of 10 cm or 7 cm diameter, respectively, separated by a grid of visual barriers and resting on a projection screen. Custom-written Bonsai[49] workflows were used to project stimuli to each animal and to track animal location at 30 fps. Stimuli were black dots on a white background moving along a predefined, synthetic-trefoil shaped trajectory at an average speed of 5 mm s^{-1}. For continuous motion, the stimulus position was updated 30 times per second. For bout-like motion, the stimulus position was updated once every 666 ms. Dot diameter was 2 mm unless noted otherwise, and 0 mm in the no-stimulus condition.

To assay shoaling of pairs of real conspecifics, we introduced a second animal in the same dish and did not show any projected stimuli. FastTrack[50] was used for post hoc tracking of real pair shoaling.

Attraction and neighbourhood maps were quantified as previously described[2] using custom-written Python software. We calculate the 'real' average interanimal distance or animal dot distance for each animal in 5 min chunks (IADr). Next, we generate 10 time-shifted trajectories and recalculate the shifted average inter animal or animal dot distance (IADs) for each time shift. Mean IADs for all time shifts are used to compute attraction as (IADs − IADr)/IADs.

For neighbourhood maps, neighbour position time series were transformed into the focal animal's reference frame to compute a binned 2D histogram.

Repulsion was quantified as the reduction in attraction at the centre of each animal's neighbour density map. Neighbour density maps were gaussian-filtered (sigma = 3 mm) before obtaining 24 radial line scans (width of 5 mm) starting from the centre of the map. Repulsion was the area above the average line scan, at radii less than the radius at which maximum neighbour density occurred (Extended Data Fig. 7a), divided by the full length of the scan (29 mm).

Looming stimuli were presented in the virtual shoaling setup[41]. Looming discs appeared once every minute at a defined offset of 5 mm to the left or the right from the current centre of mass of each animal. Looming discs expanded within 500 ms to the indicated final size and followed the animal. To compute an escape fraction, we defined an escape response as a trial in which the animal moved more than twice as far in a time window of 1 s immediately following the loom compared to the 1.3 s before. Bout duration was computed using peak detection on the velocity time series of each animal.

c-fos activity mapping

Shoaling assay for c-fos. For *c-fos* labelling, we used *nacre;elavl3:H2B-GCaMP6s* fish at 21 d.p.f. Thirty five fish were transferred into individual dishes and left without stimulation in the presence of white projector illumination from below for acclimatization and to establish a low, non-social *c-fos* baseline. Each animal was assigned randomly to one of the four stimulus groups. After 2 h, continuous or bout-like motion were shown to groups 1 and 2, respectively, whereas groups 3 and 4 continued to see no stimulus. After 45 min, groups 1, 2 and 3 were quickly euthanized and fixed. Four animals of group 4 were then transferred into the dishes of four other animals of this group for shoaling. After 45 min, these eight animals were euthanized and fixed as well.

HCR staining and imaging. Animals were euthanized and fixed on 4% ice cold paraformaldehyde (PFA). The PFA was washed out after 24 h with 1× PBS and the samples were gradually dehydrated and permeabilized with methanol and stored in −20 °C for several days until the HCR in situ labelling was performed. All of the HCR reagents were purchased from Molecular Instruments and the staining was performed according to the manufacturer's protocol for whole-mount zebrafish larvae. In brief, the samples were separated into 2 juvenile fish per single 1.5 ml Eppendorf tube. Rehydration steps were performed by washing for 5 min each in 75% methanol/PBST (1× PBS + 0.1% Tween-20), 50% methanol/PBST, 25% methanol/PBST and finally five times with 100% PBST. The samples were permeabilized with 30 µg ml^{-1} proteinase K for 45 min at room temperature, followed by postfix with 4% PFA for 20 min at room temperature and 5 washes in PBST for 5 min each. The samples were prehybridized in a 500 µl probe hybridization buffer (Molecular Instruments) for 30 min at 37 °C. Hybridization was performed by adding 2 pmol of each probe set to the hybridization buffer and incubating for 16 h at 37 °C. Probe sets for *c-fos* (B5 initiator), *cort* (B3 initiator) and *elavl3* (B2 initiator) were purchased from and designed by Molecular Instruments. To remove the excess probes, the samples were then washed 4 times for 15 min each with a wash buffer (Molecular Instruments) at 37 °C, followed by 2 washes of 5 min each with 5× SSCT (5× SSC + 0.1% Tween-20) at room temperature. Pre-amplification was performed by incubating the samples for 30 min in an amplification buffer (Molecular Instruments) at room temperature. The fluorescently labelled hairpins (B2-488, B3-647, B5-546) were prepared by snap cooling: heating at 95 °C for 90 s and then cooling to room temperature for 30 min. Hairpin solution was prepared by adding 10 µl of the snapped-cooled hairpins (3 µM stock concentration) to a 500 µl amplification buffer. The pre-amplification buffer was removed, and the samples were incubated in the hairpin solution for 16 h at room temperature. The excess hairpins were washed three times with 5× SSCT for 20 min each wash, and the samples were stored in 5× SSCT in the dark at 4 °C until imaging.

For dorsal imaging, the samples were embedded in 2.5% low melting agarose in 1× PBS. Imaging was performed with a Leica SP8 confocal microscope equipped with a ×20 water-immersion objective. *z*-Stacks, comprising four tiles, covering of the entire brain were taken (final stitched image size: 1,950 px × 1,950 px, 1,406 µm × 1,406 µm, 3 µm in *z*). All 32 samples were imaged with the exact same laser power, gain, zoom, averaging and speed to faithfully quantify and compare the fluorescent signal between the samples. For ventral imaging, the samples were removed from the agarose and dissected to remove the jaw and the gills. After the dissections, the samples were embedded upside down and imaged in the same manner. Four brains were lost during ventral imaging and were therefore excluded entirely from the subsequent analysis.

Image registration. Image registration was performed using Advanced Normalization Tools (ANTs[51]) running on the MPCDF Draco/Raven Garching computing cluster. Before registration, stacks were batch-processed in ImageJ. Each stack was downsampled to 512 px width at the original aspect ratio using bilinear interpolation, split into individual channels and saved as .nrrd files. For ventral stacks, artefacts of the dissection such as left-over autofluorescent muscle fibres

and skin were masked before registration. Initial attempts to register the *elavl3* HCR channel of dorsal or ventral HCR confocal stacks to a live-imaged two-photon reference of *elavl3-H2B-GCaMP6s* expression were not successful, probably due to deformations resulting from the HCR protocol and diverse qualitative differences in image features between the imaging modalities. Instead, separate dorsal and ventral HCR registration templates were generated from scratch by running antsMultivariateTemplateConstruction2.sh on three manually selected stacks. Next, all dorsal and ventral stacks were registered to their respective templates using antsRegistration. Finally, the ventral template was registered to the dorsal template using affine + b-spline transformations via antsLandmarkBasedTransformInitializer with the help of 25 manually curated landmarks in each stack before applying standard antsRegistration. The resulting ventral-to-dorsal transform was then applied to re-register all ventral stacks into one common (dorsal) reference frame.

c-*fos* signal intensity quantification. Image analysis was performed using custom scripts in Python. Registered dorsal and ventral stacks were merged as the arithmetic mean intensity for each animal. To normalize to a drop in signal intensity with tissue depth, the *c-fos* signal was divided voxel-wise by the *elavl3* HCR signal. For visualizations of imaging planes, the *elavl3* signal used in normalization was filtered by a 3D gaussian (filter width: 55 µm, 55 µm, 15 µm *x*,*y*,*z*). For area-wise *c-fos* quantification, unfiltered *elavl3* signal was used in normalization. To identify activity clusters, merged stacks from all animals per condition were generated by finding the maximum intensity at each voxel across animals. A combined RGB hyperstack was generated that showed *c-fos* signal for each condition, *cort* HCR and *elavl3* HCR for reference in different colours for visual inspection. Activity clusters were manually drawn as 3D masks on the hyperstack using the ImageJ segmentation editor on orthogonal overlay views. Masks were drawn with the intent to outline prominent, distinct clusters of *c-fos* signal, irrespective of their modulation by social condition. The full hyperstack, including cluster masks is available. Brain areas housing the activity clusters were identified by comparison of the *elavl3* reference to the mapzebrain atlas[30] and additional resources[13,52,53].

Individual *cort*- and *c-fos*-positive cells in DT were counted manually using the ImageJ cell counter plugin. For statistical analysis across activity clusters and conditions, bulk normalized *c-fos* signal was computed as the average intensity of all voxels belonging to a given cluster. Effect size was determined in each cluster for each condition versus the no-stimulus condition by pairwise computation of Cohen's *d* defined as the difference of the means divided by the pooled standard deviation. To determine significant activity modulation compared to the no-stimulus condition, we performed repeated two-tailed *t*-tests and corrected for multiple comparisons in each family of tests (each activity cluster) using the Bonferroni correction. Hierarchical clustering of the activity clusters was performed on the effect sizes using the seaborn method clustermap with the default parameters for average Euclidean clustering.

Functional two-photon calcium imaging

Two-photon functional calcium imaging was performed on 6–8 d.p.f. larvae and 17–22 d.p.f. juvenile *elavl3:H2B-GCaMP6s* transgenic fish without paralysis or anaesthesia. The 6–8 d.p.f. larvae were embedded in 2% agarose with the tail freed as previously described[39]. Juveniles (17–22 d.p.f.) were embedded in 3% agarose. As juvenile zebrafish are prone to hypoxia in this preparation, several precautions were taken. A drop of low-melting agarose was placed onto a petri dish and allowed to cool before a fish was introduced and oriented with a pipette tip. Once solidified, agarose was removed from the mouth, gills and tail using scalpels to restore active and passive breathing (Extended Data Fig. 3). Additional oxygen was supplied by continuously perfusing the dish. The perfusion medium consisted of fish water freshly oxygenated to saturation at the start of the experiment and diluted 1:1 with demineralized water to support ionoregulation and buffered with 1.2 mM NaH_2PO_4 and 23 mM $NaHCO_3$[54]. To monitor health, we checked heartbeat and breathing movements of gills and mouth before and after an experiment. Only fish that were breathing and moving after the end of the experiment were included in the analysis. The embedded fish were mounted onto the stage of a modified two-photon moveable objective microscope (MOM, Sutter Instrument, with resonant-galvo scanhead) with a ×20 objective (Olympus XLUMPLFLN, NA 1.0) and imaged for at least 60 min. Typically, fish resumed swimming immediately after release from embedding. Only fish that did not drift up or down in their preparation were used for analysis. Fish in which no tectal responses could be observed were eliminated from the analysis. Fast volumetric imaging of the tectum and/or thalamus was performed using a custom-built remote focusing arm added before the microscope (Extended Data Fig. 3b). The remote focusing path was constructed using the 30 mm and 60 mm Thorlabs cage system, and consists of the following parts (in order of forwards traversal): a half-wave plate (Thorlabs, AHWP05M-980), a polarizing beam splitter (Thorlabs, PBS102), two lenses (Thorlabs, AC254-100-B-ML and AC508-200-B-ML), a quarter-wave plate (Thorlabs, AQWP10M-980), remote objective (Nikon, CFI ×16 0.8 NA), and a gold mirror (Thorlabs, PF05-03-M01) mounted onto a custom piezo (PPS-D08300-001 nanoFaktur, 300 µm closed loop range, with a nPoint LC.402 controller). The piezo was mounted on a *xyz* translation stage with tip-tilt control. Changing the mirror position is rapid (for the step sizes used for imaging, 1–2 ms) and results in a change of focus of the excitation beam exiting the main objective. Refocusing through the remote arm enabled rapid sequential imaging of 6 planes with a nonlinear step size ranging from 6–24 µm at 5 volumes per second. Remote focusing was not used for the high-resolution single-plane imaging in Fig. 2h,i. The plane size ranged from 370 µm × 370 µm for larvae to 1,075 µm × 1,075 µm for juveniles. Laser power ranged from 12.3 mW to 15.4 mW. The spatial sampling (0.7–2.1 µm px^{-1}) and optical resolution enabled discrimination of single cells with cell body diameters typically in the range of 5 µm to 8 µm.

z-Stack acquisition and image registration. For each functionally imaged fish, a *z*-stack of the entire brain was taken (512 × 512 or 1,024 × 1,024 pixels, 2 µm in *z*, 835–920 nm laser wavelength, plane averaging 50–100×) with the two-photon microscope. Larval data were registered to the mapzebrain atlas[30] using the *elavl3:H2B-GCaMP6s* reference. For juvenile data, a standard brain was generated from three high-quality *z*-stacks (150× frame averaging) as described in the '*c-fos* activity mapping' section and each juvenile brain was registered to it. The generation of a standard brain and the parameters used for ANTs registration have been described in detail previously[30].

To align functional regions of interest (ROIs) from 2P data to a common reference frame, a two-step strategy was used. First, average frames of all imaging planes were registered to individual *z*-stacks using template matching. Converted ROI locations in z-stack coordinates were then transformed to the larval and juvenile common reference frames by running the ANTs command antsApplyTransformsToPoints with the matrices from the *z*-stack registrations.

Visual stimuli. Visual stimuli were designed using PsychoPy and projected by an LED projector (Texas Instruments, DLP Lightcrafter 4500, with 561 nm long-pass filter) on Rosco tough rolux 3000 diffusive paper placed into a petri dish filled with fish water.

Frequency tuning. A black dot moving on a circular trajectory (radius, 18 mm) with the fish head in the centre was shown starting either perpendicular to the fish at the left, or in front of the fish. The dot was moved in discrete jumps at 0.75, 1.5, 3.0, 6.0 or 60.0 Hz at an overall speed of 5 mm s^{-1} (15.9 degrees (deg) s^{-1}). Each frequency was presented using a dot diameter of 4 mm (12.7 deg). Moreover, 1.5 Hz and 60.0 Hz

stimuli were also presented with dot diameters of 2 mm (6.4 deg) and 8 mm (25.1 deg). Both clockwise and counter-clockwise presentations were shown. The frequency, direction and, if applicable, size were randomly drawn at each stimulus instance. Each stimulus had a duration of 22.6 s and was followed by a 20 s break. A total of 13 stimuli were shown per 10 min recording. Five to nine of these recordings were performed in each fish, leading to an average of four to six presentations of each stimulus. For Fig. 2b, only responses to dots (4 mm diameter) with 1.5 Hz and 60 Hz bout frequency were analysed. For Fig. 2g, again only responses to 4 mm dots were analysed.

Specificity. Naturalistic stimulus trajectories consisted of a 4 mm diameter dot (12.7 deg) moving along real trajectories from one of two interacting juvenile zebrafish that were previously recorded[2]. The trajectory was computed as a fish-centric view of the conspecific with respect to a focal fish. To avoid noise in the heading calculation due to tracking jitter, the trajectory was convolved with a normalized hamming kernel (mode: valid, window length: 20). The naturalistic motion sequences were shown for 1 min each (Extended Data Fig. 5b). For the whole-field motion stimulus an image was created by combining random intensities and restricted spatial distributions in Fourier space, matching the size of the moving dot (Extended Data Fig. 5c). The computed image either rotated in discrete jumps of 1.5 Hz or continuously at 60 Hz. In both cases the stimulus took 22.6 s to finish a complete round. All stimuli, 1.5 Hz dot, 60 Hz dot, 1.5 Hz whole-field, 60.0 Hz whole-field and naturalistic dot motion were shown in a pseudo-random order during 6x10 min recordings.

Kinetic parameters. Presented 4 mm diameter (12.7 deg) dots moved clockwise on a circular trajectory (18 mm radius). Five speeds were tested using a continuously moving dot: 2.5, 5, 15, 50 and 150 mm s^{-1} (8, 15.9, 47.7, 159.2 and 477.5 deg s^{-1}). Five speeds at a bout frequency of 1.5 Hz were tested by increasing the distance the dot moved during each bout. This increased both the average speed and the acceleration during bouts. The following parameters were tested: 1.25 mm s^{-1}; 3 m s^{-2}, 2.5 mm s^{-1}; 6 m s^{-2}, 5 mm s^{-1}; 12 m s^{-2}, 10 mm s^{-1}; 24 m s^{-2}, and 20 mm s^{-1}; 48 m s^{-2} (4 deg s^{-1}; 9.5 × 10^3 deg s^{-2}, 8 deg s^{-1}; 19.1 × 10^3 deg s^{-2}, 15.9 deg s^{-1}; 38.2 × 10^3 deg s^{-2}, 31.8 deg s^{-1}; 76.4 × 10^3 deg s^{-2} and 63.7 deg s^{-1}; 152.8 × 10^3 deg s^{-2}). Finally, for changing acceleration during each bout, we modelled each bout as a gaussian speed profile and changed the width of the curve. Each stimulus still had an average speed of 5 mm s^{-1} (15.9 deg s^{-1}) through a normalization factor. The following peak accelerations were tested: 0.0, 0.02, 0.5, 2.0 and 12.0 m s^{-2} (0, 0.06, 1.6, 6.3 and 38.2 × 10^3 deg s^{-2}).

Control stimuli after tectal ablation. Control stimuli consisted of translational gratings moving caudorostrally with respect to the fish (width, 20 mm; frequency, 0.12 Hz; duration, 20 s) and a looming stimulus (expansion from 0.6 deg to 110 deg in 83 ms, delay 10 s with disk and 20 s without stimulus) centred below the fish. One grating was shown at the beginning, followed by the dot stimuli, another grating and finally the looming stimulus. These recording sessions took 10 min each and were separated by a 1 min break to avoid potential habituation or response suppression due to the looming stimulus.

Data analysis for two-photon imaging

Suite2P[55] was used for motion correction, ROI detection, cell classification and signal extraction. For the entire analysis, a GCaMP6s time-constant of 7 s was used to accommodate the slow kinetics partially due to the nuclear localization of this sensor. On the basis of a visual inspection of the raw data, a cell diameter of 4–6 px was used. In detail, raw recording files were deinterleaved into separate time series for each plane. An extra motion-correction step was required owing to ripple noise stemming from the resonant mirror: to avoid spurious alignment to the noise pattern, rigid and non-rigid motion correction was performed on a spatially low-pass filtered time series (Gaussian, sigma = 4). The resulting motion-correction parameters were applied to the raw data. Next, the time series were downsampled fivefold to one volume per second. On the downsampled data, ROIs were detected and fluorescent traces were extracted.

Thresholding. Neuron ROIs were thresholded in a two-step process. First, the built-in Suite2p classification algorithm iscell was applied using the default parameters. Second, *iscell*$^+$ ROIs that showed a mean $\Delta F/F$ response to any stimulus above the 95th percentile (Fig. 2)/90th percentile (Fig. 4).

Mean $\Delta F/F$ responses. For each functional ROI, the fluorescent trace was normalized and split into stimulus episodes. $\Delta F/F$ was computed by using the 5 s before stimulus onset as the baseline. $\Delta F/F$ temporal responses were averaged across stimulus presentations per stimulus and then averaged over time to receive one value per stimulus.

BPI. On the basis of the behavioural tuning curves to bout frequency[2], stimuli were split into bout-like (0.75–3 Hz) and continuous (6–60 Hz) categories, regardless of stimulus size or directionality. BPI was defined as the difference in mean over mean $\Delta F/F$ to bout-like stimuli and mean over mean $\Delta F/F$ to continuous stimuli divided by their sum (equation (1)). BPNs were considered all ROIs that scored BPI >0.5, which equates to a threefold higher bout response.

$$\frac{\text{mean } \Delta F/F \text{ (bout)} - \text{mean } \Delta F/F \text{ (continuous)}}{\text{mean } \Delta F/F \text{ (bout)} + \text{mean } \Delta F/F \text{ (continuous)}} \quad (1)$$

Tuning peaks. For computing peaks in the tuning of neurons to a variable, mean $\Delta F/F$ responses were interpolated with a one-dimensional spline (scipy.interpolate.InterpolatedUnivariateSpline, $k = 2$, second degree) and the location of the maximum was computed.

Gaussian KDE. To generate a kernel density estimate of BPNs in anatomical space, BPN coordinates were used to fit a Gaussian Kernel (sklearn.neighbors.KernelDensity(*, bandwidth = 10 (14 for 7 d.p.f.), algorithm='auto', kernel='gaussian', metric='euclidean'). In detail, the brain was divided along the rostrocaudal axis and, for each hemisphere, a separate kernel was fitted with the contained BPNs. The resulting two kernels were used to generate probability density fields of each hemisphere, which were then merged again. The resulting density was thresholded so that only voxels within the brain itself had values > 0 and all voxels in the volume surrounding the brain equalled 0. Probability values were then normalized so that the sum would result in the total number of BPNs. To draw contours of areas with certain threshold BPN density, the KDE volume was binarized so that all voxels above threshold equalled 1. Of the resulting binarized volume a two-dimensional maximum intensity projection was computed for each orthogonal anatomical axis and a contour-finding algorithm (skimage.measure.find_contours) was applied to the two-dimensional projection.

Definition of the larval DT

The outline of the larval thalamus proper was refined with expert help of M. Wullimann (LMU). The refinement was based on extensive analysis of gene expression[52]. The *elavl3* reference stain was used to identify the diencephalic regions. Proliferative cells, however, which are abundant in the anterior DT at the larval stage, are not labelled by *elavl3*. The neurogenin line was used to indicate the early glutamatergic cells belonging to DT. Neurogenin is absent in the prethalamus (VT). The VT/DT boundary was further defined using *gad1b* and *dlx4*, which label late and early GABAergic cells, respectively. GABAergic cells are mainly found in VT, although the intercalated nucleus and the anterior nucleus of DT may contain some *gad1b* positive cells. The pretectum/DT

boundary was defined using *gad1b* and *th*. The latter marks dopamine cells present in the pretectum.

EM and segmentation of mapzebrain regions

A detailed description of the EM dataset and region mapping is published elsewhere[35]. In brief, the Serial Block Face Scanning EM dataset was of a 5 d.p.f. larval zebrafish imaged at a resolution of 14 × 14 × 25 nm. A diffeomorphic mapping between the mapzebrain light-microscopy brain reference coordinate system and the EM coordinate system generated by the dipy (https://dipy.org/) Python library was used to overlay mapzebrain (https://mapzebrain.org) region annotations over the EM data. Registration accuracy was reviewed for different brain regions with an alignment error of maximal ~5 µm (midbrain) to ~20 µm (hindbrain). We applied flood-filling networks for an automated reconstruction of all neurons[56] within the whole-brain EM dataset[35]. To correct for split and merge errors of the segmentation, we used the Knossos application (www.knossos.app). Proof-reading of single pBPN-DT cells started at the cell body location and ended when all branches were completely traced. Growth cones defined premature neurons. Proof-reading of partner cells started at the synapse and was again performed until the whole cell was completed. Synapses have been automatically segmented using the SyConn v2 pipeline[35]. Input to pBPN-DT cells and tectal PVPNs was quantified by randomly selecting ten incoming synapses per cell and tracing input partner cells, until their cell bodies were identified.

Nitroreductase ablations

To chemogenetically ablate neurons, fish expressing nitroreductase (NTR) were treated with 7.5 mM metronidazole (MTZ) in Danieau's solution with 1 ml l^{-1} dimethylsulfoxid (DMSO) for larvae, or 7.5 mM MTZ in fish facility water with 2 ml l^{-1} DMSO for juvenile fish, respectively. Control fish were only treated with the respective DMSO concentration in the absence of MTZ. For *SAGFF(lf)81c* ablations, the canonical *UAS-E1B:NTR-mCherry(c264)* nitroreductase was used[47].

Transgenic animals (RFP^+) and control sibling fish (RFP^-) were incubated in MTZ + DMSO solution for 16–24 h overnight. For the experiment shown in Extended Data Fig. 7b,e, we additionally incubated RFP^+ and RFP^- animals in DMSO only. Animals recovered for 16–24 h in system water before starting imaging or behaviour experiments.

In larvae, *s1026tEt* drives strong expression in the DT, dorsal VT, ventral pretectum and ventral telencephalon, and additional background expression in the heart and trunk musculature[31,48]. We found that MTZ mediated ablation of *s1026tEt*, *UAS-E1B:NTR-mCherry(c264)* double transgenic fish was lethal in 100% of animals. We therefore used a nitroreductase transgene of which the background muscle expression was suppressed by a 3′UTR: *UAS:BGi-epNTR-TagRFPT-utr.zb3*[57]. To overcome strong variegation of the existing allele (*y362*) in *s1026tEt* cells, we created new alleles via Tol2 mediated transgenesis. We injected *UAS:BGi-epNTR-TagRFPT-utr.zb3* together with *Tol2* mRNA into the TLN *s1026tEt* background. We outcrossed individual founders to TLN and raised transgenic RFP^+ offspring and control RFP^- siblings. At 19 d.p.f., we selected transgenic offspring of one founder for homogeneous RFP signal in the DT. This founder established the allele *mpn420* of which the expression is largely confined to the DT (Extended Data Fig. 8). Half of transgenic and control animals were randomly assigned to MTZ + DMSO versus DMSO-only treatment. We observed no lethality after ablation in this line. Analogous, non-transgenic siblings were also split into two groups for MTZ + DMSO versus DMSO-only treatment. MTZ had no detectable effect on non-transgenic animals and we subsequently pooled all three control conditions.

Laser ablations

Juvenile (20–23 d.p.f.) *elavl3:H2B-GCaMP6s* transgenic fish were embedded as described above, anesthetized with Tricaine and placed under a two-photon laser scanning microscope (Femtonics). The DT-BPN region within each brain was visually identified by the experimenter. A 20 µm ROI was specified on the DT-BPN region of each brain hemisphere and scanned with a 800 nm/400 mW laser beam for 30 ms. After each scan, one image was captured to observe the resulting damage and potential off-target effects. This procedure was repeated 7 ± 3 times until no more nuclei could be observed in the target region that could be targeted without blood vessel damage. Fish were removed from the embedding and anaesthesia immediately after ablation. One fish that did not start swimming within a few minutes was excluded from subsequent behaviour testing and analysis. Fish were allowed to recover for at least 16 h before they were tested in a shoaling assay as described above.

Social isolation

Individual eggs from *elav:H2B-GCaMP6s* incrosses were placed into small petri dishes at 0 d.p.f. The side walls of the dishes were taped to prevent visual contact between dishes. For controls, 15 eggs were placed in one small petri dish. Larvae were imaged at 7 d.p.f. As no brain stacks were acquired for these animals, anatomical DT masks were drawn for each fish manually. The response threshold for data analysis was adjusted to 50% due to a lower number of recorded neurons in single-plane imaging.

Statistical analysis

All analyses were performed in Python, using NumPy, Scipy, MatplotLib, Suite2p, Pandas and Scikit-learn. All statistical details are described in the figure legends and the Methods. All tests were two-tailed, unless noted otherwise. Error bars represent 1 s.d., unless noted otherwise. *N* denotes the number of animals, unless noted otherwise.

Data collection software

The following data collection software were used: Bonsai (v.2.4.1); Leica LAS X (v.3.5.7); and ScanImage (v.5.6).

Data analysis software

The following data analysis software was used: Python (v.3.9) with NumPy (v.1.21.0), Scipy (v.1.7.0), MatplotLib (v.3.4.2), Pandas (v.1.3.0) and additional packages (full python environments are available with our code on bitbucket); Ants (v.1.9); Suite2p (v.0.9.3); and ImageJ (v.1.53c).

Reporting summary

Further information on research design is available in the Nature Research Reporting Summary linked to this paper.

Data availability

All data to evaluate the conclusions in the paper and to reproduce the analysis are provided in the Article or made publicly available. Raw HCR data, two-photon time series for individual neurons and behaviour tracking data are available at Edmond (https://doi.org/10.17617/3.2QCFQP)[58]. The EM stack will be publicly available in a companion paper[35]. Source data are provided with this paper.

Code availability

Python scripts to recapitulate our data analysis are available at bitbucket (https://bitbucket.org/mpinbaierlab/kappeletal2022).

45. Vladimirov, N. et al. Light-sheet functional imaging in fictively behaving zebrafish. *Nat. Methods* **11**, 883–884 (2014).
46. Asakawa, K. & Kawakami, K. The Tol2-mediated Gal4-UAS method for gene and enhancer trapping in zebrafish. *Methods* **49**, 275–281 (2009).
47. Davison, J. M. et al. Transactivation from Gal4-VP16 transgenic insertions for tissue-specific cell labeling and ablation in zebrafish. *Dev. Biol.* **304**, 811–824 (2007).
48. Scott, E. & Baier, H. The cellular architecture of the larval zebrafish tectum, as revealed by Gal4 enhancer trap lines. *Front. Neural Circuits* **3**, 13 (2009).
49. Lopes, G. et al. Bonsai: an event-based framework for processing and controlling data streams. *Front. Neuroinform.* **9**, 7 (2015).

50. Gallois, B. & Candelier, R. FastTrack: an open-source software for tracking varying numbers of deformable objects. *PLoS Comput. Biol.* **17**, e1008697 (2021).
51. Avants, B. B. et al. A reproducible evaluation of ANTs similarity metric performance in brain image registration. *NeuroImage* **54**, 2033–2044 (2011).
52. Mueller, T. & Wullimann, M. F. *Atlas of Early Zebrafish Brain Development* (Academic Press, Elsevier, 2016).
53. Wullimann, M. F., Rupp, B. & Reichert, H. *Neuroanatomy of the Zebrafish Brain: A Topological Atlas* (Birkhäuser, 2012).
54. Bergmann, K. et al. Imaging neuronal activity in the optic tectum of late stage larval zebrafish. *J. Dev. Biol.* **6**, 6 (2018).
55. Pachitariu, M. et al. Suite2p: beyond 10,000 neurons with standard two-photon microscopy. Preprint at *bioRxiv* https://doi.org/10.1101/061507 (2017).
56. Januszewski, M. et al. High-precision automated reconstruction of neurons with flood-filling networks. *Nat. Methods* **15**, 605–610 (2018).
57. Marquart, G. D. et al. A 3D searchable database of transgenic zebrafish Gal4 and Cre Lines for functional neuroanatomy studies. *Front. Neural Circuits* **9**, 78 (2015).
58. Kappel, J. et al. Data from: visual recognition of social signals by a tecto-thalamic neural circuit. *Edmond* https://doi.org/10.17617/3.2QCFQP (2022).

Acknowledgements We thank E. Laurell and E. Kuehn for generating HCR stainings and for imaging marker lines for the mapzebrain atlas. Funding was provided by the Max Planck Society. J.K. was supported by a Boehringer Ingelheim Fonds graduate fellowship. J.L. was supported by a NARSAD Young Investigator Award. I.S. was supported by an Alexander von Humboldt foundation research fellowship.

Author contributions J.M.K. and K.S. performed two-photon imaging experiments. J.M.K. performed laser ablations, registration of two-photon and HCR data. M.J. segmented the EM volume with FFNs. D.F. proofread and traced presegmented EM data. I.S. performed HCR staining and imaging. F.S. generated the EM data and performed EM brain area registration. S.S. performed pilot HCR in situ experiments in juvenile fish. J.C.D. helped with the two-photon hardware and remote focusing, and advised on microscopy and analysis. J.L. performed behaviour experiments, transgenesis and brain area segmentation. J.M.K., K.S., D.F. and J.L. analysed the data. J.M.K., K.S., D.F., H.B. and J.L. interpreted the data. J.M.K., D.F., H.B. and J.L. wrote the paper with input from all of the authors. All of the authors reviewed and edited the manuscript. H.B. and J.L. supervised the project.

Funding Open access funding provided by Max Planck Society.

Competing interests The authors declare no competing interests.

Additional information

Supplementary information The online version contains supplementary material available at https://doi.org/10.1038/s41586-022-04925-5.

Correspondence and requests for materials should be addressed to Herwig Baier or Johannes Larsch.

Peer review information *Nature* thanks Lauren O'Connell and the other, anonymous, reviewer(s) for their contribution to the peer review of this work. Peer reviewer reports are available.

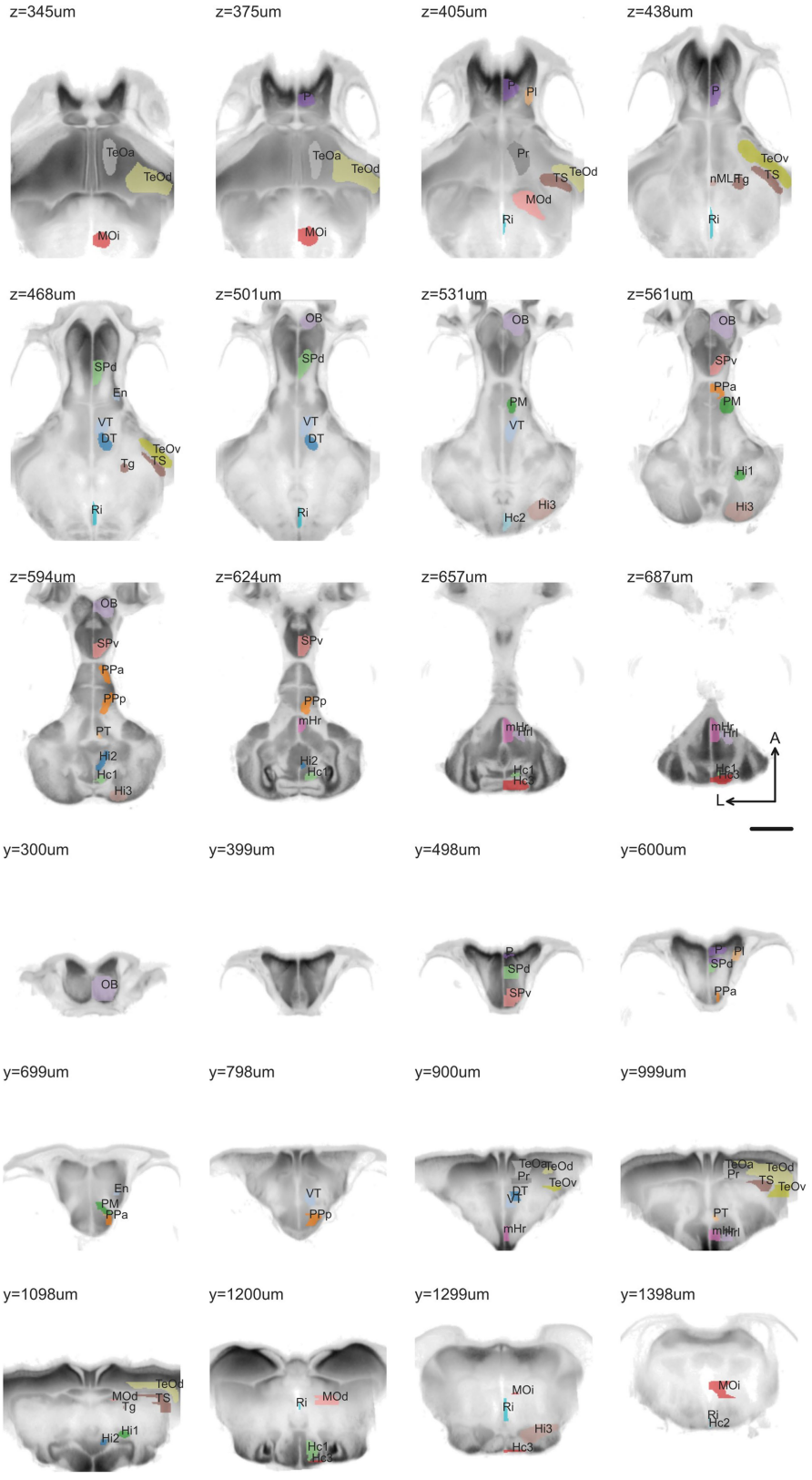

Extended Data Fig. 1 | Overview of all manually segmented *c-fos* activity clusters. Horizontal and coronal slices showing manually segmented *c-fos* activity clusters overlaid on the mean registered *elavl3* signal across all 28 animals. For visualization purposes, the *elavl3* signal was non-linearly transformed using a gamma adjustment of 0.5. Top three rows are horizontal sections, bottom three rows are coronal sections. Scale bar: 200 µm.

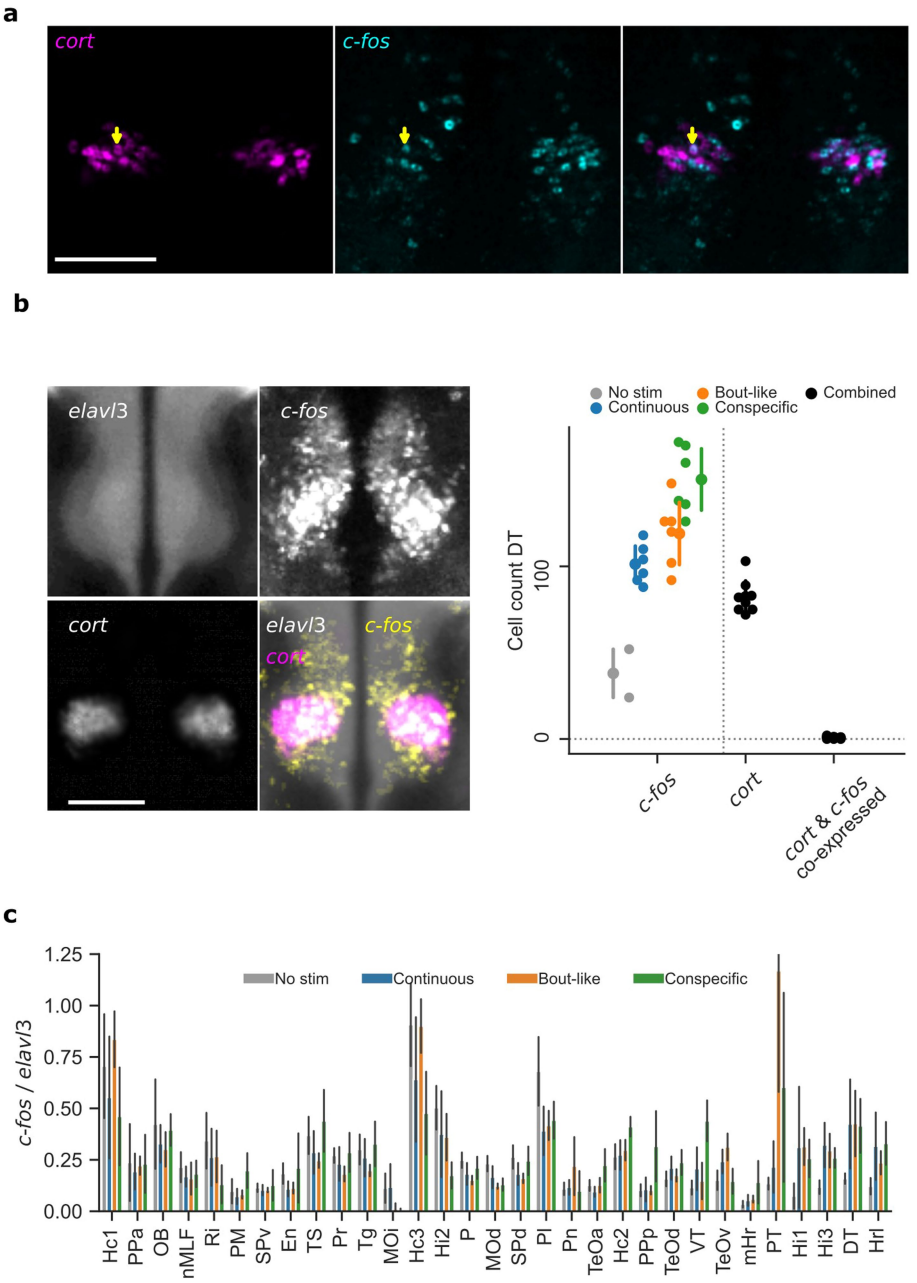

Extended Data Fig. 2 | Quantification of *c-fos* and *cort* HCR labelling. **a**, Dorsal thalamic plane showing HCR labelling of *c-fos* and *cort* in one animal after interaction with a bout-like motion dot stimulus. Expression occurs in the same regional cluster (DT) but only one cell expresses both markers (arrowhead). Representative for 6 examined animals. **b**, Left: Expression of *cort* and *c-fos* induction by shoaling stimuli localize to the same area. *elavl3*, *cort* and *c-fos* were co-labelled in the same animals. A single horizontal imaging plane at the centre of the DT cluster is shown. *elavl3* and *cort* channels are mean intensity, *c-fos* channel is maximum intensity over all 28 animals. Right: *c-fos*$^+$ and *cort*$^+$ cells were counted in the dorsal thalamus of N = 2,6,6,6,8,8 animals for no stim, continuous, bout like, conspecific, *cort*, and *cort* & *c-fos* groups, respectively. Data are mean ± 1SD. **c**, Normalized bulk *c-fos* signal for each activity cluster. Bars represent median±1SD, N = 6,8,6,8 animals for 'No stim', 'Continuous', 'Bout-like', 'Conspecific', respectively. Individual data points are available in the figure source data. Scale bars: 100 µm.

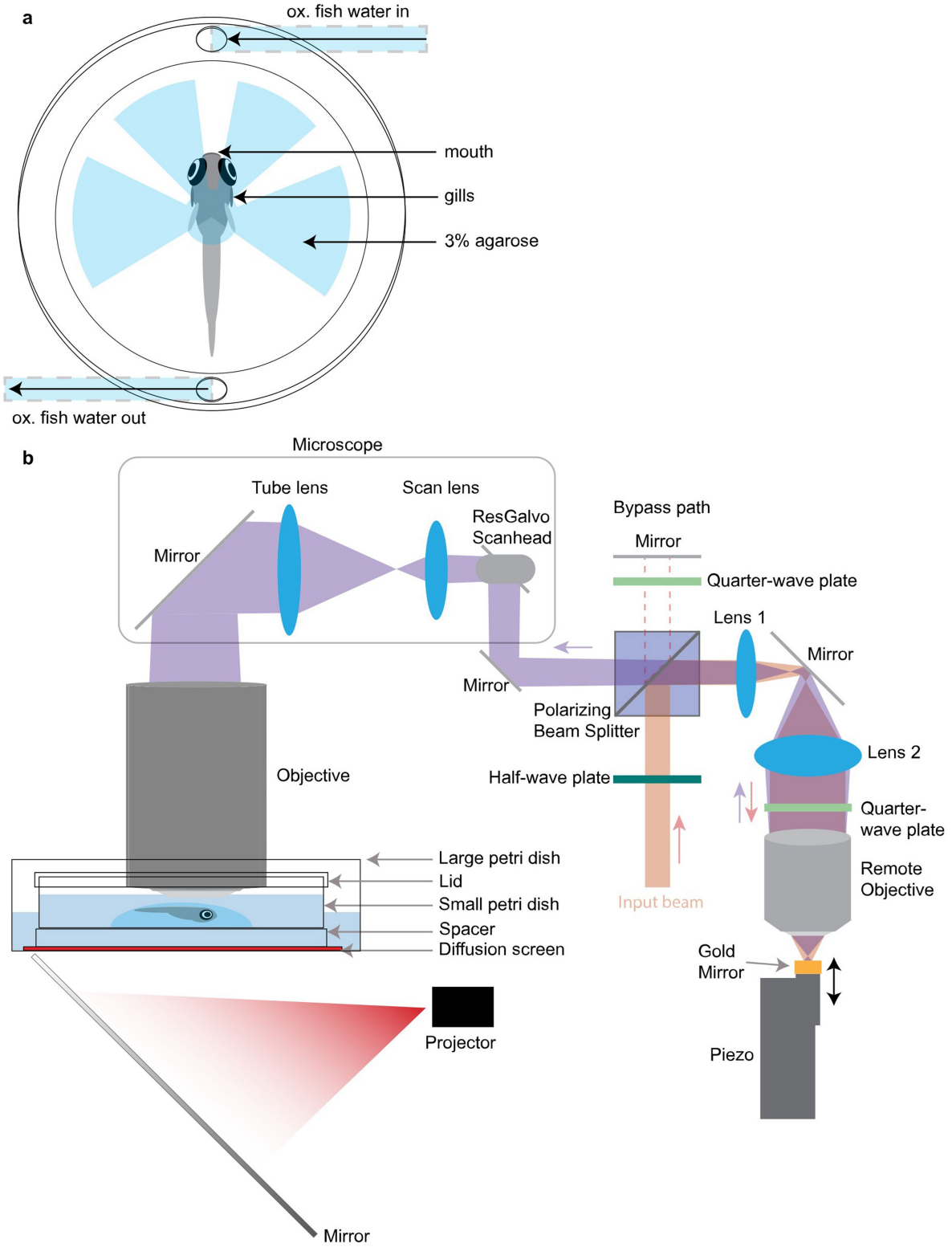

Extended Data Fig. 3 | See next page for caption.

Extended Data Fig. 3 | Schematic of the setup for calcium imaging. **a**, Top view of the embedding preparation for 2-photon imaging of juvenile zebrafish. To enable active respiration, agarose columns are cut out in front of the mouth and gills. The tail is also freed to improve oxygen uptake through the skin. Oxygenated water in the imaging chamber is constantly renewed with a peristaltic pump. **b**, Side view of the preparation and remote focusing system. The imaging chamber, consisting of a small petri dish, is placed in a large petri dish filled with water. Diffusive paper serving as a screen and a small spacer are placed between the large and small petri dish. The large petri dish is placed on a custom-made sample holder. A cold mirror is placed under the preparation to reflect projector images onto the screen. The input beam to the remote focusing system (red), passes through a half-wave plate and is reflected by a polarizing beam splitter. The beam is enlarged by two lenses, passes through a quarter-wave plate, and is focused by an objective onto a mirror mounted to a custom piezo stage. The piezo moves the mirror and thus adjusts the effective focal distance of the reflected beam, which ultimately changes the collimation of the beam at the main objective, changing the focus. The second pass through the quarter-wave plate on the return trip results in a change of polarization compared with the input beam, so the reflected beam now continues straight through the polarizing beam splitter, reaching the microscope. To bypass the remote focusing path, the input half-wave plate can be rotated so the input beam instead passes through the polarizing beam splitter, hits a mirror and passes through a quarter-wave plate twice, and then is reflected into the microscope. The detection path is standard and is not depicted.

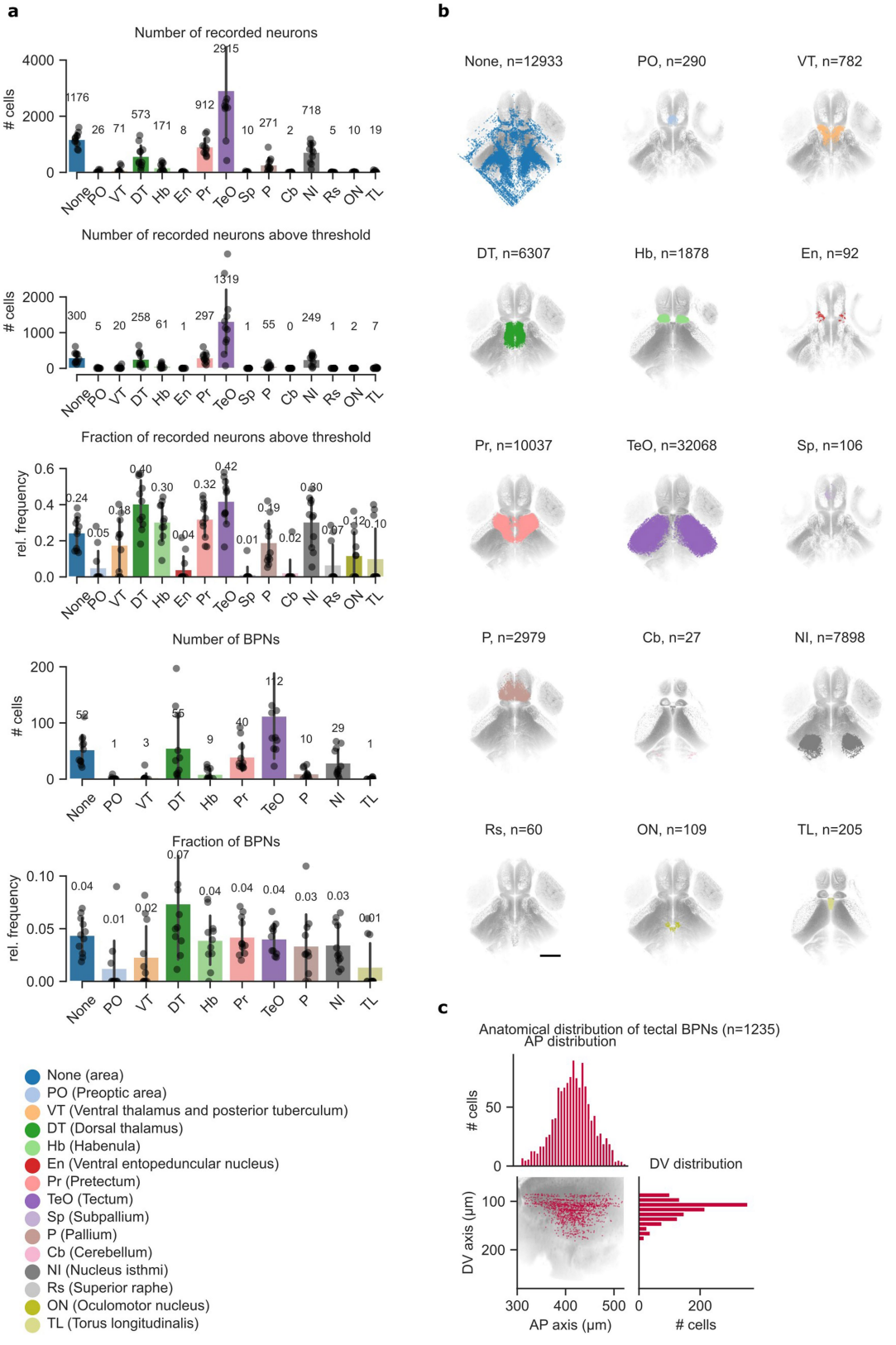

Extended Data Fig. 4 | BPN quantification across brain areas. a, Bar plots showing average numbers and fractions of neurons per fish per brain area. Bars indicate mean across animals, error bars represent 1SD. Dots show mean of individual fish. Top: Number of recorded neurons per brain area. Second: Number of recorded neurons above response threshold, see methods. Middle: Fraction of recorded neurons that surpassed response threshold per brain area. Fourth: Average number of BPNs per brain area. Bottom: Fraction of recorded neurons that were classified as BPNs per brain area. N = 11 animals. **b**, Anatomical location of recorded neurons in each brain area. Dots represent individual neurons. **c**, Distribution of tectal BPNs along anterior-posterior (AP) and dorso-ventral (DV) axis. Scale bar: 200 µm.

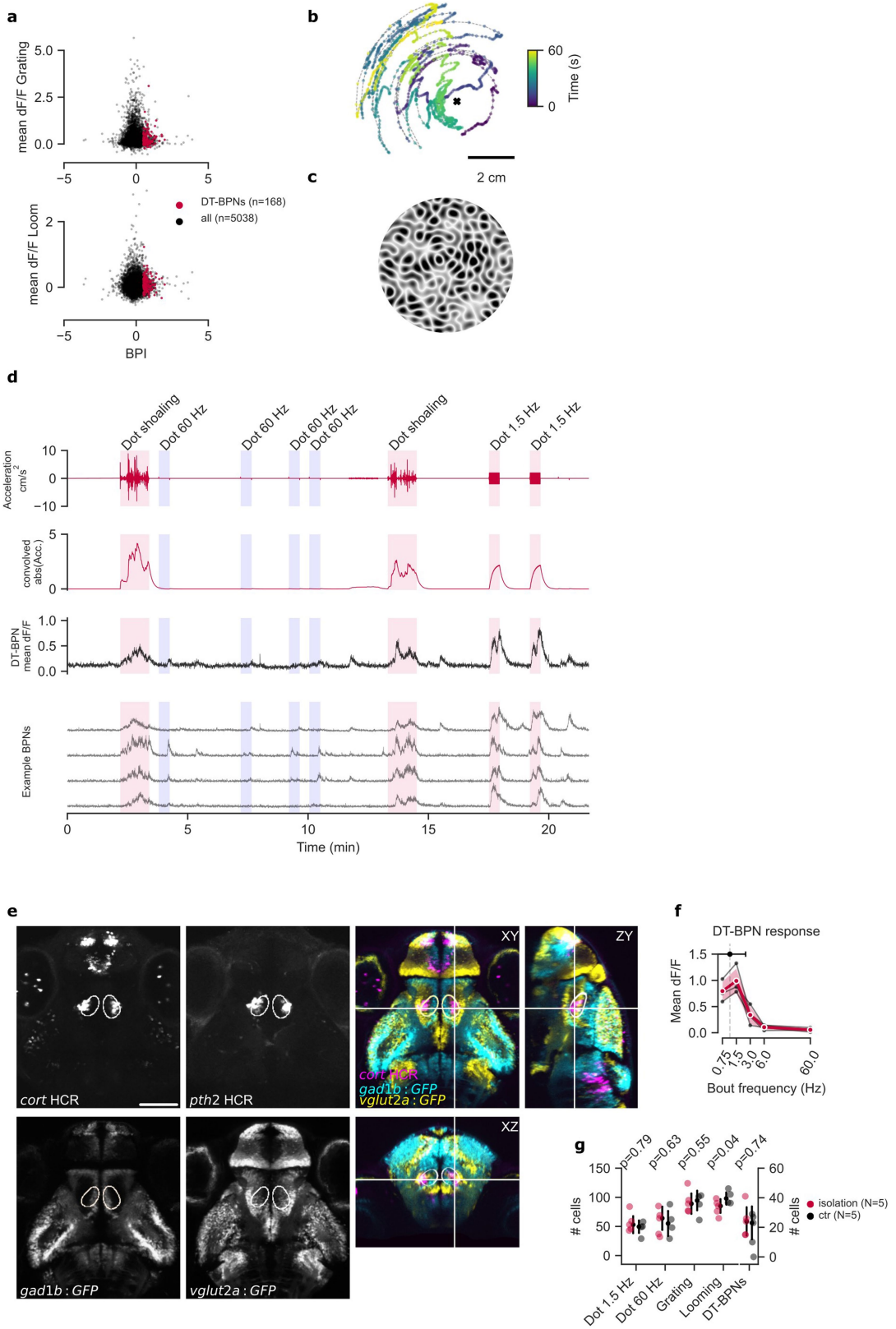

Extended Data Fig. 5 | See next page for caption.

Extended Data Fig. 5 | BPN response specificity in juvenile and larval animals. a, Responses of DT-BPNs (n = 56 ± 51) and all other recorded neurons above threshold (n = 1679 ± 1065) to looming and translational grating stimuli from 3 animals where these stimuli were included in the protocol. DT-BPNs are not strongly activated by either of the two control stimuli. **b**, Dot shoaling stimulus. Dot position recapitulates the location of a conspecific relative to a focal fish facing up. Cross marks location of the focal fish. **c**, Whole-field motion stimulus used in Fig. 2i. **d**, DT-BPNs respond to dot shoaling stimulus. Top red trace shows instantaneous dot stimulus acceleration, bottom red trace the same time series convolved with GCaMP6s kernel (see methods). Dot shoaling, 1.5 Hz and 60 Hz stimuli were shown in pseudo-random order as indicated. Median trace represents n = 84 DT-BPNs from one fish, including four representative neurons shown below. **e**, Expression of *cort*, *pth2*, *gad1b* and *vglut2a* defines the location of the larval BPN KDE as dorsal thalamus. *gad1b* positive 'stripe' of cells near the midline marks the dorsal edge of VT. Left four panels show single planes. Right shows merged orthogonal views. Each channel shows mean expression over multiple individual fish registered to the mapzebrain atlas. *cort* and *pth2* are HCR labels, mean of N = 3 animals each. *gad1b* and *vglut2a* are Gal4 enhancer trap lines driving expression of GFP, N = 5 animals each. Also see Video S1. **f**, Larval DT-BPN (n = 51 ± 14 neurons per fish, N = 4 animals) tuning curve to stimulus frequencies from 0.75 to 60 Hz shown in red. Mean tuning peak of individual neurons (shown above) was 1.1 Hz ± 1.3 Hz. Black lines represent means of individual animals. Data from a subset of all animals in Fig. 2j with number of recorded DT-BPNs > 30. **g**, Number of neurons in DT responding to different visual stimuli of larvae raised in social isolation compared to group-raised larvae (N = 5 animals per group). Number of responsive neurons to bout-like motion as well as the number of DT-BPNs are not significantly different in socially isolated animals. Error bars: 1SD. P-value: two-tailed student's t-test, no corrections. Scale bars: b, 2 cm; e, 100 µm.

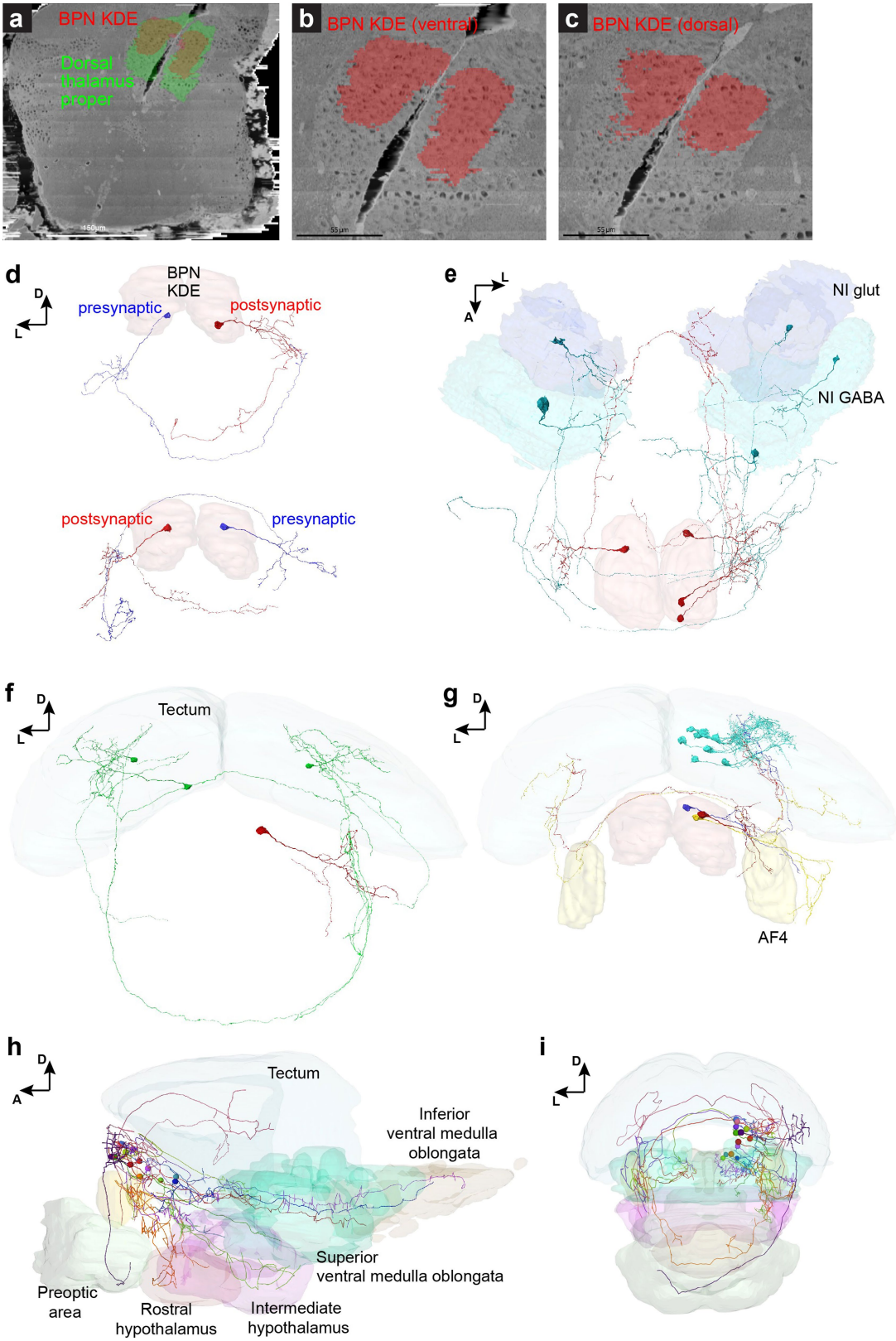

Extended Data Fig. 6 | Representative example neurons and brain areas in the EM dataset. a-c, Registration of mapzebrain regions to the EM dataset. Shown are top-views of the kernel density estimation for bout-preference neurons (red) inside the dorsal thalamus proper (green, a) and at different coronal planes (b, c). N = 1 EM stack. **d**, Frontal views of the BPN KDE in EM reconstructions showing two examples (top and bottom) for synaptically connected putative BPN partners across brain hemispheres. **e**, Dorsal view of three putative BPNs (red) and their presynaptic partners in the nucleus isthmi (glutamatergic and GABAergic domains are annotated). **f**, A single putative BPN (red) receives ipsi- and contralateral synaptic input from at least three identified tectal PVPNs (green). **g**, Three examples for putative BPNs (red, orange, purple) with axonal projections to the ipsi- and contralateral tectum. Eight tectal PVINs (cyan), which are postsynaptic to the red putative BPN are shown. **h-i**, Mapzebrain atlas showing single cells in the BPN KDE and their targeted brain regions in lateral (h) and frontal (i) views. AF4 (yellow) is shown as a reference. Scale bars: a, 150 µm; b, c, 55 µm.

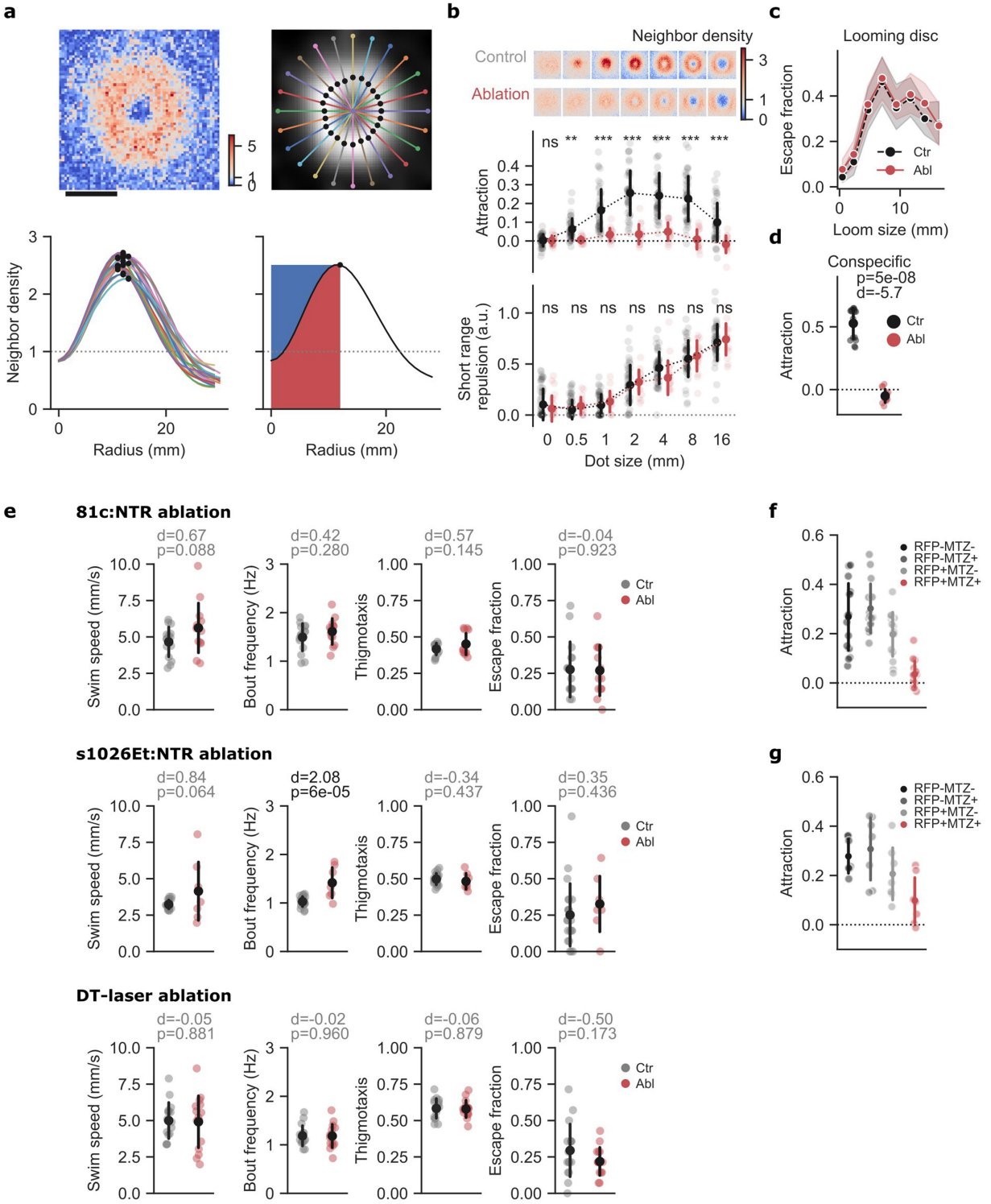

Extended Data Fig. 7 | See next page for caption.

Extended Data Fig. 7 | Additional behavioural analysis of ablated animals. **a**, Definition of short-range repulsion. Top left shows a representative neighbour map for one of 45 similar control animals interacting with a dot of 4 mm diameter. Colour map as in Fig. 4e. Top right and bottom left show 24 radial line scans of smoothed neighbour density. Each scan begins at the centre of the map. Black dots label the maximum of each scan. Bottom right shows the mean of all line scans in black. Repulsion is quantified as the area above the mean line, left of the peak (blue shading). This defines the reduction of attraction at the centre of the map. Dotted line in bottom panels indicates baseline neighbour density (random distribution). **b**, Attraction and neighbour density are strongly reduced in *81c:NTR* ablated animals. Short-range repulsion is intact. N = 15 ablated, 45 control animals. Data represent individual animals and mean (attraction) or median (repulsion). Neighbour maps show mean probability of finding the stimulus in space with the focal animal at the centre of the map, heading up. Values represent ratios, relative to time-shuffled data. Each map is 60 x 60 mm. ***: $p < 0.001/7$, **: $p < 0.01/7$, ns: $p > 0.05/7$. Two-sided student's t-test for attraction, Mann-Whitney U test for repulsion, alpha values Bonferroni corrected for 7 comparisons. See figure source data for individual p-values. **c**, Loom induced startle responses are intact in *81c:NTR* ablated animals. Same animals as in Fig. 4c, d. Data represents mean, shading represents 1SD. N = 13 ablated, N = 15 control animals. **d**, Shoaling with real conspecifics is disrupted in *81c:NTR* ablated animals. Fish as in Fig. 4c, d +1 additional animal per group tested in pairs. N = 14 ablated animals, tested as 7 pairs, N = 16 control animals, tested as 8 pairs. **e**, Quantification of control behaviours in animals shown in Fig. 4c, d, i, and k. Refer to legend of Fig. 4 and figure source data for additional statistical information. **f**, Attraction shown separately for 81c:NTR-RFP ablation +/− RFP and MTZ +/− control groups, same data as 2 mm dots in b. RFP: red fluorescent protein indicates expression/ no expression of nitroreductase, respectively. MTZ: Metronidazole incubation/ DMSO control, respectively. N = 15 animals in each group. **g**, Attraction shown separately for s1026tEt:NTR-RFP ablation +/− RFP and MTZ +/− control groups, same data as in e. N = 7 animals in each group. Data in d-g show individual animals or pairs and mean. Error bars are 1SD. p: Two-sided student's t-tests, uncorrected. d: Cohen's *d*. Scale bar: 20 mm.

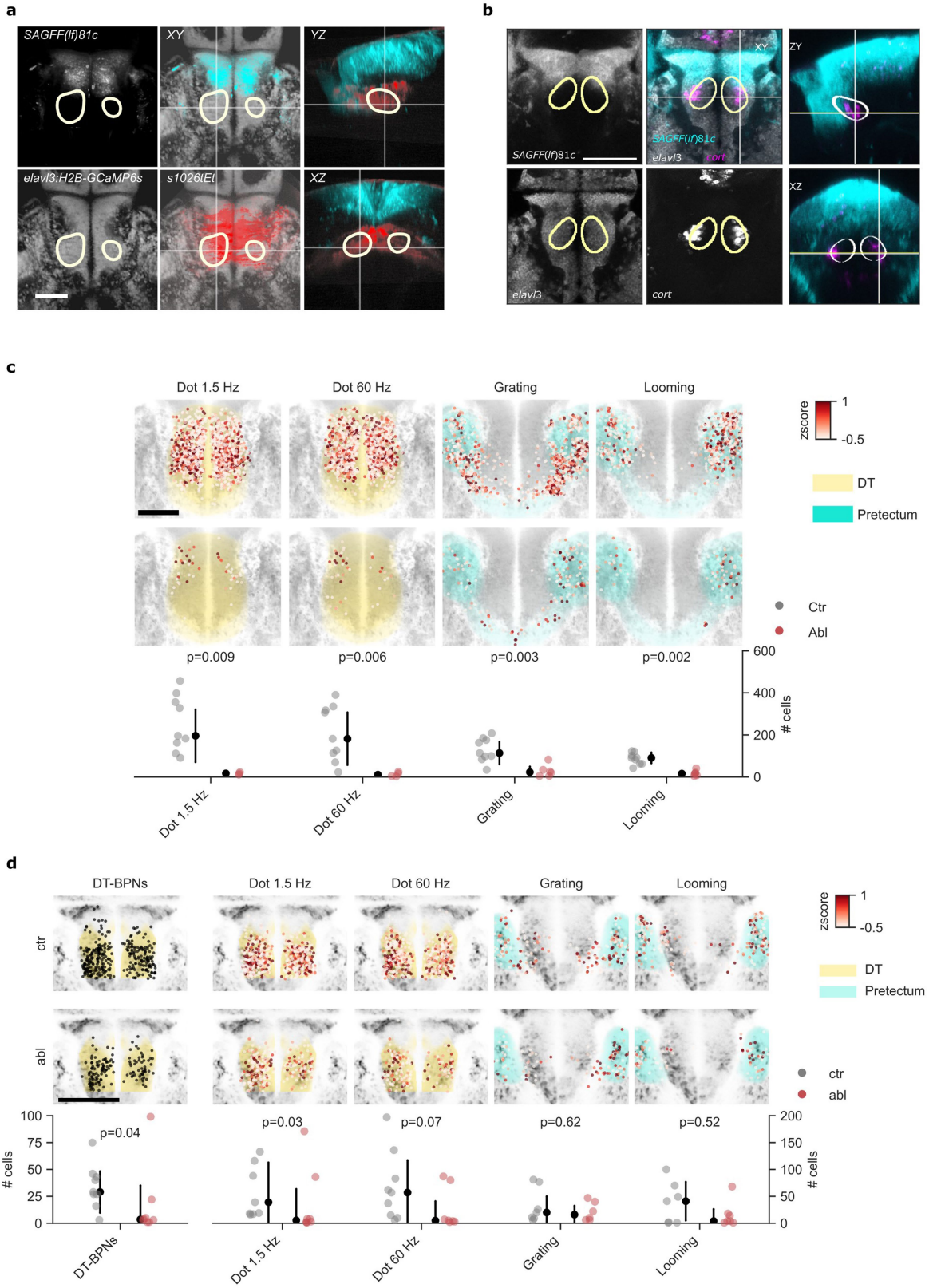

Extended Data Fig. 8 | See next page for caption.

Extended Data Fig. 8 | Evoked neuronal activity in *SAGFF(lf)81c* ablated animals. a, Juvenile expression of *SAGFF(lf)81c:Gal4*, *UAS:NTR-mCherry* and *s1026tEt, UAS:NTR-mCherry* relative to BPN KDE (yellow outline). Markers were imaged in separate 21 dpf fish and registered to the juvenile standard brain. *SAGFF(lf)81c*: average of 3 animals. *s1026tEt:* average of 2 animals. *elavl3:H2B-GCaMP6s:* mapzebrain reference channel. Merged view is shown in 3 orthogonal axes. White crosshairs indicate the orthogonal planes. **b**, Larval expression of *SAGFF(lf)81c:Gal4*, *UAS:NTR-mCherry* relative to BPN KDE (yellow outline) and *cort* HCR. Markers were imaged in separate 5–7 dpf fish and registered to the mapzebrain standard brain. *81c*: average of 4 animals *SAGFF(lf)81c:Gal4, UAS:NTR-mCherry*. *elavl3*: mapzebrain reference channel. *cort*: average of 3 animals, HCR label. Merged view is shown in 3 orthogonal planes. White crosshairs indicate the orthogonal planes. Also see Video S3. **c**, Additional analysis of Fig. 4e–h. Number of neurons with mean dF/F above the 90th percentile in DT for bout-like dot motion, continuous dot motion, as well as in pretectum for translational gratings and looming stimuli of *81c:NTR* ablated and control animals, respectively. Ablated animals show significantly less responding neurons for all stimuli compared to controls. Individual data points denote animals. Color code of individual neurons is z-scored mean dF/F per stimulus. N = 7 ablated, 9 control animals. **d**, Same experiment as in Fig. 4e–h, and Extended Data Fig. 8c, but in 7dpf larvae. Here, significant reduction of responding neurons in *81c:NTR* ablated animals is only observed for DT-BPNs and bout-like dot motion in DT, whereas continuous dot motion, translational gratings and looming do not evoke significantly less responses in the pretectum of ablated animals. N = 8 ablated, 9 control animals. Error bars: 1SD. Scale bars: a, b, 100 µm; d. p-values in c,d result from two-sided Mann-Whitney U test (uncorrected).

2.2 Positional information drives distinct traits in transcriptomically identified neuronal types

Inbal Shainer*, **Johannes M. Kappel***, Eva Laurell, Joseph C. Donovan, Martin Schneider, Enrico Kuehn, Irene Arnold-Ammer, Manuel Stemmer, Johannes Larsch, Herwig Baier

*These authors contributed equally to this work

This article is not published yet.

Positional information drives distinct traits in transcriptomically identified neuronal types

Inbal Shainer*[1], Johannes M. Kappel*[1], Eva Laurell[1], Joseph C. Donovan[1], Martin Schneider[1], Enrico Kuehn[1], Irene Arnold-Ammer[1], Manuel Stemmer[1], Johannes Larsch[1], Herwig Baier[1]

[1]Max Planck Institute for Biological Intelligence, Am Klopferspitz 18, 82152 Martinsried, Germany.

* These authors contributed equally to this work.

Correspondence: herwig.baier@bi.mpg.de

Summary

Neuronal phenotypic traits such as morphology, connectivity, and function are dictated, to a large extent, by a specific combination of differentially expressed genes. Clusters of neurons in transcriptomic space correspond to distinct cell types and in some cases (e.g., *C. elegans* neurons[1] and retinal ganglion cells[2,3]) have been shown to share morphology and function. The vertebrate optic tectum is composed of a spatial array of neurons that transform visual inputs into motor outputs. While the visuotopic map is continuous, subregions of the tectum are functionally specialized[4,5]. To uncover the cell-type architecture of the tectum, we transcriptionally profiled its neurons, revealing approximately 60 cell types that are organized in distinct anatomical layers. We then measured the functional tuning of thousands of neurons to a battery of ethologically relevant visual stimuli by two-photon calcium imaging and matched them to their cell-type identities. Surprisingly, we found that neurons that are transcriptionally similar can diverge functionally and morphologically. Incorporating the spatial coordinates of neurons within the tectal volume as a classifier revealed functionally defined subclusters within individual transcriptomic clusters. Our findings suggest that extrinsic, position-dependent factors expand the phenotypic repertoire of genetically similar neurons.

Main

Neurons can be grouped into types and subtypes by the complement of genes they express[6–8]. The cell type-specific transcriptome (t-type) is believed to encode the genetic instructions for a neuron's differentiation trajectory during development and thus its morphology (m-type), connectivity and function (f-type). For example, each of the 118 anatomically distinct neuron types in the roundworm *C. elegans* express a unique, sparse combination of transcription factors, which regulate downstream genes, thus shaping the neuron's phenotype and contribution to network function[1,9]. Similarly, in the mouse visual cortex, morpho-electric properties measured in tissue slices were found to be relatively homogeneous within individual t-types[10,11].

However, the dogmatic view of "t-type = m-type = f-type" is problematic, as functional responses and dendritic arbor elaborations are often shaped by modulatory influences and individual experience[12,13]. For instance, GABAergic interneurons in the visual cortex have been found to exhibit tuning properties dependent on behavioral state rather than t-type[14]. Moreover, it was recently shown that mouse cortical neurons of the same t-type vary strongly in their functional tuning[15], as well as in their m-type, showing divergent long range projections and local connectivity[16]. It is therefore essential to determine the extrinsic factors that influence the expression of a neuron's phenotype and how these interact with the transcriptome.

In this study, we examine if the interplay between transcriptome, development and topography plays a role in shaping morphological and functional neuronal phenotypes. The zebrafish optic tectum (OT) receives topographically organized input from retinal ganglion cells (RGCs) along the anterior-posterior (AP) and dorsal-ventral (DV) axes[17,18]. In its superficial-to-deep (SD) dimension, which runs orthogonally to the retinotopic axes, the OT contains a neuropil layer, in which RGC axons form synapses with the dendrites of tectal neurons, and a cell-body layer, the stratum periventriculare (SPV). Cellular birthdating studies have shown that newborn neurons are added to the OT from the ventricular zone, with older neurons being gradually displaced into the SPV as they mature and extend neurites into the neuropil[19,20]. Extrinsic factors, including morphogens and chemotropic cues, change with location and over the course of development[21]. Moreover, interactions with other cells are certain to vary along all three axes of the OT. These cues may affect the neurons' t-, m- and f-types. Indeed, taking advantage of systematic functional imaging of neuronal responses followed by transcriptional profiling[22], we discovered here that a combination of both transcriptomic identity and cell-body position in this topographically structured tissue are important determinants of a neuron's phenotype.

Diversity of neuronal and non-neuronal tectal cell types

To characterize the t-type composition of the zebrafish OT, we performed droplet-based single-cell RNA sequencing (scRNA-seq; see Methods; Extended data Fig. 1). We grouped 20,197 sequenced cells according to their transcriptomes into 30 major clusters (Fig. 1a), which corresponds to 3.5x coverage

of cells in a single tecta (~5800 cells [4]). Based on differentially expressed (DE), cluster-specific genes (Supplementary Table 1, Extended data Fig. 2-3), we identified four clusters of progenitor cells, three clusters of radial glia, fourteen clusters of neurons and nine additional non-neuronal populations (Extended data Fig. 2-3).

The postmitotic neurons (>13,500 cells, expressing *elavl3*) were reclustered (Fig. 1b) and separated into inhibitory (*gad1b*+) and excitatory (*gad1b*–) neurons (Fig. 2c, Extended data Fig. 3e-d). This resulted in 29 excitatory t-types (clusters: c21, e1-e4, e6-e29; total number of cells = 6,182) and 29 inhibitory t-types (clusters: n24, i2-8, i10-30; total number of cells = 2,060). For 27 neuronal types, we identified single DE genes that serve as mutually exclusive markers; for the remaining types, sparse combinations of DE genes suffice for an unambiguous definition (Fig. 1d-e, Supplementary Table 1). Overall, we identified 58 t-types in the larval zebrafish OT.

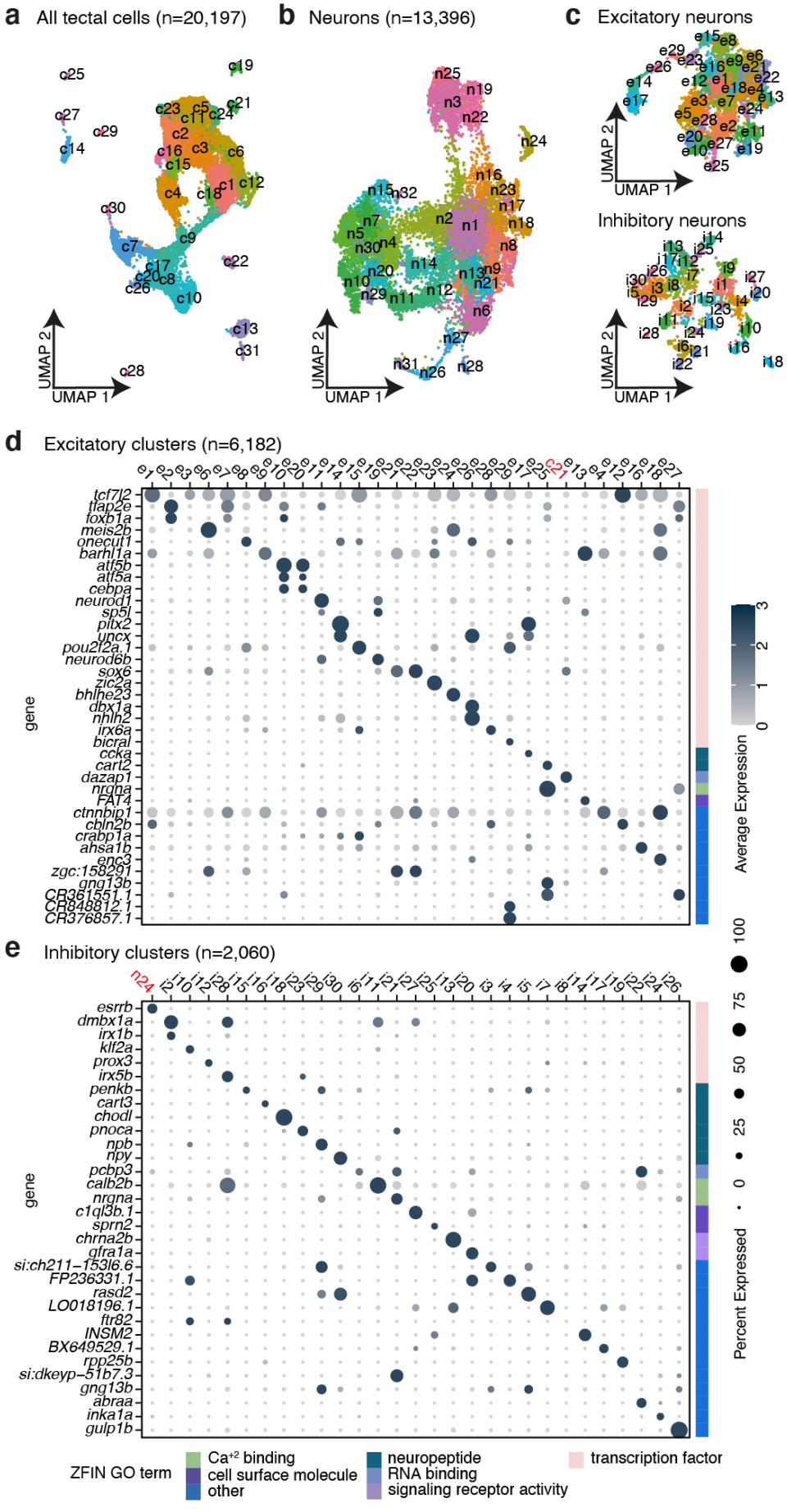
a All tectal cells (n=20,197)
b Neurons (n=13,396)
c Excitatory neurons
Inhibitory neurons
UMAP 1
UMAP 2
d Excitatory clusters (n=6,182)
gene
Average Expression
e Inhibitory clusters (n=2,060)
Percent Expressed
ZFIN GO term
Ca+2 binding
cell surface molecule
other
neuropeptide
RNA binding
signaling receptor activity
transcription factor

Fig. 1. scRNA-Seq of the optic tectum reveals a multitude of neuronal types.

- **a.** The sequenced cells were clustered according to similarity of gene expression, 31 different clusters were identified. Each dot represents a single cell, color coded according to the cluster.
- **b.** Neurons (clusters expressing *elavl3*) were subset and reclustered to further identify the variety of neuronal types.
- **c.** The neuronal clusters were separated into excitatory and inhibitory cells according to *gad1b* expression (Extended data Fig. 3) and further clustered.
- **d.** Dotplot of the highly DE genes for each of the excitatory cell types (clusters: c21, e1-e4, e6-e29). The DE genes were grouped according to their molecular function and annotated according to ZFIN GO terminology[23].
- **e.** Dotplot of the highly DE genes for each of the inhibitory cell types (clusters: n24, i2-8, i10-30).

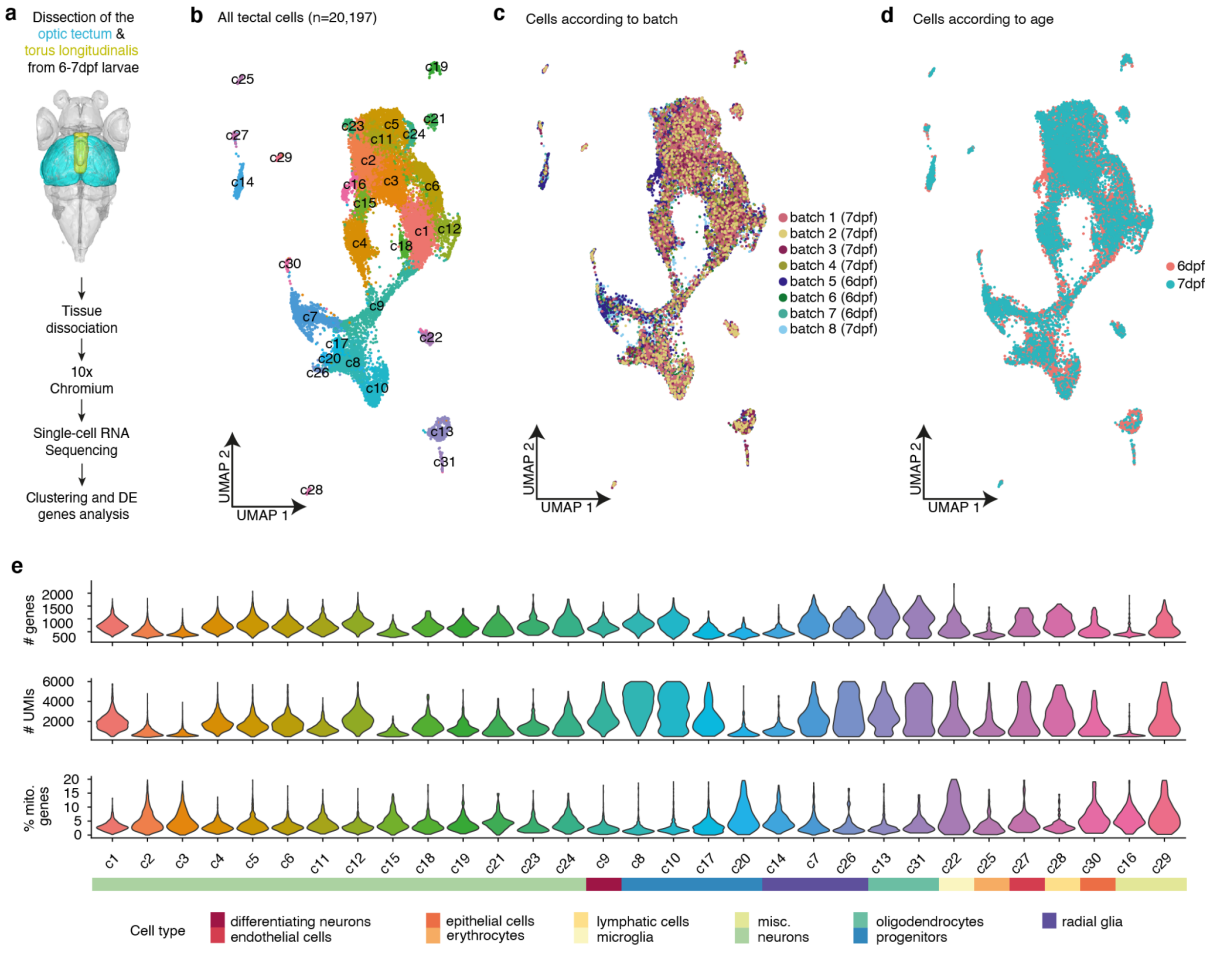

Extended data Fig. 1. QC of the scRNA-Seq clustering analysis.

- **a.** Experimental procedure: the optic tectum and the torus longitudinalis (TL) were dissected from 6-7 dpf WT larvae in eight experimental batches. The cells were dissociated, single-cell barcoded cDNA was generated using the 10x Chromium system and sequenced.

b. After batch correction using Harmony[24] and removal of IEGs (Methods), we identified a total of 31 clusters of cells. Each dot represents a single cell, color coded according to the cluster.

c. Same UMAP as in **b**, color coded according to the batch. Clusters include cells from all batches. Cluster c16 was only represented in batch 5, and expressed genes typically associated with the eye (Extended data Fig. 3). We therefore treated these cells as a contamination and omitted cluster c16 from further analysis.

d. Same UMAP as in **b**, color coded according to the larvae age. The larval age did not affect the clustering analysis, as clusters include cells from all ages.

e. QC metric of the sequenced cells after filtration, according to cluster. Cells were filtered (see Methods) in order to remove outliers that contain either low or high number of genes and UMI (representing either poorly sequenced cells or doublets), as well as cells containing high percentage of mitochondrial genes (representing stressed cells). Different cell types contained different levels of genes and UMIs, matching their biological profile (for example high levels of UMIs in some of the progenitor cells).

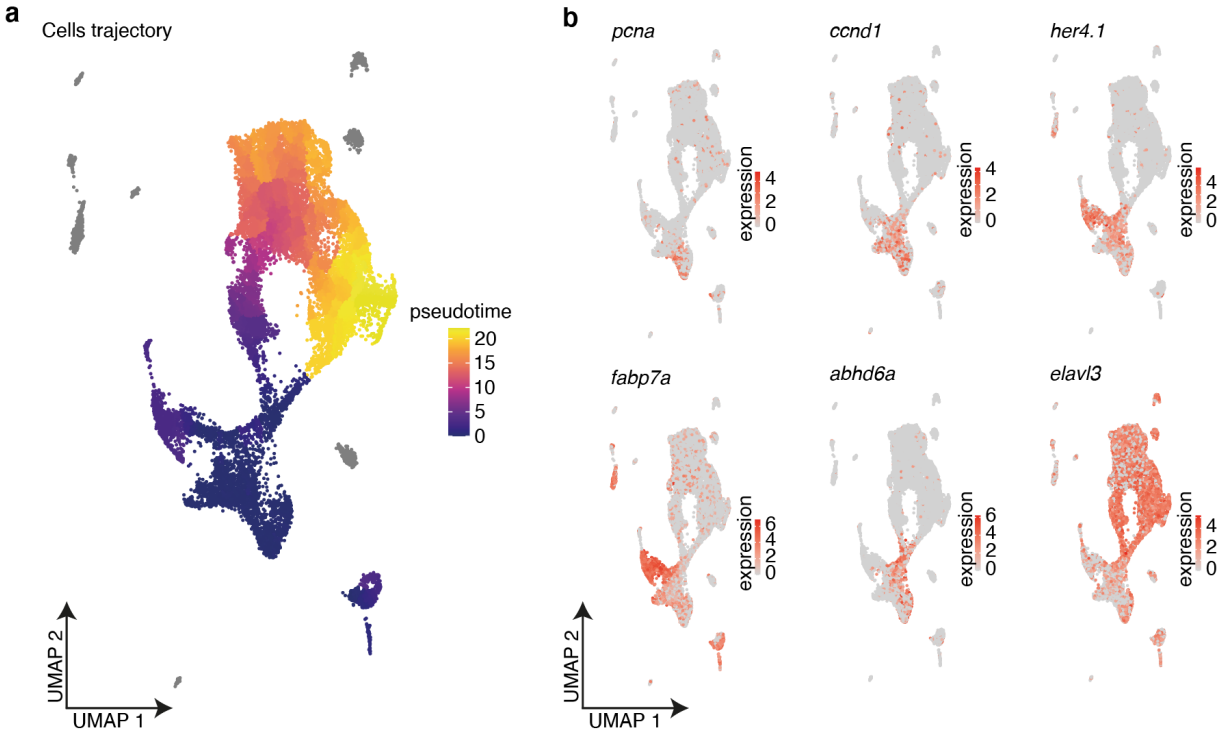

Extended data Fig. 2. Pseudotime analysis

a. Pseudotime analysis was performed with Monocle3[25]. Cells belonging to clusters c8 and c10 were identified as progenitor cells and defined as the root point. These cells expressed proliferating cell nuclear antigen (*pcna*), a key component of DNA replication machinery and a marker of the G1 phase[26], and *ccnd1*, a member of the cyclin family that regulates the cell-cycle transition from G1 to S phase[27]. Cells are color coded according to their pseudotemporal ordering.

b. Expression patterns of selected marker genes, representing the different stages of proliferation and differentiation. The markers *fabp7a* and *her4.1* are typically expressed in radial glia[28,29]. *Abhd6a (abhydrolase domain containing 6, acylglycerol lipase a*) is homologous to the mammalian *abhd6,* which is involved in regulation of synaptic transmission and expressed in progenitors as well as in adult neurons[30], and *elavl3* is expressed in committed neurons.

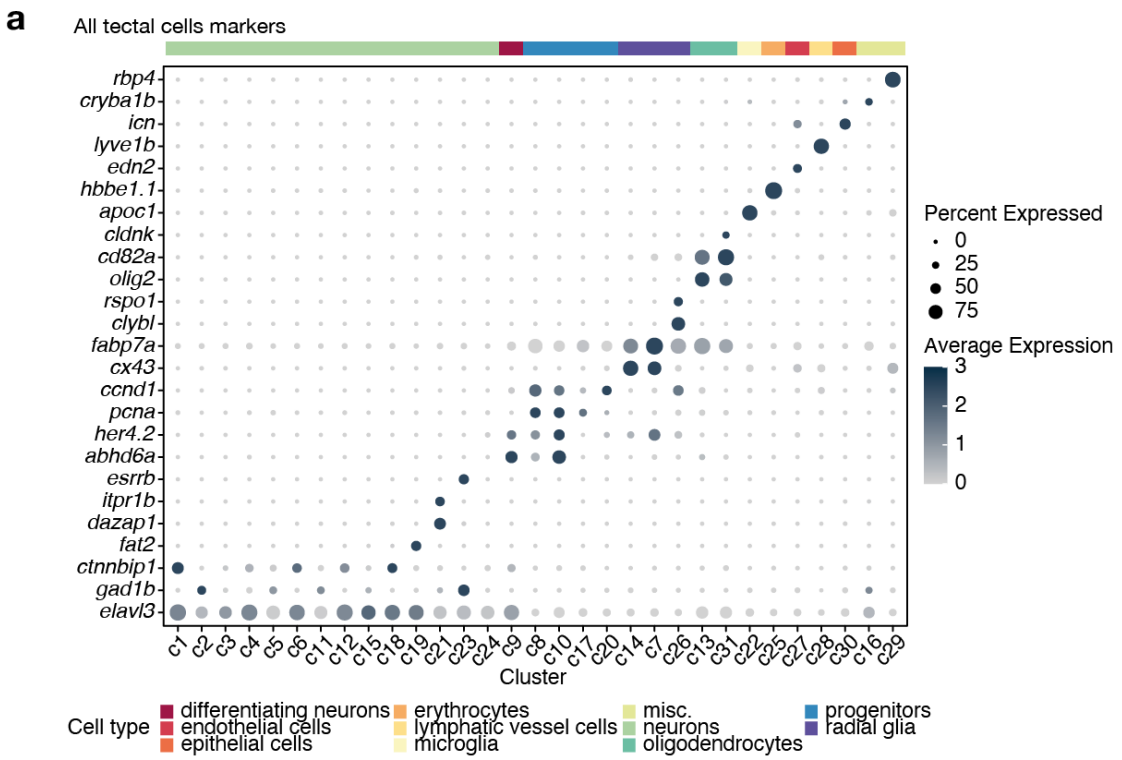
a
All tectal cells markers
rbp4
cryba1b
icn
lyve1b
edn2
hbbe1.1
apoc1
cldnk
cd82a
olig2
rspo1
clybl
fabp7a
cx43
ccnd1
pcna
her4.2
abhd6a
esrrb
itpr1b
dazap1
fat2
ctnnbip1
gad1b
elavl3
c1 c2 c3 c4 c5 c6 c11 c12 c15 c18 c19 c21 c23 c24 c9 c8 c10 c17 c20 c14 c7 c26 c13 c31 c22 c25 c27 c28 c30 c16 c29
Cluster
Percent Expressed
0
25
50
75
Average Expression
3
2
1
0
Cell type
differentiating neurons
endothelial cells
epithelial cells
erythrocytes
lymphatic vessel cells
microglia
misc.
neurons
oligodendrocytes
progenitors
radial glia

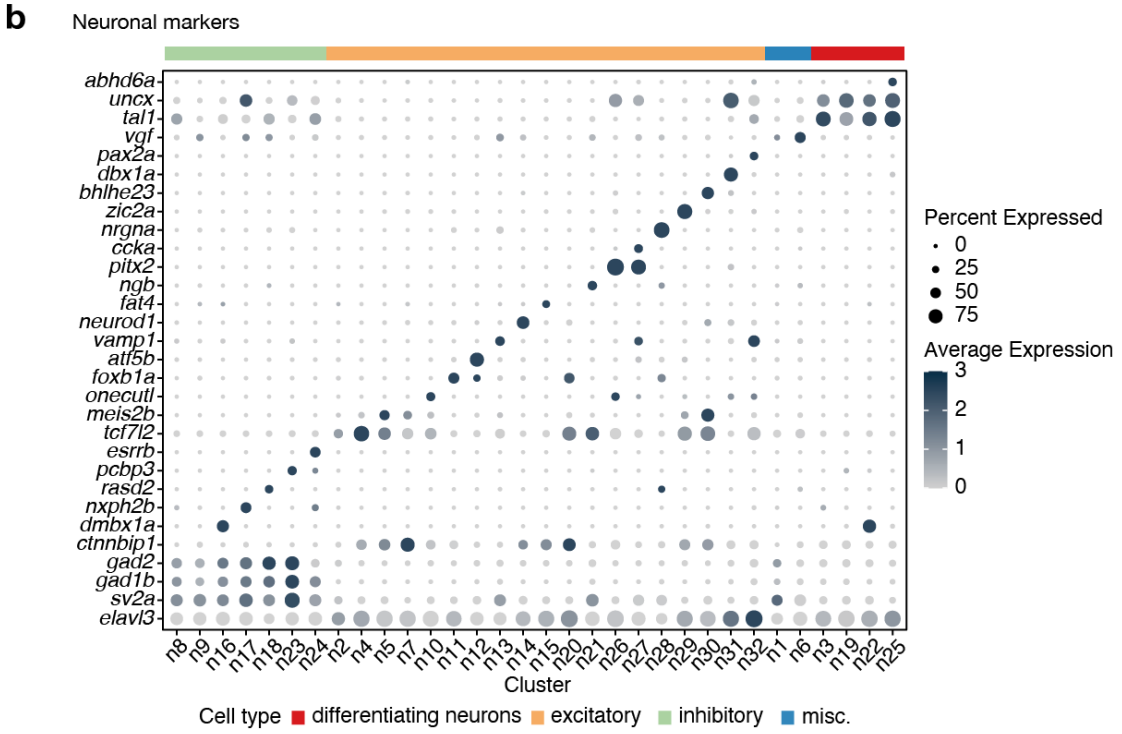
b
Neuronal markers
abhd6a
uncx
tal1
vgf
pax2a
dbx1a
bhlhe23
zic2a
nrgna
ccka
pitx2
ngb
fat4
neurod1
vamp1
atf5b
foxb1a
onecut1
meis2b
tcf7l2
esrrb
pcbp3
rasd2
nxph2b
dmbx1a
ctnnbip1
gad2
gad1b
sv2a
elavl3
n8 n9 n16 n17 n18 n23 n24 n2 n4 n5 n7 n10 n11 n12 n13 n14 n15 n20 n21 n26 n27 n28 n29 n30 n31 n32 n1 n6 n3 n19 n22 n25
Cluster
Percent Expressed
0
25
50
75
Average Expression
3
2
1
0
Cell type
differentiating neurons
excitatory
inhibitory
misc.


c
Excitatory
e1 e2 e3 e4 e5 e6 e7 e8 e9 e10 e11 e12 e13 e14 e15 e16 e17 e18 e19 e20 e21 e22 e23 e24 e25 e26 e27 e28 e29
gad1b
elavl3
Average Expression
3
2
1
0
d
Inhibitory
i1 i2 i3 i4 i5 i6 i7 i8 i9 i10 i11 i12 i13 i14 i15 i16 i17 i18 i19 i20 i21 i22 i23 i24 i25 i26 i27 i28 i29 i30
slc17a6a
gad1b
elavl3
Percent Expressed
25
50
75

Extended data Fig. 3. Cell type classification

- **a.** Dotplot of the highly differentially expressed genes for each tectal cluster. Clusters were grouped according to cell function. Cluster c19 cells expressed torus longitudinalis marker genes and were therefore omitted from downstream tectum analyses. The composition of cell types we identified differed from a recent study characterizing the zebrafish OT [31]. In that study, FACS sorting of tectal neurons from a specific transgenic line was used prior to the scRNA-seq, most likely biasing the sequenced data toward cells only labeled by that line[31].
- **b.** Dotplot of the highly differentially expressed genes for each neuronal cluster. Clusters were grouped according to transmitter use and developmental stage. Several clusters of neurons expressed the transcription factors *uncx* and *tal1,* which are typically expressed in differentiating neurons[32–34].
- **c.** Based on *gad1b* expression, we separated the inhibitory and excitatory clusters, and reclustered them. We still detected *gad1b* as a marker gene of cluster e5. This cluster most likely represents cells contaminated with external RNA, and therefore was omitted from the final excitatory cell type analysis.
- **d.** Two of the inhibitory clusters, i1 and i9, expressed the glutamate transporter *slc17a6a* (*vglut2b)*, and therefore was omitted from the final inhibitory cell type analysis.

Neuronal cell types are non-uniformly distributed in the tectum

To test whether t-types are spatially organized relative to the three axes of the OT volume (Fig. 2), we selected DE genes, which were expressed in a single or a small number of clusters, and examined their spatial expression patterns using multiplexed RNA in situ hybridization chain reaction (HCR) (Extended data Fig. 4). We co-registered the HCR patterns within the standard coordinates of the *mapzebrain.org* atlas[35,36] and measured their expression levels at the same transverse and coronal sections (Fig. 2, Extended data Fig. 5).

This visualization revealed that genetically identified neurons are frequently enriched in specific domains along the SD axis, which is orthogonal to the visual map. Most prominently, GABAergic and glutamatergic neurons largely populate the deepest and most superficial layer of the SPV, respectively, with cholinergic neurons sandwiched between them (Extended data Fig. 4). Individual excitatory and inhibitory t-types generally follow this rule, but can also break it. For example, the excitatory marker *bhlhe23* is expressed in deep SPV neurons, where it is surrounded by inhibitory *insm2*, *chodl npb*, and *npy* neurons (Fig. 2, Extended data Fig. 4). The excitatory markers *ccka*, *onecut1*, *pitx2,* and *zic2*a are restricted to superficially located neurons in the SPV (Fig. 2, Extended data Fig. 4), whereas *irx1b*, *cart2*, and *nrgna* are expressed by neurons in the middle of the SPV (Fig. 2). Some t-types are present in all SPV regions, namely those expressing *atf5b*, *sp5l*, *gfra1a,* and *neurod1*, while the inhibitory markers *esrrb* and *rpp25b* show a two-layer expression pattern (Fig. 2). We rarely find neurons

expressing the same marker directly adjacent to each other (Fig. 2, Extended data Fig. 4-5), suggesting that neurons of the same type form a mosaic in the SPV, similar to individual RGC types in the retina.

To obtain a holistic picture of OT cell-type architecture, we manually labeled the neurons' centroid positions (Fig. 2c-d), and measured the nearest neighbor distances (NND) in 3D, between each centroid in a given t-type to its NN of all other t-types. We then performed hierarchical clustering on the mean NND vector for each t-type (Fig. 2e). The spatial organization of the clustered NND vectors divided the SPV into three distinct layers: superficial, intermediate and deep (Fig. 2e-f), illustrating locally neighboring t-types. This organization disappeared with shuffled labels (Extended data Fig. 6). Given that the superficial cells of the SPV are born before the deep cells, this finding suggests that, similar to the retina[37], cell classes and cell types develop in a prespecified order, with excitatory t-types generally preceding inhibitory t-types (Fig. 2; Extended data Fig. 4c).

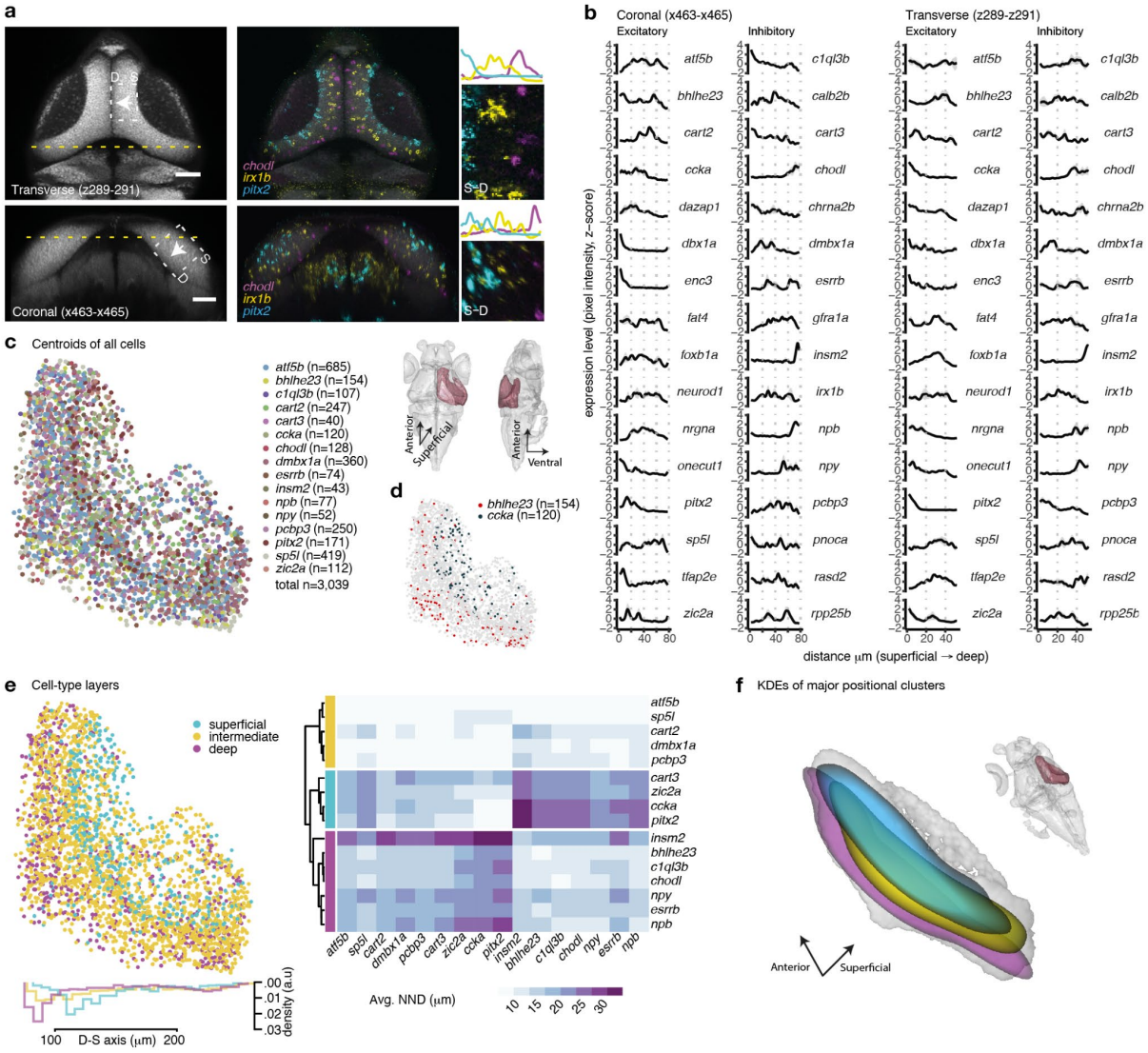

Fig. 2. Transcriptomic cell types form molecular layers orthogonally to the retinotopic map.

- **a.** Multiplexed RNA in-situ hybridization of selected marker genes were registered to the reference brain of the *mapzebrain.org* atlas. We measured the expression level by examining the pixel intensity profile of each gene in the same transverse (projection of planes z289-z291) and coronal section (projection of planes x463-x465). The pixel intensity measured area is labeled with a white dashed rectangle and confined to the SPV (S; superficial, D; deep).
- **b.** Z-scored pixel intensity of selected inhibitory and excitatory marker genes. Black line represents the average (n=3, simple moving average with window size=3), the gray shade represents standard error. Scale bar= 50 µm.
- **c.** Centroids of selected tectal cell type markers located within the SPV were manually labeled. Dorsal and lateral brain views with the right hemisphere tectal SPV highlighted in burgundy are shown, representing the labeled area of the centroids, as well as the tectal coordinate system.
- **d.** The labeled centroids of *bhlhe23* and *ccka* are shown, demonstrating the segregation of these cells along the tectum in 3D.
- **e.** The distance from each cell in a given cell type to its nearest neighbors of all other cell types was measured in 3D (NND). Hierarchical clustering of the average NND for each cell type revealed three main clusters, dividing the SPV layer into three molecular layers.
- **f.** 3D visualization of bounded Gaussian kernel densities for the three molecular layers from **e.**

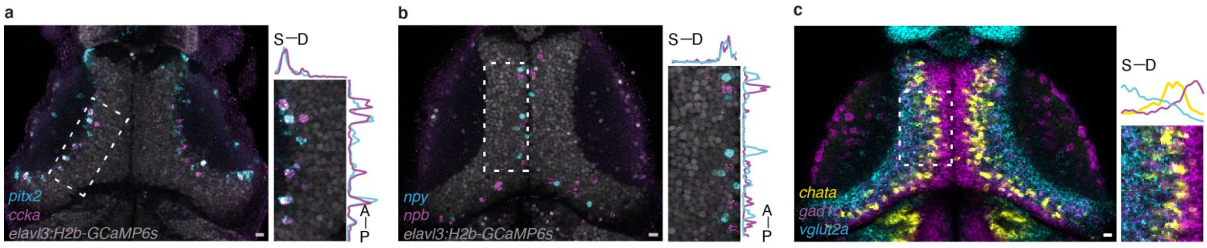

Extended data Fig. 4. Multiplexed HCR labeling of cell type markers. We applied HCR in-situ to analyze and validate the spatial arrangement of the cell types' marker genes.

- **a.** The marker gene *ccka* was co-expressed with *pitx2* in cluster e17 but not in cluster e14. Dashed square area is enlarged and the pixel intensity (z-scored) is plotted, demonstrating both the co-expression and the localization to the superficial part of the SPV. Scale bar= 10 µm.
- **b.** The expression of the neuropeptides *npb,* marker of cluster i29, and *npy,* marker of cluster i30 was mutually exclusive. In-situ HCR analysis demonstrated both the expression and the localization to the deep sublayer of the SPV. Scale bar= 10 µm.
- **c.** Registered in-situ data of *gad1b*, *vglut2a* (*slc17a6b*), and *chata* revealed that glutamatergic, cholinergic, and GABAergic neurons are segregated along the tectal superficial to deep axis. Scale bar= 10 µm.

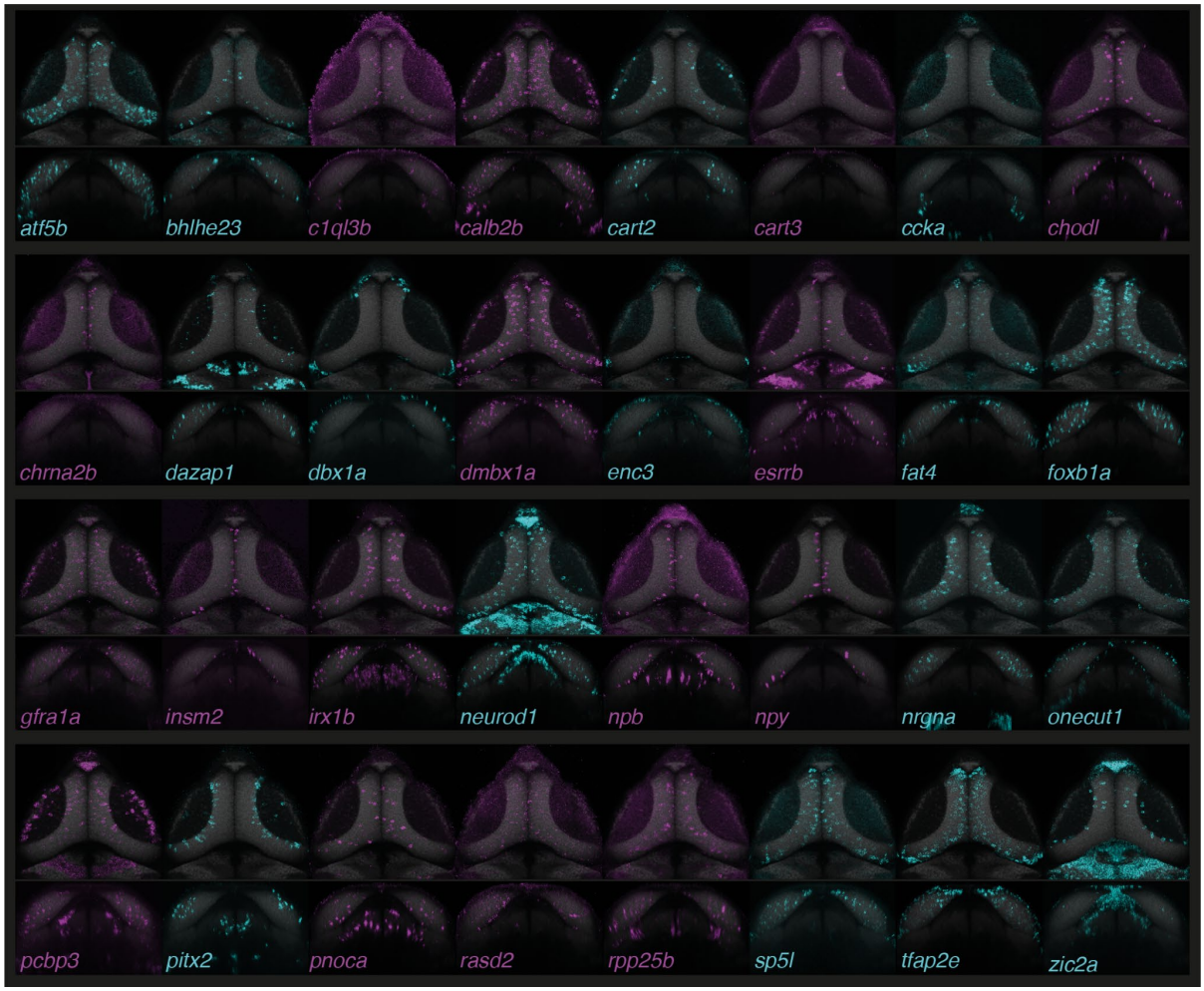

Extended data Fig. 5. Marker genes expression patterns. Registered HCR in-situ data for the examined cell type markers. Projection of transverse planes z289-z291 and coronal planes x463-x465 of single animals. Excitatory markers are shown in cyan, inhibitory markers are shown in magenta. All the data can be viewed through mapzebrain.org[36].

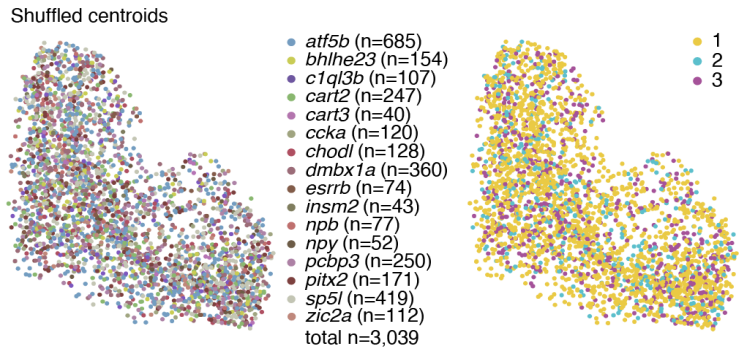

Extended data Fig. 6. Shuffling of the tectum cell type centroids results in a loss of the observed molecular layers within the tectum.

Individual tectal t-types are selectively tuned to multiple visual stimuli

We next asked if neurons of a given transcriptomic type shared selectivity to visual stimuli in their functional responses. To this end, we recorded calcium activity by 2-photon volumetric imaging in tectal neurons of *elavl3:H2B-GCaMP6s* transgenic larvae, exposed to a battery of ethologically relevant visual stimuli. The stimuli included both local and global motion cues: dots moving in different directions, either continuously or in a saltatory fashion (bout-like or continuous motion[38]), a forward moving grating (evoking optomotor responses), a looming black disk (simulating a predator or an object on a collision course) and ambient luminance changes (Fig. 3a). We then fixed the imaged animal and performed iterative multiplexed HCR, labeling up to six t-type markers per sample. Markers were chosen for their mutually exclusive expression in single t-types (except for *pitx2* and *ccka*; Extended data Fig. 7). The 2-photon live 3D volume was then aligned to the in-situ 3D HCR-labeled volume. In 1,204 neurons from 6 animals, we could unambiguously assign a t-type to a functionally recorded neuron (Fig. 3b).

Perhaps surprisingly, we found that average t-type responses had elevated scores for at least two stimuli of the set (Fig. 3c). For example, moving dots as well as moving gratings evoked strong activity in the *sp5l* type, while *itpr1b* neurons scored highest for looming and OFF ramp (Fig. 3c). To test whether individual neurons within the same t-type or between t-types have similar functional responses we correlated calcium traces of all t-type+ neurons with each other across animals (Fig. 3d). A correlation matrix of raw calcium traces, sorted by t-type, and within t-type by overall response score to local motion stimuli, i.e., moving dots, revealed stereotyped clusters of positive and negative pairwise correlations within and between all t-types (Fig. 3d). This indicates a functional diversity within each t-type, varying mostly in the relative frequency of local- and global-motion tuned neurons. Mean pairwise correlations of calcium responses were significantly higher within t-type than between t-types for six out of nine marker genes tested (Fig. 3e). We conclude that neurons of the same t-type show diverse but partially coherent visual tuning that is distinctive from other t-types.

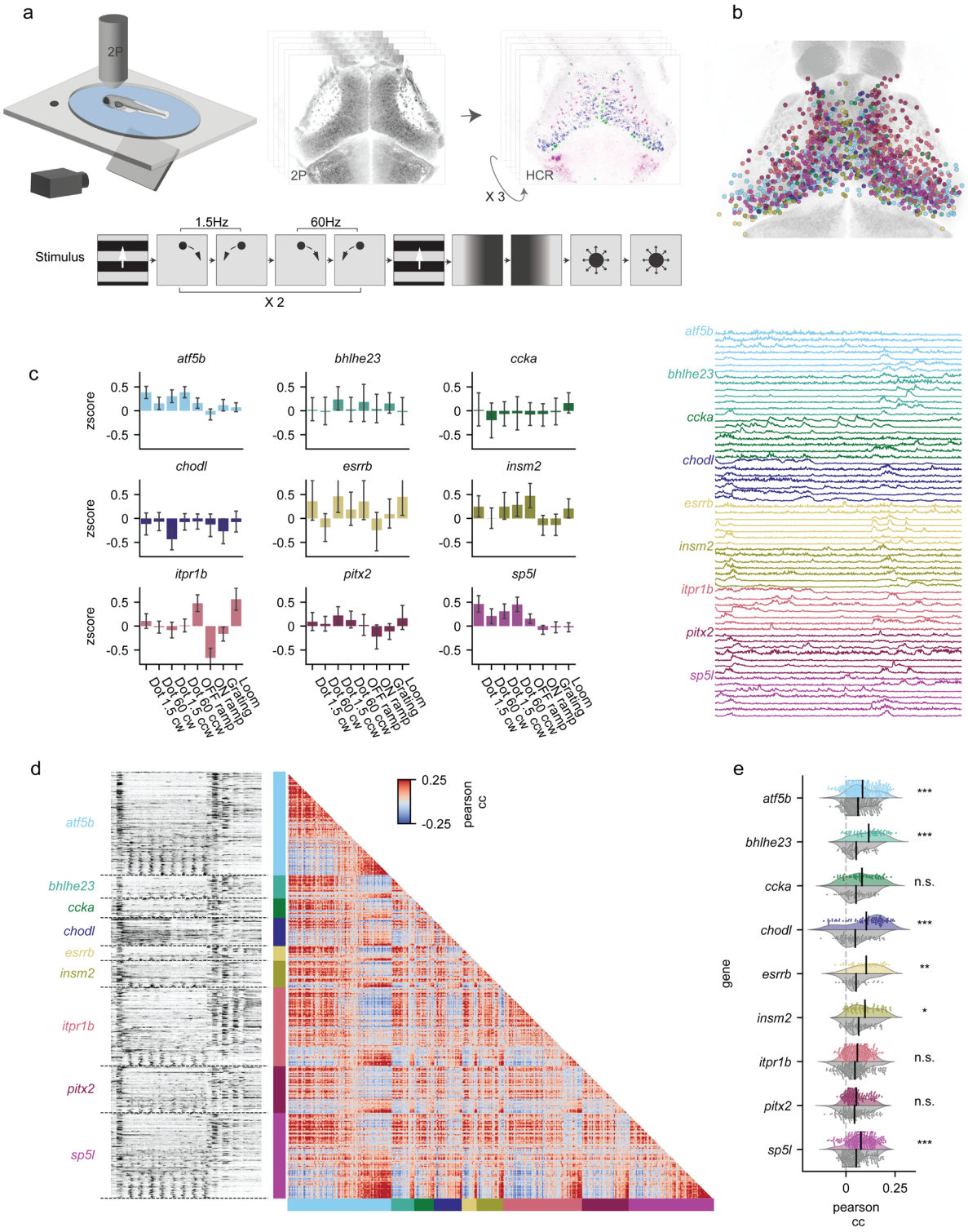

Fig. 3. t-types show diverse visual responses and form coherent functional subclusters

a. Experimental procedure: 6 dpf larvae were exposed to a battery of visual stimuli while volumetric functional 2-photon calcium imaging was performed in most neurons of the tectum. The larvae were then stained in consecutive rounds for up to 6 marker gene mRNAs using HCR labeling.

b. Result of aligning functional and HCR brain volumes and registering all ROIs that overlap with one of 9 marker genes into a common anatomical reference frame (ROIs=1204, N=6).

c. Average t-type response scores to the visual stimulus battery scaled to unit variance and zero mean of overall tectal population. Most t-types showed elevated or decreased responses to at least two different stimuli.

d. Top: Pictogram of temporal sequence of visual stimuli. Left: Raw calcium traces of all 1204 t-type+ functional ROIs sorted by first t-type and within t-type by response score to local motion. Responses to global motion (beginning, end) as well as local motion (middle section) are visible in all t-types. Right: Correlation matrix of all pairwise correlations using pearson correlation coefficient. Red and blue clusters of positively and negatively correlated neurons are found between and within all t-types.

e. Mean pairwise correlations of each neuron with all neurons of the same t-type (color) and all neurons (gray) of other t-types. Within t-type correlation is significantly increased for six out of nine tested t-types. Two-sided Mann-Whitney-U Test, Bonferroni-corrected. *$p < 0.05$, **$p < 0.01$, ***$p < 0.001$.

Position in the tectum contributes to the functional differentiation of genetically identified neurons

While functional responses varied within neurons of the same t-type, discrete functional phenotypes might still be specific to certain t-types. To explore these possibilities, we first identified functional neuronal phenotype classes in the tectum. For this, we clustered the 8-dimensional stimulus response vectors of the most responsive tectal neurons for any given stimulus regardless of transcriptomic identity (n=7,127), yielding 15 distinct f-types (Fig. 4a). The response vectors of most responsive neurons formed five superclusters in a two-dimensional t-SNE embedding, corresponding to broad classes of neurons tuned to local motion, ON, OFF, looming, and grating motion, respectively (Fig. 4b-c). The 15 functional clusters were locally enriched in regions of the OT (Extended data Fig. 8), consistent with regionally specialized information processing in the tectum[4].

Next, we mapped t-types into the functional space to search for t-type specific subclusters. To this end, we computed for each of the most responsive tectal neurons the ratio of how common all t-types are in the 50 nearest neighbors to the expected proportion (if t-type distribution was independent) (Fig. 4d). Visualizing this metric in the functional embedding revealed that specific t-types are locally enriched within f-type superclusters in functional space. A similar result was obtained when mapping response vectors from neurons in transgenic lines expressing GCaMP6s under the control of the *atf5b*, *itpr1b,* or *sp5l* regulatory regions (see Methods; Fig. 4e; Extended data Fig. 9).

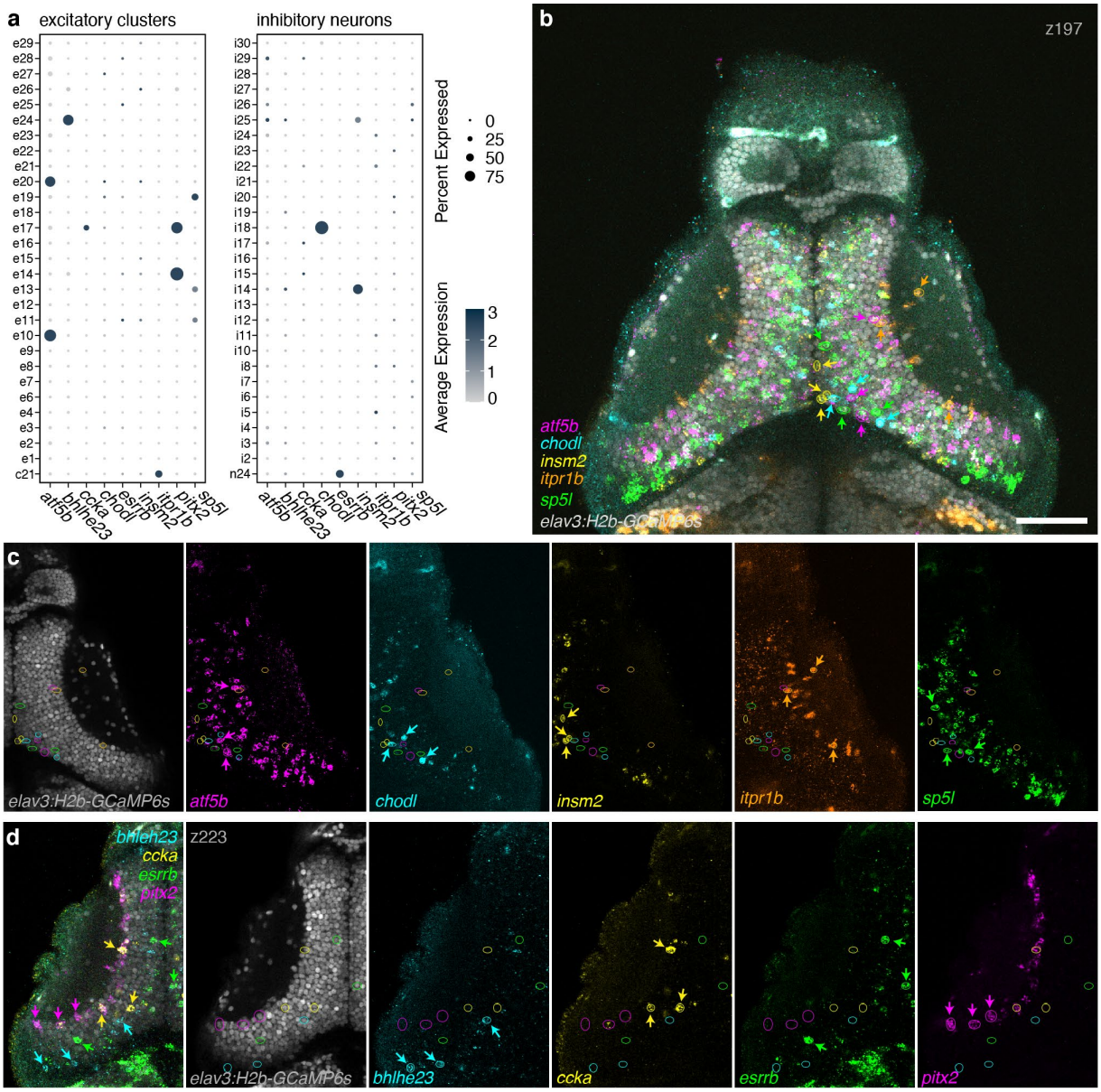

Extended data Fig. 7. HCR labeling of marker genes post calcium imaging.

- **a.** HCR was performed on a set of nine marker genes. The expression levels of these genes measured by scRNA-Seq showing their expression is restricted to one or a few non-overlapping clusters, except for *ccka* that overlaps with *pitx2* expression.
- **b.** Multiplexed interactive HCR labeling post functional imaging. Five genes were labeled and registered. Similar to the scSeq data, these genes were not co-expressed in the same cells, representing different tectal t-type populations. Circles and arrowheads point to example cells shown in **C**, color coded similar to the gene HCR color. Single z-plane is shown, scale bar = 50 µm.
- **c.** Same view as **b**, split according to the genes labeled.
- **d.** Example of another multiplexed interactive HCR post functional imaging, with a different set of labeled cell type marker genes.

We next directly assigned one of the 15 f-types to each of the 1204 t-type+ neurons. We found that no f-type was exclusive to a single t-type (Extended data Fig. 8). Based on the layered structure of t-types we wondered whether neurons of the same f-type would be anatomically localized within t-types. For this, we determined the anatomical distributions of such t/f-clusters that shared functional and transcriptomic identity. This analysis yielded a sufficiently large sample, consisting of at least 10 neurons per t/f-cluster for four of our t-type markers. For each t/f-cluster, we computed a gaussian kernel density estimate (KDE) and measured the pairwise spatial overlap of t/f-cluster KDEs within t-types and f-types, respectively. We discovered that t/f-clusters show significant anatomical separation compared to shuffled controls (Fig. 4f). This indicates that cell body position within a tectal t-type strongly influences its functional phenotype. Interestingly, neurons of different t-types but the same f-types also show significantly lower spatial overlap compared to shuffle controls, suggesting that neurons of the transcriptomic identity and functional phenotype are anatomically clustered for both modalities in the tectum.

Support vector machine (SVM) classification revealed that cell-body position in the OT volume is a better statistical predictor for t-type than position in functional space for tectal neurons. Combining both spaces yields even higher predictive power (Fig. 4h-i). Taken together, these results indicate a strong contribution of anatomical position to the functional phenotype of neurons with a given transcriptomic type.

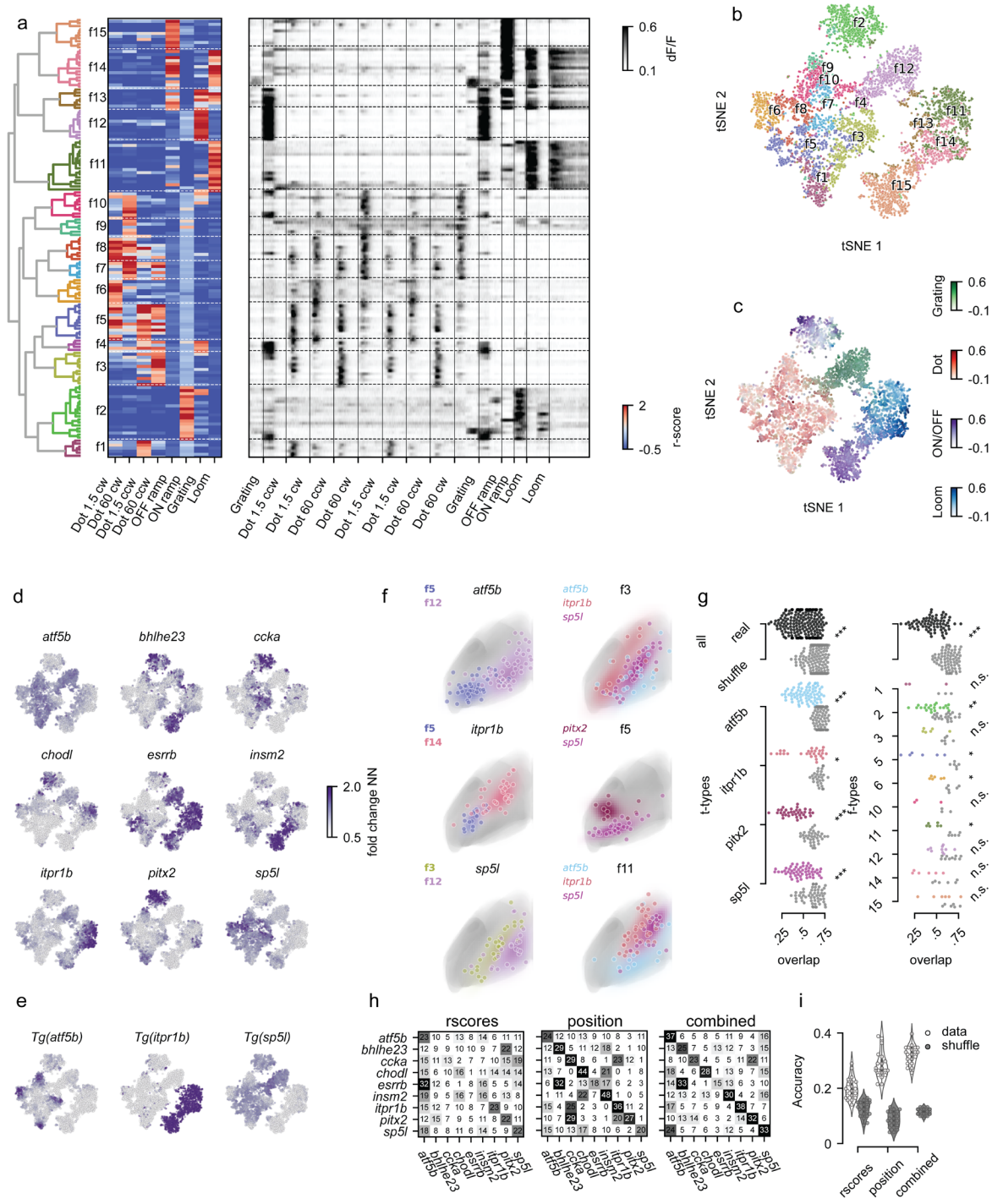

Fig. 4. Localization in functional and anatomical space varies between t-types.

a. Hierarchical clustering of all strongly responding tectal neurons (N=7127) to identify functional cell types (f-types). Left: Dendrogram of clustering all 145 exemplars that were identified using affinity propagation. Middle: Heatmap showing response vectors of all exemplars based on stimulus battery. Functional clusters and exemplars are primarily divided into local (clusters 1-10) vs. global (clusters 11-15) motion responses. Right: Raw calcium traces of all exemplars.

b. t-SNE visualization based on response vectors, overlaid with color code according to the f-type assignment.

c. t-SNE visualization of all responding neurons from **b**, with four different color codes for response score to different stimuli.

d. T-types accumulate locally in functional space. Left: Fold-changes in t-type+ nearest neighbor frequencies for each strongly responding neuron in 8-dimensional functional space mapped onto t-SNE visualization. k=50 NN.

e. Response vectors of the transgenic t/f-ROIs, mapped into the same functional embedding, largely confirmed the enrichments observed **d**.

f. Anatomical localization of t/f-clusters within t-types and f-types. Dots represent individual ROIs, colored areas show gaussian kernel density estimates (KDEs) of t/f-clusters. ROIs of the same t-type (left) / f-type (right) comprise anatomically separated clusters based on functional (left) / transcriptomic (right) identity. All ROIs mirrored to the left tectal hemisphere.

g. t/f-clusters are significantly separated in anatomical tectal space within t-types and f-types. Left: Pairwise KDE overlap values for cell types of different functional clusters for real data and shuffled t-type labels. Right: Same as left for different t-types within functional clusters. Mean pairwise overlap values of t/f-clusters across t-types and across f-types are significantly lower than respective shuffled controls, respectively, indicating anatomical separation of cell types within functional clusters. Two-sided Mann-Whitney-U Test, Bonferroni-corrected. *$p < 0.05$, **$p < 0.01$, ***$p < 0.001$.

h. Confusion matrices of three SVM classifiers predicting transcriptomic identity based on functional response vectors, cell body position, or both. Numbers and saturation indicate a true-positive rate. Predictive performance increases from left to right, indicated by the saturation of the diagonal (true positive predictions per cell type).

i. Accuracy of SVM classifier performances from **h** (grey dots and violin plots). Position in functional space can recover t-type identity in roughly one out of five cases, for anatomical space accuracy was 10% higher. Combining both spaces resulted in elevated performance. For all classifiers, negative controls with shuffled cell type labels resulted in significantly lower performance (white dots and violin plots).

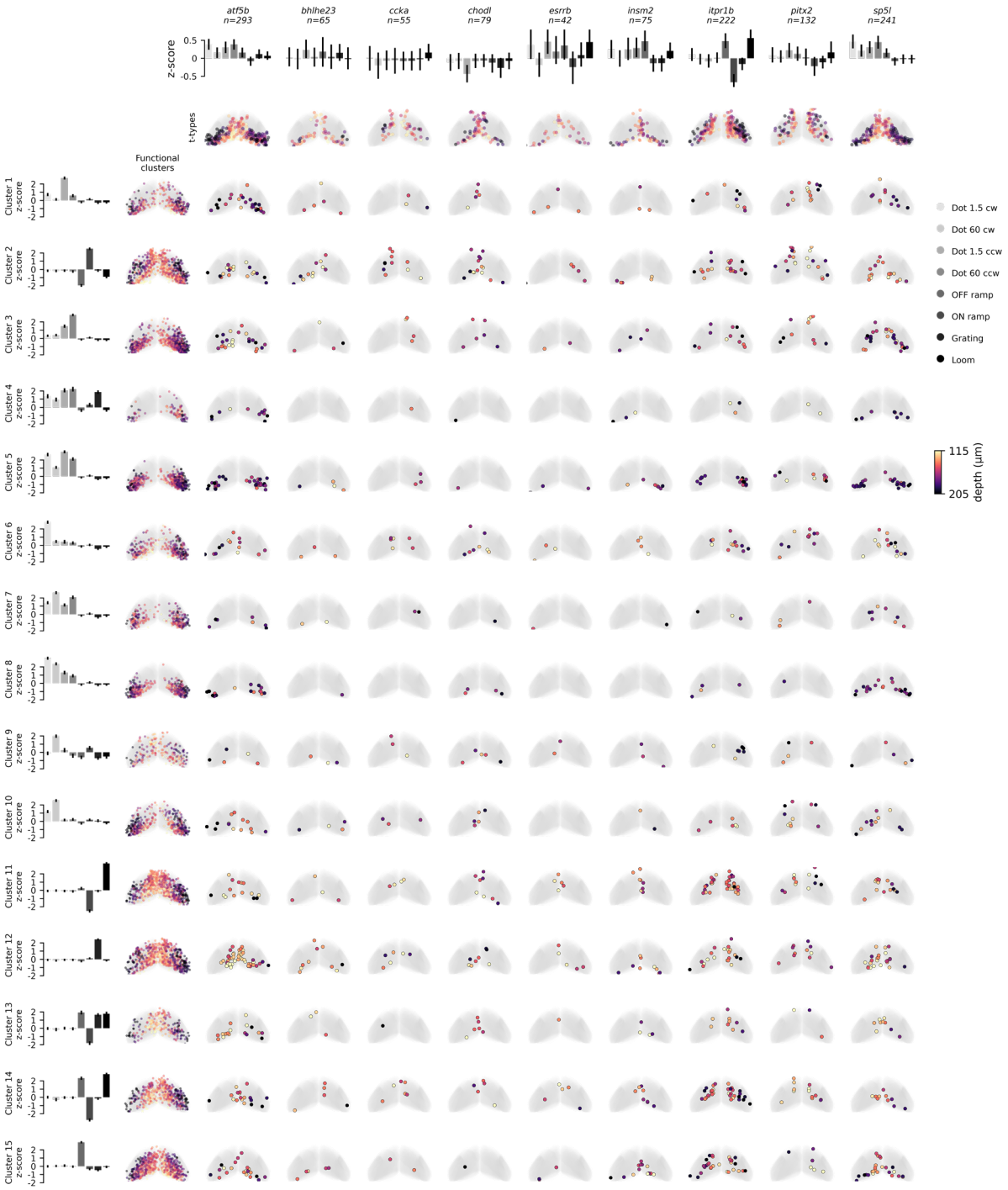

Extended data Fig. 8. T-types comprise anatomically coherent functional clusters

First column: average response scores of each f-type scaled to tectal population mean. Second column: Anatomical localization of f-types in the tectum. First row: average response scores of each t-type scaled to tectal population mean. Second row: Anatomical localization of functionally recorded t-types. Inner matrix: Anatomical localization of t-type ROIs assigned to respective f-types. Color code depicts tissue depth.

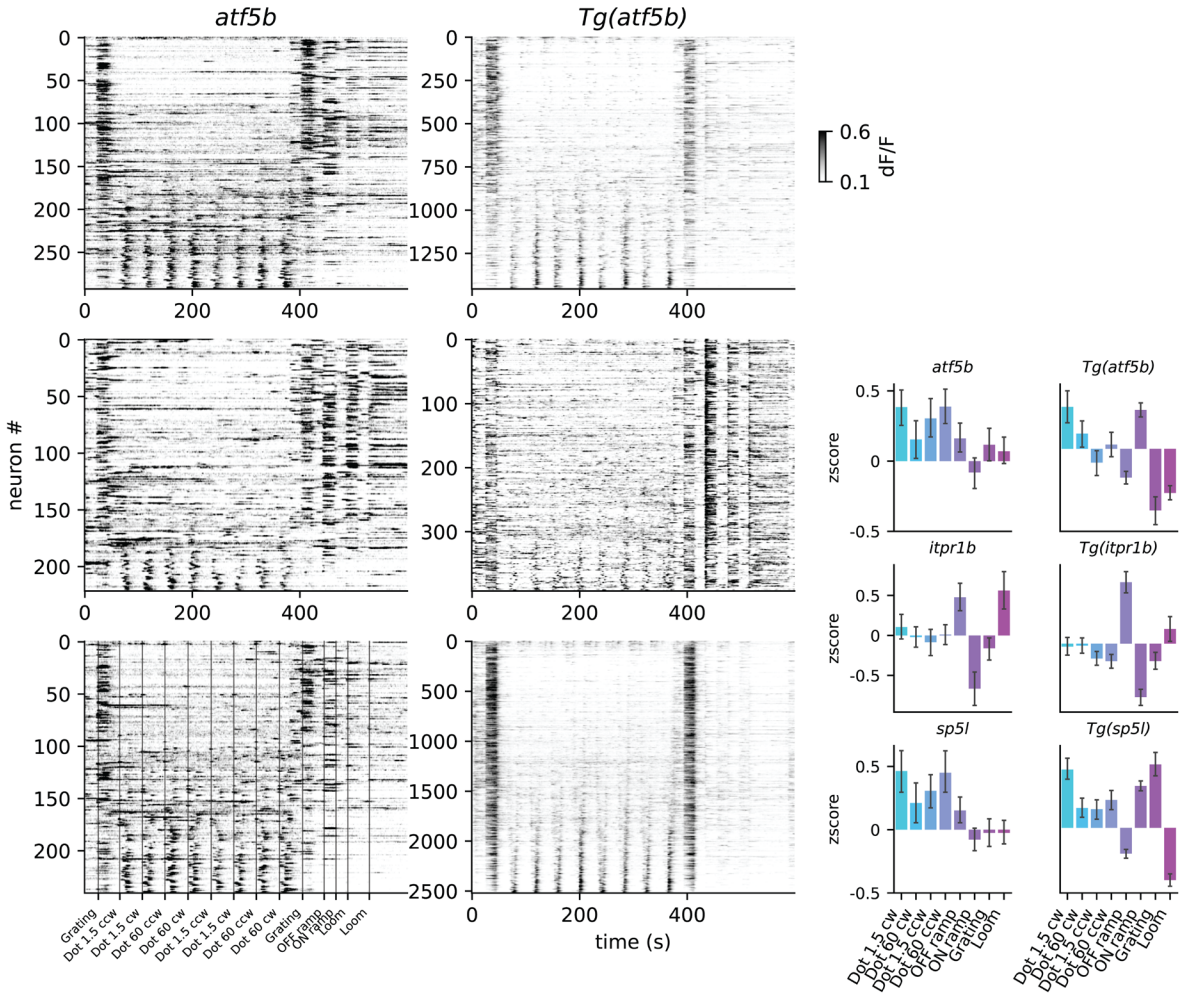

Extended data Fig. 9. Comparison of functional responses between HCR labeled t-types and the corresponding transgenic lines.

- **a.** Raw traces of all t-type+ ROIs for *atf5b*, *itpr1b,* and *sp5l* from HCR-labeling, or transgenic lines (Tg) expressing GCaMP6s exclusively in *atf5b*+, *itpr1b,* or *sp5l*+ neurons. Traces are sorted according to an overall local motion response score. Proportions of ROIs responding to local motion vs. grating/looming stimuli are similar between conditions.
- **b.** Left: Average response scores of three marker genes *atf5b*, *itpr1b,* and *sp5l* from Figure 5E. Right: Average response scores of recorded ROIs from three transgenic lines for the same marker genes, scaled to tectal population response. Average responses were similar between experiments for *itpr1b* while *atf5b*+ neurons showed broader tuning in the HCR experiments and *s5l*+ neurons were tuned more broadly in transgenic fish.

Transcriptome and position influence tectal neuron morphology

Tectal neurons exhibit a rich diversity of morphologies, including specific dendritic and axonal targets[4,5,39–42]. We asked whether t-type is related to m-type, making use of transgenic reporter lines labeling the *atf5b*, *itpr1b, pcbp3,* and *sp5l* t-types. We sparsely labeled single neurons in these

transgenic lines and traced their morphologies (see Methods). The excitatory *atf5b* and *sp5l* neurons included specific sets of ipsilaterally or contralaterally projecting neurons and interneurons with a range of dendritic stratification patterns (Fig. 5a, d; Extended data Fig. 10a-e). The *pcbp3* neurons are inhibitory interneurons with monostratified neurite arbors and with cell bodies located in the superficial half of the neuropil or the SPV (Fig. 5c; Extended data Fig. 10d). The *itpr1b* neurons are a relatively homogeneous population, which resides exclusively in the neuropil (Fig. 5b), with morphologies reminiscent of tectal pyramidal/type I neurons[39,42].

We asked if we could further differentiate *atf5b* and *sp5l* projection neurons with comparable projection patterns (Figure 5e-f). By registering confocal images of these two transgenic lines, we discovered that the fluorescent intensity of their ipsilateral projections differed: *sp5l* neurons have collaterals within the GABAergic domain of a tegmental nucleus, the nucleus isthmi[43], while *atf5b* neurons form collaterals in its glutamatergic domain (Figure 5f). As is the case for t/f-clusters, the morphology of neurons belonging to the same t-type varies across the OT: *sp5l* cells tend to develop into interneurons in the anterior OT and into projection neurons in the posterior OT (Fig. 5d), while the reverse appears to hold for *atf5b* cells. Together, this suggests that individual t-types accommodate a distinct range of morphologies, which are expressed in a position-dependent manner across the AP axis of the OT.

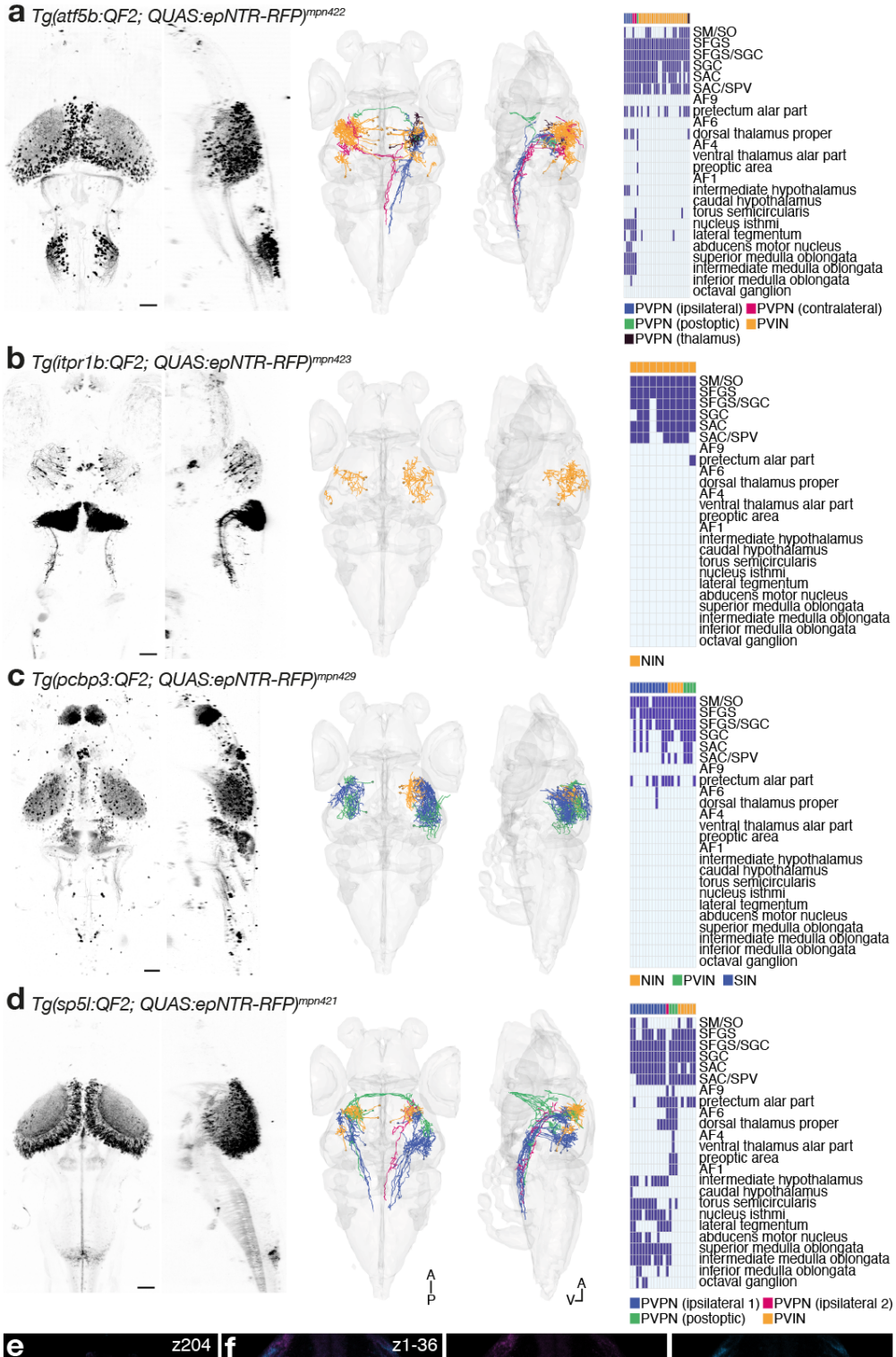
a Tg(atf5b:QF2; QUAS:epNTR-RFP)mpn422
SM/SO
SFGS
SFGS/SGC
SGC
SAC
SAC/SPV
AF9
pretectum alar part
AF6
dorsal thalamus proper
AF4
ventral thalamus alar part
preoptic area
AF1
intermediate hypothalamus
caudal hypothalamus
torus semicircularis
nucleus isthmi
lateral tegmentum
abducens motor nucleus
superior medulla oblongata
intermediate medulla oblongata
inferior medulla oblongata
octaval ganglion
PVPN (ipsilateral)
PVPN (contralateral)
PVPN (postoptic)
PVIN
PVPN (thalamus)
b Tg(itpr1b:QF2; QUAS:epNTR-RFP)mpn423
NIN
c Tg(pcbp3:QF2; QUAS:epNTR-RFP)mpn429
NIN
PVIN
SIN
d Tg(sp5l:QF2; QUAS:epNTR-RFP)mpn421
PVPN (ipsilateral 1)
PVPN (ipsilateral 2)
PVPN (postoptic)
PVIN
A
P
A
V
e
z204
atf5b
sp5l
f
z1-36
NI GABAergic domain
NI Glutamatergic domain
intermediate ventral medulla oblongata
atf5b
sp5l

Fig. 5. Combination of morphological types within tectal t-types.

- **a.** Left- z-projection of *Tg(atf5b:QF2; QUAS:epNTR-RFP)* larva. Center - sparsely labeled *atf5b+* neurons were registered into a reference brain (N=31). Neurons are color coded according to their m-type. Right- anatomical matrix.
- **b.** Left- z-projection of *Tg(itpr1b:QF2; QUAS:epNTR-RFP)* larva. Center - sparsely labeled *itpr1b+* neurons were registered into a reference brain (N=10). Neurons are color coded according to their m-type. Right- anatomical matrix.
- **c.** Left- z-projection of *Tg(pcbp3:QF2; QUAS:epNTR-RFP)* larva. Center - sparsely labeled *sp5l+* neurons were registered into a reference brain (N=21). Neurons are color coded according to their m-type. Right- anatomical matrix.
- **d.** Left- z-projection of *Tg(sp5l:QF2; QUAS:epNTR-RFP)* larva. Center - sparsely labeled *sp5l+* neurons were registered into a reference brain (N=22). Neurons are color coded according to their m-type. Right- anatomical matrix.
- **e.** Registered confocal stack of *atf5b* and *sp5l* transgenic fish. A single focal plane spanning the optic tectum is shown. Scale bar = 50 μm.
- **f.** Z-projection of the nucleus isthmi area, showing *atf5b* and sp5l projections forming collaterals at different parts of the nucleus isthmi.

Abbreviations: A; anterior, NIN; neuropil interneurons, P; posterior, PVPN; periventricular projection neurons, PVIN; periventricular interneurons neurons, SIN; superficial interneuron, V; ventral

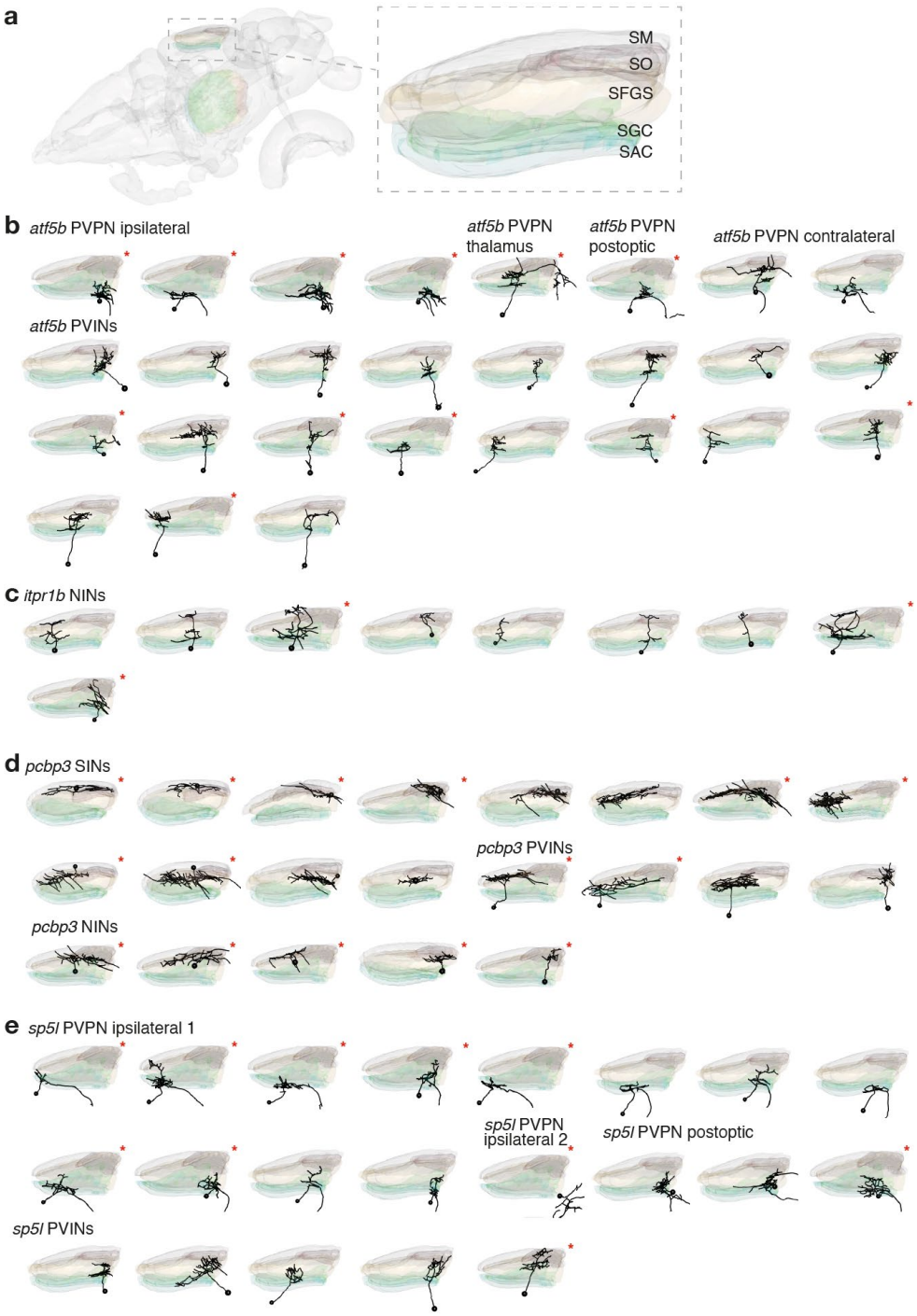

Extended data Fig. 10. Stratification within the tectal neuropil of the traced neurons

- **a.** Illustration of the larval zebrafish brain, highlighting the tectal neuropil layers. Abbreviations: SAC; stratum album centrale, SFGS; stratum griseum et fibrosum superficiale, SGC; stratum griseum centrale, SM; stratum marginale, SO; stratum opticum.
- **b. - e.** Stratification of m-types within the tectal neuropil. * Neurons mirrored from right to left hemisphere

Discussion

A neuron's shape, synaptic connectivity, and function, i.e., its phenotype, are dictated, or at least bounded, by the genes it expresses. High-throughput barcoding and sequencing efforts promise to offer deep insights into brain function, provided that transcriptomic datasets can be read out at scale and eventually translated into wiring diagrams[44]. This formidable task is aided by the observation that single-cell transcriptomes can be clustered by similarity of their gene expression profiles, with clusters corresponding to individual cell types. Such dimensionality reduction allows researchers to focus on characterizing the connectional and functional properties of reproducible sets of neurons, 'cell type by cell type' and across animals. Single-cell RNA sequencing and spatial transcriptomics have successfully matched cell types to specific brain regions[45,46], to developmental trajectories[47–49] and to specific functions[2,3,6,50], although the latter with less stringency and consistency[14,15,51].

There are at least two factors that confound this straightforward cell-type concept: topography and development. First, it is unclear if and how transcriptionally defined cell types vary in brain areas that are regionally specialized, such as topographic maps, which are prevalent in the visual, auditory, and somatosensory systems. Are different cell types employed for each local circuit? Or are the same cell types repurposed for local processing demands, with the consequence that their connectivity, morphology, and function vary across the map? Second, neurons are not manufactured in one sweep like transistors are printed on a microchip; they grow in number by cell division and wire up by extending neurites often over long distances and searching for molecularly matching synaptic partners. Thus, neurons respond to dynamically changing local cues depending on when and where in the tissue they are born, differentiate and form connections.

Studying the zebrafish tectum, we find that both development and topography contribute to the expression of functional and morphological traits of genetically identified neurons. Positional information influences cell-type function along all three axes of the tectal volume. For the retinotopic axes of the tectum, regional differences in f-type distribution probably reflect either input heterogeneities[18,52,53] or asymmetric circuit layout across the spatial array of neurons[54]. Visual processing is adapted to stimulus statistics, and these are not uniform across the visual field. The principle is well illustrated by the example of prey capture, a prominent tectum-dependent behavior [4]. For a hunting zebrafish larva, protozoan prey is most likely to appear in the distance and in the peripheral visual field; accordingly, RGCs residing in the nasal retina and (their topographically matched) posterior tectal neurons respond preferentially to small, motile objects[4]. Anterior-dorsal tectal cells and their RGC inputs from the temporal-ventral retina, on the other hand, respond to larger-sized objects, which match a prey object that is positioned right in front of the fish, shortly before the capture strike[55]. Similarly, different tectal domains are specialized for driving task-specific motor commands including approach of prey and escape from a predator[5].

For the superficial-to-deep axis of the tectum, transcriptomic identity correlates strongly with time of birth: early-born neurons come to reside closer to the surface of the SPV, as they are displaced by later-born neurons, which stay near the deep ventricular zone[19,20]. A similar temporally staggered development of cell types has been reported in other systems[37,56]. However, neurons that share their transcriptomes do not necessarily have the same functional profile, and vice versa. An influence of positional information on the expression of cell-type traits supports the notion that a limited number of global transcriptomic states (cell types) are re-used and locally adapted to generate functioning circuits[57]. While the repertoire of genetically distinguishable neuronal cell types is already enormous[6,10,11,58], local extrinsic cues can generate even more variants of genetically programmed circuitry.

Methods

Zebrafish husbandry and maintenance

Adult zebrafish were kept at 28°C under a day/night cycle of 14/10 hours, pH of 7-7.5, and a conductivity of 600 µS. The following transgenic lines were used in this study: Wild type (WT) fish of the TL stain, *Tg(elavl3:H2b-GCaMP6s), Tg(atf5b:QF2)mpn422, Tg(itpr1b:QF2)mpn423, Tg(pcbp3:QF2)mpn429, Tg(sp5l:QF2)mpn421, Tg(QUAS:GCaMP6s)mpn164.* All larvae produced by natural matings and raised until 6 days post fertilization (dpf) at 28°C in Danieau´s solution in petri dishes. The animal experiments were performed under the regulations of the Max Planck Society and the regional government of Upper Bavaria (Regierung von Oberbayern), approved protocols: ROB-55.2-2532.Vet_03-19-86, ROB-55.2-2532.Vet_02-19-16, ROB-55.2-2532.Vet_02-21-93.

Single-cell RNA sequencing

Tissue dissections and cell dissociation

6-7 dpf WT larvae were anesthetized in tricaine (one larvae at a time), followed by removal of the eye and the skin around the brain using a fine Tungsten needle. The OT and TL were carefully dissected out of the brains and transferred into a low-binding protein eppendorf tube containing ~50µL of PBS, which was placed on ice. Cell dissociation procedure was performed immediately after the dissections (see below). Eight batches of dissections were performed on different days, 20-25 OTs and TLs were dissected in each batch.

Cell dissociation

Cell dissociation was performed using Papain (Papain dissociation system, Worthington Biochemical Corporation). A 500µl of oxygenated papain was added to the eppendorf tube containing the 50µl PBS and the dissected tissue, and incubated at 37°C with superficial oxygen flow. The samples were gently pipetted every 10 minutes, and were fully dissociated after 45 minutes (a 2µl sample was visually inspected to assess cell separation). The cells were then centrifuged for 10 minutes at 400g, at 4°C, using a swinging bucket centrifuge. The supernatants were carefully removed, and the cells were resuspended in 260µl of equilibrated ovomucoid solution and 30µl of DNaseI. The cells were then centrifuged for 10 minutes at 400g, at 4°C, the supernatants were removed, and the cells were resuspended in 500µl PBS and 0.04% BSA. This step was repeated once again, after which the cells were filtered using 30µm cell strainer. Lastly, the cells were centrifuged, and the supernatants were removed, leaving 80µl in which the cells were pipette gently. 5µl of the dissociated cells were

transferred into a new low-binding protein eppendorf tube and mixed with 13µl PBS, 0.04% BSA and 0.4% Trypan blue for cell counting and viability assessment.

Library preparation and sequencing

The dissociated cells were loaded onto a commercially available droplet-based single-cell barcoding system (10x Chromium Controller, 10x Genomics). The Chromium Single Cell 3′ Reagent Kit v3 (10x Genomics) was used to prepare single-cell 3′ barcoded cDNA and Illumina-ready sequencing libraries according to the manufacturer's instructions. The cDNA libraries were sequenced using an Illumina HiSeq 2500 machine, with a mean of ~90,000 reads per cell over the 8 batches. The raw sequencing data will be made available upon publication through NCBI's Gene Expression Omnibus (GEO).

Quality check, batch correction and clustering analysis

The sequenced data was processed using CellRanger (filtering, barcode and UMI counting) with default command line options. The sequenced reads were aligned to the zebrafish GRCz11 genome assembly (Ensembl release 101). To prevent confounding effects of the tissue dissection and cell dissociation on gene expression analysis, immediate early genes (IEGs) that were induced during the procedure[59], were removed prior to the analysis. We have curated a list of 43 zebrafish IEGs (Extended data table 2), and excluded them from the cell-gene matrix. The data from the 8 batches was then merged into a single Seurat object and analyzed using the Seurat R package version 4[60]. Additional filtration steps were performed to ensure analysis of high quality cells, including filtering out cells expressing less than 200 or higher than 4000 genes, cells with higher than 4000 unique molecular identifiers (UMIs), or containing higher than 20% mitochondrial genes. This resulted in a final dataset of 20,197 cells with a median of 660 genes per cell and 1495 UMIs. The data was then normalized using the Seurat "LogNormalize" methods with a scale factor of 10,000. A set of 2,000 variable features were identified using the "vst" selection method, and the data was scaled using the "ScaleData" command with default parameters. The detected variable features were used for principle component analysis. We then performed batch correction using "Harmony"[24], grouping the variables according to their original batch followed by dimensionality reduction with Uniform Manifold Approximation and Projection (UMAP). Clustering analysis was performed by applying the Seurat "FindNeigbors" command with reduction="harmony" and dims=30, and the "FindCluster" command with resolution set to 1.2 (sub-lcustering resolution was: neurons=1.7, excitatory neurons= 2.5, inhibitory neurons=4). Differentially expressed genes were identified using the Wilcoxon Rank Sum test integrated in the Seurat "FindAllMarkers" command. Pseudotime analysis was performed using Monocle3[61].

Multiplexed and iterative *in situ* hybridization chain reaction (HCR)

All the HCR experiments were performed on *Tg(elavl3:H2b-GCaMP6s)* larvae to enable registration onto the *mapzebrain.org* atlas and a common coordinate system between images. All the HCR reagents including probes, hairpins and buffers were purchased from Molecular Instruments (Los Angeles, California, USA). The staining was performed according to previously published and modified protocol[22,36]. *Tg(elavl3:H2b-GCaMP6s)* positive larvae were anesthetized in 1.5 mM tricaine and fixed with ice-cold 4% PFA/DPBS overnight at 4°C with gentle shaking. The following day, larvae were washed 3 times for 5 minutes with DPBST (1x Dulbecco's PBS + 0.1% Tween-20) to stop fixation, followed by a short 10-minute treatment with ice-cold 100% Methanol at −20°C to dehydrate and permeabilize the tissue samples. Next, rehydration was performed by serial washing of 50% MeOH/50% DPBST and 25% MeOH/75% DPBST for 5 minutes each and finally 5 × 5 minutes in DPBST. 10-12 larvae were transferred into a 1.5 ml Eppendorf tube and pre-hybridized with pre-warmed hybridization buffer for 30 minutes at 37°C. Probe solution was prepared by transferring 2 pmol of each HCR probe set (2 µl of 1 µM stock) to 500 µl of hybridization buffer at 37°C. The hybridization buffer was replaced with probe solution, and the samples were incubated for 12-16 hours at 37°C with gentle shaking. To remove excess probes, larvae were washed 4 × 15 minutes with 500 µl of pre-warmed probe wash buffer at 37°C. Subsequently, larvae were washed 2 × 5 minutes with 5x SSCT (5x sodium chloride sodium citrate + 0.1% Tween-20) buffer at room temperature. Next, pre-amplification was performed by incubating the samples in 500µl of amplification buffer for 30 minutes at room temperature. Separately, 30 pmol of hairpin h1 and 30 pmol of hairpin h2 were prepared by snap-cooling 10 µl of 3 µM stock by incubating the hairpins in 95°C for 90 seconds, and cooling down to room temperature in a dark environment. After cooling down for 30 minutes, hairpin solution was prepared by transferring the h1 and h2 hairpins to a 500 µl amplification buffer. The pre-amplification buffer was removed and the samples were incubated in the hairpin solution for 12-16 hours in the dark at room temperature. Excess hairpins were washed the next day 3 × 20 minutes using 5x SSCT at room temperature. Larvae were then long-term stored at 4°C in 5X SSCT until imaging.

For iterative HCR staining, the HCR probes and hairpins were stripped using DNAseI treatment. The imaged fish were placed separately in eppendorf tubes and incubated in a mix of 5µl 10x reaction buffer (Invitrogen #AM2238), 5µl Turbo DNAseI (final concentration 0.2U/µl, Invitrogen #AM2238) and 40µl DPBS for 4 hours at 37°C. The samples were then washed 3 × 5 minutes with DPBST and the complete removal of the HCR signal was validated under a confocal microscope. The HCR striped fish were kept separated in eppendorf tubes and underwent another round of HCR staining and imaing, beginning from the pre-hybridization step.

HCR data was registered onto the HCR reference brain as previously described[36] using Advanced Normalization Tools (ANTs)[62]. For the functional HCR experiments (see below), where iterative HCR

stainings were performed, each iteration was registered to the first iteration of the same animal. A total of 3 HCR rounds were performed on single animals without any noticeable morphological distortions or reduction of the endogenous fluorescence of the *Tg(elavl3:H2b-GCaMP6s)* used as the reference registration channel.

HCR image registration

All the HCR images were aligned onto the *Tg(elavl3:H2b-GCaMP6s)* average brain[35,36].

The ANTs registration command used was:

antsRegistration -d 3 --float 1 -o [${output1},${output2}] -- interpolation WelchWindowedSinc --use-histogram-matching 0 -r [${template},${input1},1] -t rigid[0.1] -m MI[${template},${input1},1,32,Regular,0.25] -c [200×200×200×0,1e-8,10] -- shrink-factors 12×8×4×2 --smoothing-sigmas 4×3×2×1vox -t Affine[0.1] -m MI[${template},${input1},1,32,Regular,0.25] -c [200×200×200×0,1e-8,10] -- shrink-factors 12×8×4×2 --smoothing-sigmas 4×3×2×1 -t SyN[0.01,6,0.5] -m CC[${template},${input1},1,2] -c [200×200×200×200×10,1e-7,10] --shrink- factors 12×8×4×2×1 --smoothing-sigmas 4×3×2×1×0

followed by applying the transformation files on the HCR image channels using the ANTs command:

antsApplyTransforms -d 3 -v 0 -- float -n WelchWindowedSinc -i ${input3} -r ${template} -o ${output4} -t ${output1}1Warp.nii.gz -t ${output1}0GenericAffine.mat

All the registered HCR data used in this study are publicly available through the *mapzebrain.org* atlas.

Confocal imaging

HCR labeled or immunostained samples were embedded in 2% low-melting agarose in 1x DPBS (Dulbecco's PBS) and imaged with a Zeiss LSM700 confocal scanning microscope (upright), equipped with a 20x water immersion objective. Z-stacks, composing 2 tiles (or 1 tile for functional HCR experiment), were taken and stitched to produce a final image with size of 1039 × 1931 pixel (463.97 × 862.29 μm, 1 μm in z).

Pixel intensity quantification of HCR data

For each HCR labeled gene, three larvae were imaged and registered as described above. A maximum intensity projection was generated for each image for planes z289-z291. Coronal sections were generated using Fiji "reslice" option[63], and the maximum intensity projection was generated for planes x463-465. ROIs spanning the SPV for both the transverse and coronal section were used to measure the pixel intensity profile using a custom Fiji macro. The data was analyzed and plotted using R.

Cell centroids labeling

Cell centroids in the HCR data were manually labeled using *napari* points layer tool[64], by examination of HCR signal together with the nuclear labeling of the *Tg(elavl3:H2b-GCaMP6s)*. The points were then registered onto a reference brain using ANTs and the R package ANTsR. The nearest-neighbor distances between centroids were measured in 3D using the R package spatstat[65]. The centroids were visualized using the R package Plotly, hierarchically clustered using complete linkage method implemented in the "hclust" function with default parameters, and plotted using the R package *pheatmap*[66].

Functional two-photon calcium imaging of *Tg(elavl3:H2b-GCaMP6s)*

Two-photon functional calcium imaging was performed on 6–8 dpf *Tg(elavl3:H2b-GCaMP6s)* larvae that expresses a nuclear calcium indicator in all neurons, without paralysis or anesthesia. The animals were embedded in 2% agarose and mounted onto the stage of a modified two-photon moveable objective microscope (MOM, Sutter Instrument, with resonant-galvo scanhead) with a ×20 objective (Olympus XLUMPLFLN, NA 1.0) and recorded for 20 min. Fish that drifted along the dorsoventral axis in the preparation were excluded from analysis. Volumetric imaging of the tectum was performed with a custom-built remote focusing arm [38]. Refocusing through the remote arm enabled rapid sequential imaging of 6 planes (512x512 px) spanning 60-100 μm of the tectum along the dorsoventral axis at 5 volumes per second. In each fish neuronal activity in the tectum was recorded over two 10-minute sessions to cover the whole tectum, resulting in 12 imaging planes per fish in total. Laser power out of the objective ranged from 10 mW to 15 mW.

Two-photon functional calcium imaging of transgenic lines

Animals were embedded and placed under a commercial two-photon laser scanning microscope (Femtonics) as previously described[67]. Sequential single-plane imaging at 1.5 fps was performed at 4-

7 different depths along the tectum for a 10-minute session each, with the same stimulus set as detailed below. No anatomical stack (see below) was acquired from these animals, hence no registration was performed.

Visual stimulation

Visual stimuli were designed with PsychoPy and projected by an LED projector (Texas Instruments, DLP Lightcrafter 4500, with 561 nm long-pass filter) from below onto Rosco tough rolux 3000 diffusive paper water-immersed in a 10 cm petri dish. The embedded animal was placed into a 6 cm petri dish on top of the diffusive paper in the larger dish, with a spacer in between that ensured a water film between the diffusive paper and the smaller petri dish. The fish was placed at 12 mm distance from the projection screen. The fish head was manually centered in the imaging chamber, aided by projecting crosshairs on the screen. Stimuli were shown in a predetermined sequence: gratings, dot motion (8x, see below for details), gratings, OFF ramp, ON ramp, looming (2x). All stimuli were shown black on a red background to not interfere with the green GCaMP fluorescence signal. Individual stimulus presentations were separated by 20 seconds inter-trial intervals, except for the two loom stimuli, for which a 1-min interval was used. The whole duration of the stimulus protocol was 10 minutes.

Grating

A grating moving caudo-rostrally with respect to the fish was shown once at the beginning and after the dot stimuli with 20 mm width and 2 Hz temporal frequency for 20 seconds.

Dot motion

A black dot moving on a circular trajectory (radius, 18 mm) was shown starting in front of the fish. The dot stimulus moved either in discrete jumps at 1.5 Hz or perceptually smooth at 60.0 Hz (projector frame rate) with the same overall speed of 5 mm s^{-1} (15.9 degrees (deg) s^{-1}), resulting in a stimulus duration of 22.6 seconds. Each frequency was presented using a dot diameter of 4 mm (12.7 deg). Both clockwise and counter-clockwise presentations were shown, resulting in 4 different stimuli. The whole dot stimulus set was repeated twice in each session, so 8 dot stimuli were shown in succession.

OFF/ON ramp

Whole-field luminance of the projected blank image was decreased to zero over the course of 2 seconds, and ramped up to normal background luminance within 2 seconds after 20 seconds delay.

Looming

An expanding disk was displayed with expansion from 0.6 deg to 110 deg in 83 ms centered below the fish.

z-Stack acquisition, registration and ROI matching

After each functional recording, a high-resolution 2-photon *z*-stack of large parts of the brain including the full midbrain region was taken (1,024 × 1,024 pixels, 1 µm in *z*, 835 nm laser wavelength, plane averaging 100×). Each time series average of the 12 imaging planes were registered to this stack using the *scikit-learn* template matching algorithm. The 2-photon brain volume was then registered to the volume of the first round HCR confocal imaging as described above (see **HCR image registration**). To transform functional ROIs from 2-photon space into HCR space, ROI pixel coordinates were transformed first from imaging plane reference frame (RF) to 2-photon z-stack RF and finally to the first round HCR RF the by running the ANTs command antsApplyTransformsToPoints two times using the respective transformation matrices from each registration step. HCR cell centroid annotations from each round were transformed into the first round HCR RF, and all coordinates were used as seeds for generating 3x3 pixel volumes that were overlaid with registered functional ROI pixels. HCR centroids were assigned to a functional ROI based on the largest fractional overlap. Finally, all assigned as well as unassigned functional ROIs were registered to the average brain as described above.

Data analysis for two-photon imaging

Suite2p[68] was used for motion correction, ROI detection, classification and signal extraction (time constant *tau*=7 s, diameter=4 px). In detail, raw recording files were deinterleaved into individual time series for each imaging plane. Rigid and non-rigid motion correction was performed with *suite2p* on a low-pass filtered time series in xy (gaussian, sigma=4). The motion-correction shifts were applied to the raw imaging time series. ROIs were detected on fivefold downsampled & motion-corrected time series and fluorescent traces were extracted using the average pixel intensities of ROIs over time. All functional ROIs were initially thresholded based on built-in *suite2p* classification algorithm *iscell* and an anatomical tectal mask drawn in the reference brain (see mapzebrain.org).

Response score

For each stimulus, a regressor was constructed by convolving a boxcar function with an exponential decay kernel that mimics the H2B::GCaMP6s off-kinetics. The resulting 8 regressors were separately fitted to the calcium trace of each functional ROI, using a linear regression model on the stimulus time window. The response score was calculated as the product of the regression coefficient (equivalent to dF/F) and the coefficient of determination R^2. For clustering and dimensionality reduction (Fig 6 f-h), the analysis included all functional ROIs that scored above the 95th percentile of the population response score for any of the visual stimuli. Response score vectors of all high-scoring neurons excluding any t-type positive ROIs (n=7127) were scaled to unit variance and zero mean for subsequent analysis.

Hierarchical clustering & embedding

Functional clusters were identified in a two-step analysis: First, exemplars of the 7127 high-scoring ROIs in 8-dimensional functional space were identified using affinity propagation (*sklearn.cluster.AffinityPropagation*, default parameters). Exemplars with less than 16 associated ROIs were excluded from subsequent analysis The remaining 145 exemplars were clustered using hierarchical clustering (*scipy.cluster.hierarchy.linkage*, method='complete', metric='correlation'; *scipy.cluster.hierarchy.fcluster,* criterion='maxclust'). In parallel, the 2-dimensional embedding for visualizing the tuning manifold was computed from the 8-dimensional response vectors of all high-scoring ROIs with T-distributed Stochastic Neighbor Embedding (t-SNE, *sklearn.manifold.TSNE,* default parameters).

Nearest neighbor t-type frequencies

Fold-changes in nearest neighbor frequencies of different t-types were calculated for each functional ROI as the relative frequency of a certain t-type within the k=50 euclidean nearest neighbors in 8-dimensional functional space divided by the relative frequency of the same t-type within all t-type+ ROIs. This calculation was performed for each high-scoring ROI and the fold-change values were then used as a color-code in the t-SNE embedding to visualize the localization of t-types on the tuning manifold.

Anatomical overlap metric

3D coordinates of each t/f-cluster that contained more than 10 ROIs were used to generate a gaussian kernel density estimate with *scipy.stats.gaussian_kde(bandwidth=0.75)*. For computing pairwise overlap, the KDEs were sampled, normalized, and the minimum of the joint KDEs was taken at each point. The overlap metric is bounded from 0 to 1 (0 if no overlap, near 1 if the same). Controls were generated by shuffling t-type labels of all ROIs in the whole dataset.

T-type classification

Response scores of t-type+ ROIs were scaled to unit variance and zero mean. A support vector machine (SVM) classifier (*sklearn.svm.SVC*, kernel='rbf', gamma='scale', C=1) was trained on 90 % of all t-type+ response vectors and gene labels. To counter the biased distribution of t-types, the training data was upsampled so that each t-type had 1000 samples. Evaluation of the classifier performance was done on 10 % holdout test data. This process was repeated 20 times with permutated training/test data splits. The same classification was performed with anatomical centroid positions of t-type+ ROIs as dependent variables as well as using both response vectors and anatomical positions. Each classification was run again with shuffled marker gene labels as negative control.

Generation of knock-in transgenic lines

The knock-in (KI) lines *Tg(sp5l:QF2)mpn421*, *Tg(atf5b:QF2)mpn423* and *Tg(itpr1b:QF2)mpn424, Tg(pcbp3:QF2)mpn429* were generated by locus-specific insertions using CRISPR-Cas9 and the GeneWeld approach[69]. gRNA target sequences were identified using the CCTop tool[70]. The gRNA target sequences are: *atf5b* 5'-ATTTGGACGTCATGCTCCAGAGG-3' ; *itpr1b* 5'-CATCTGCTCCCTGTATGCGGAGG-3'; *pcpb3* 5'-CATGAGGAGCCGGATGGTCAGGG-3'*; sp5l* 5'-AGGCTCGCAGCTCCCTTACGAGG-3'. Short homology sequences of 48bp spanning the upstream and downstream of gRNA site were ordered as complementary oligonucleotides (MWG) and cloned into donor plasmids using the GoldenGATEway strategy[71]. Universal gRNAs (ugRNA) (Wierson et al., 2020) were introduced into the donor to release the insert from plasmid after injection. The order of components of all the donor constructs was the following: ugRNA, upstream homology arm, short GSG linker, T2A, QF2, polyA signal, downstream homology arm and second ugRNA (inverted). CRISPR-Cas9 RNP complex was prepared at a concentration of 1.5 µM as described before[3]. The gRNA was produced by annealing customized crRNA (IDT, Alt-R® CRISPR-Cas9 crRNA) with tracrRNA (IDT, CAT# 1072533) in annealing buffer (IDT, CAT# 11-05-01-12). The gRNA was incubated with Cas9 protein (IDT, CAT# 1081060) for 15 minutes at 37°C and the donor plasmid was added to the injection mix, at a final concentration of 20 ng/µl. The CRISPR-Cas9 mix was injected into *Tg(QUAS:epNTR-RFP)mpn165* embryos at the single-cell stage. Positive transient expressor fish were raised and screened at adulthood for germline transmission.

Cellular tracing and morphology analysis

Single neurons were sparsely labeled either during the KI generation procedure in mosaic F0 animals, or by transiently microinjecting 12.5 ng/µL QUAS:eGFP-caax into the *Tg(atf5b:QF2)mpn423, Tg(itpr1b:QF2)mpn424, Tg(pcbp3:QF2)mpn429 or Tg(sp5l:QF2)mpn421* transgenic embryos at the single-cell stage. At 6 dpf the injected larvae were anesthetized in a lethal dose of tricaine, fixed in 4% PFA and immunostained with Mouse anti-ERK1/2 (Cell Signaling Technology) and Chicken anti-GFP (Invitrogen), according to the protocol previously published[35].

Confocal imaging was performed as described above. Individual neurons were semi-automatically traced using the freeware NeuTube[72], saved as SWC files and registered to the mapzebrain.org atlas using ANTs as described above and previously[35].

The traced neurons were plotted using the R package natverse[73] and manually clustered according to the projection terminals. A matrix for the anatomical crossing areas for each neuron was generated with the *mapzebrain.org* atlas, and the heatmap was plotted using the R package pheatmap[66].

Code availability

All the python, R and imageJ custom scripts used in this study will be made publicly available upon publication.

Acknowledgments

We thank Mariam Al Kassar and Nouwar Mokayes for their assistance in mapping neuronal traces to the *mapzebrain.org*. We thank Hagar Lavian, Ruben Portugues and Takashi Kawashima for fruitful discussions. We thank all of the Baier lab members for their support. Funding was provided by the Max Planck Society. I.S. was supported by an Alexander von Humboldt foundation research fellowship and by the Weizmann Institute of Science Advancing Women in Science bridge position program. J.K. and M.S were supported by a Boehringer Ingelheim Fonds graduate fellowship. J.L. was supported by a NARSAD Young Investigator Award.

Competing interests

The authors declare no competing interests.

References

1. Taylor, S. R. *et al.* Molecular topography of an entire nervous system. *Cell* **184**, 4329-4347.e23 (2021).

2. Goetz, J. *et al.* Unified classification of mouse retinal ganglion cells using function, morphology, and gene expression. *Cell Rep.* **40**, (2022).

3. Kölsch, Y. *et al.* Molecular classification of zebrafish retinal ganglion cells links genes to cell types to behavior. *Neuron* **109**, 645–662 (2021).

4. Förster, D. *et al.* Retinotectal circuitry of larval zebrafish is adapted to detection and pursuit of prey. *eLife* **9**, e58596 (2020).

5. Helmbrecht, T. O., dal Maschio, M., Donovan, J. C., Koutsouli, S. & Baier, H. Topography of a Visuomotor Transformation. *Neuron* **100**, 1429-1445.e4 (2018).

6. Yuste, R. *et al.* A community-based transcriptomics classification and nomenclature of neocortical cell types. *Nat. Neurosci.* **23**, 1456–1468 (2020).

7. Zeng, H. What is a cell type and how to define it? *Cell* **185**, 2739–2755 (2022).

8. Zeng, H. & Sanes, J. R. Neuronal cell-type classification: challenges, opportunities and the path forward. *Nat. Rev. Neurosci.* **18**, 530–546 (2017).

9. Hobert, O. Terminal Selectors of Neuronal Identity. *Curr. Top. Dev. Biol.* **116**, 455–475 (2016).

10. Gouwens, N. W. *et al.* Integrated Morphoelectric and Transcriptomic Classification of Cortical GABAergic Cells. *Cell* **183**, 935-953.e19 (2020).

11. Gouwens, N. W. *et al.* Classification of electrophysiological and morphological neuron types in the mouse visual cortex. *Nat. Neurosci.* **22**, 1182–1195 (2019).

12. Abbott, L. F. & Regehr, W. G. Synaptic computation. *Nature* **431**, 796–803 (2004).

13. Yap, E.-L. & Greenberg, M. E. Activity-regulated transcription: bridging the gap between neural activity and behavior. *Neuron* **100**, 330–348 (2018).

14. Bugeon, S. *et al.* A transcriptomic axis predicts state modulation of cortical interneurons. *Nature* **607**, 330–338 (2022).

15. Scala, F. *et al.* Phenotypic variation of transcriptomic cell types in mouse motor cortex. *Nature* **598**, 144–150 (2021).

16. Peng, H. *et al.* Morphological diversity of single neurons in molecularly defined cell types. *Nature* **598**, 174–181 (2021).

17. Isa, T., Marquez-Legorreta, E., Grillner, S. & Scott, E. K. The tectum/superior colliculus as the vertebrate solution for spatial sensory integration and action. *Curr. Biol.* **31**, R741–R762 (2021).

18. Robles, E., Laurell, E. & Baier, H. The retinal projectome reveals brain-area-specific visual representations generated by ganglion cell diversity. *Curr. Biol. CB* **24**, 2085–2096 (2014).

19. Galant, S. *et al.* Embryonic origin and lineage hierarchies of the neural progenitor subtypes building the zebrafish adult midbrain. *Dev. Biol.* **420**, 120–135 (2016).

20. Hall, Z. J. & Tropepe, V. Visual Experience Facilitates BDNF-Dependent Adaptive Recruitment of New Neurons in the Postembryonic Optic Tectum. *J. Neurosci. Off. J. Soc. Neurosci.* **38**, 2000–2014 (2018).

21. Nakamura, H. Regionalization of the optic tectum: combinations of gene expression that define the tectum. *Trends Neurosci.* **24**, 32–39 (2001).

22. Lovett-Barron, M. *et al.* Multiple convergent hypothalamus–brainstem circuits drive defensive behavior. *Nat. Neurosci.* **23**, 959–967 (2020).

23. Bradford, Y. M. *et al.* Zebrafish Information Network, the knowledgebase for Danio rerio research. *Genetics* **220**, iyac016 (2022).

24. Korsunsky, I. *et al.* Fast, sensitive and accurate integration of single-cell data with Harmony. *Nat. Methods* **16**, 1289–1296 (2019).

25. Cao, J. *et al.* The single-cell transcriptional landscape of mammalian organogenesis. *Nature* **566**, 496–502 (2019).

26. Moldovan, G.-L., Pfander, B. & Jentsch, S. PCNA, the Maestro of the Replication Fork. *Cell* **129**, 665–679 (2007).

27. Fu, M., Wang, C., Li, Z., Sakamaki, T. & Pestell, R. G. Minireview: Cyclin D1: Normal and Abnormal Functions. *Endocrinology* **145**, 5439–5447 (2004).

28. Jurisch-Yaksi, N., Yaksi, E. & Kizil, C. Radial glia in the zebrafish brain: Functional, structural, and physiological comparison with the mammalian glia. *Glia* **68**, 2451–2470 (2020).

29. Lange, C. *et al.* Single cell sequencing of radial glia progeny reveals the diversity of newborn neurons in the adult zebrafish brain. *Dev. Camb. Engl.* **147**, dev185595 (2020).

30. Zhang, H., Li, X., Liao, D., Luo, P. & Jiang, X. Alpha/Beta-Hydrolase Domain-Containing 6: Signaling and Function in the Central Nervous System. *Front. Pharmacol.* **12**, 784202 (2021).

31. Martin, A. *et al.* Single-Cell RNA Sequencing Characterizes the Molecular Heterogeneity of the Larval Zebrafish Optic Tectum. *Front. Mol. Neurosci.* **15**, 13 (2022).

32. Achim, K. *et al.* The role of Tal2 and Tal1 in the differentiation of midbrain GABAergic neuron precursors. *Biol. Open* **2**, 990–997 (2013).

33. Sammeta, N., Hardin, D. L. & McClintock, T. S. Uncx regulates proliferation of neural progenitor cells and neuronal survival in the olfactory epithelium. *Mol. Cell. Neurosci.* **45**, 398–407 (2010).

34. Tambalo, M., Mitter, R. & Wilkinson, D. G. A single cell transcriptome atlas of the developing zebrafish hindbrain. *Development* **147**, dev184143 (2020).

35. Kunst, M. *et al.* A cellular-resolution atlas of the larval zebrafish brain. *Neuron* **103**, 21–38 (2019).

36. Shainer, I. *et al.* A single-cell resolution gene expression atlas of the larval zebrafish brain. *Sci. Adv.* **9**, eade9909 (2023).

37. Livesey, F. J. & Cepko, C. L. Vertebrate neural cell-fate determination: lessons from the retina. *Nat. Rev. Neurosci.* **2**, 109–118 (2001).

38. Kappel, J. M. *et al.* Visual recognition of social signals by a tectothalamic neural circuit. *Nature* 1–7 (2022).

39. Meek, J. & Schellart, N. a. M. A golgi study of goldfish optic tectum. *J. Comp. Neurol.* **182**, 89–121 (1978).

40. Romeskie, M. & Sharma, S. C. The goldfish optic tectum: A golgi study. *Neuroscience* **4**, 625–642 (1979).

41. Scott, E. & Baier, H. The cellular architecture of the larval zebrafish tectum, as revealed by Gal4 enhancer trap lines. *Front. Neural Circuits* **3**, (2009).

42. Vanegas, H., Laufer, M. & Amat, J. The optic tectum of a perciform teleost I. General configuration and cytoarchitecture. *J. Comp. Neurol.* **154**, 43–60 (1974).

43. Fernandes, A. M. *et al.* Neural circuitry for stimulus selection in the zebrafish visual system. *Neuron* **109**, 805-822.e6 (2021).

44. Kebschull, J. M. & Zador, A. M. Cellular barcoding: lineage tracing, screening and beyond. *Nat. Methods* **15**, 871–879 (2018).

45. Ortiz, C. *et al.* Molecular atlas of the adult mouse brain. *Sci. Adv.* **6**, eabb3446 (2020).

46. Yao, Z. *et al.* A high-resolution transcriptomic and spatial atlas of cell types in the whole mouse brain. 2023.03.06.531121 Preprint at https://doi.org/10.1101/2023.03.06.531121 (2023).

47. Bakken, T. E. *et al.* Comparative cellular analysis of motor cortex in human, marmoset and mouse. *Nature* **598**, 111–119 (2021).

48. Di Bella, D. J. *et al.* Molecular logic of cellular diversification in the mouse cerebral cortex. *Nature* **595**, 554–559 (2021).

49. Farrell, J. A. *et al.* Single-cell reconstruction of developmental trajectories during zebrafish embryogenesis. *Science* **360**, eaar3131 (2018).

50. Xie, Z. *et al.* Transcriptomic encoding of sensorimotor transformation in the midbrain. *eLife* **10**, e69825 (2021).

51. de Vries, S. E. J. *et al.* A large-scale standardized physiological survey reveals functional organization of the mouse visual cortex. *Nat. Neurosci.* **23**, 138–151 (2020).

52. Baden, T., Euler, T. & Berens, P. Understanding the retinal basis of vision across species. *Nat. Rev. Neurosci.* **21**, 5–20 (2020).

53. Zhou, M. *et al.* Zebrafish Retinal Ganglion Cells Asymmetrically Encode Spectral and Temporal Information across Visual Space. *Curr. Biol. CB* **30**, 2927-2942.e7 (2020).

54. Li, Y. & Meister, M. Functional Cell Types in the Mouse Superior Colliculus. 2022.04.01.486789 Preprint at https://doi.org/10.1101/2022.04.01.486789 (2022).

55. Mearns, D. S., Donovan, J. C., Fernandes, A. M., Semmelhack, J. L. & Baier, H. Deconstructing hunting behavior reveals a tightly coupled stimulus-response loop. *Curr. Biol.* **30**, 54–69 (2020).

56. El-Danaf, R. N., Rajesh, R. & Desplan, C. Temporal regulation of neural diversity in Drosophila and vertebrates. *Semin. Cell Dev. Biol.* **142**, 13–22 (2023).

57. Cembrowski, M. S. & Menon, V. Continuous Variation within Cell Types of the Nervous System. *Trends Neurosci.* **41**, 337–348 (2018).

58. Vlasits, A. L., Euler, T. & Franke, K. Function first: classifying cell types and circuits of the retina. *Curr. Opin. Neurobiol.* **56**, 8–15 (2019).

59. Wu, Y. E., Pan, L., Zuo, Y., Li, X. & Hong, W. Detecting Activated Cell Populations Using Single-Cell RNA-Seq. *Neuron* **96**, 313-329.e6 (2017).

60. Hao, Y. *et al.* Integrated analysis of multimodal single-cell data. *Cell* **184**, 3573-3587.e29 (2021).

61. Qiu, X. *et al.* Reversed graph embedding resolves complex single-cell trajectories. *Nat. Methods* **14**, 979–982 (2017).

62. Avants, B. B. *et al.* A reproducible evaluation of ANTs similarity metric performance in brain image registration. *Neuroimage* **54**, 2033–2044 (2011).

63. Schneider, C. A., Rasband, W. S. & Eliceiri, K. W. NIH Image to ImageJ: 25 years of image

analysis. *Nat. Methods* **9**, 671–675 (2012).

64. Sofroniew, N. *et al.* napari: a multi-dimensional image viewer for Python. (2022) doi:10.5281/zenodo.7117339.

65. Baddeley, A., Rubak, E. & Turner, R. *Spatial point patterns: methodology and applications with R*. (CRC press, 2015).

66. Kolde, R. Pheatmap: pretty heatmaps. *R Package Version* **1**, 726 (2012).

67. Förster, D., Maschio, M. D., Laurell, E. & Baier, H. An optogenetic toolbox for unbiased discovery of functionally connected cells in neural circuits. *Nat. Commun.* **8**, 116 (2017).

68. Pachitariu, M. *et al.* Suite2p: beyond 10,000 neurons with standard two-photon microscopy. 061507 Preprint at https://doi.org/10.1101/061507 (2017).

69. Wierson, W. A. *et al.* Efficient targeted integration directed by short homology in zebrafish and mammalian cells. *eLife* **9**, e53968 (2020).

70. Stemmer, M., Thumberger, T., Keyer, M. del S., Wittbrodt, J. & Mateo, J. L. CCTop: An Intuitive, Flexible and Reliable CRISPR/Cas9 Target Prediction Tool. *PLOS ONE* **10**, e0124633 (2015).

71. Kirchmaier, S., Lust, K. & Wittbrodt, J. Golden GATEway Cloning – A Combinatorial Approach to Generate Fusion and Recombination Constructs. *PLOS ONE* **8**, e76117 (2013).

72. Feng, L., Zhao, T. & Kim, J. neuTube 1.0: A New Design for Efficient Neuron Reconstruction Software Based on the SWC Format. *eNeuro* **2**, ENEURO.0049-14.2014 (2015).

73. Bates, A. S. *et al.* The natverse, a versatile toolbox for combining and analysing neuroanatomical data. *Elife* **9**, e53350 (2020).

3. Discussion

The senses of the brain provide access to the sensory *Umwelt*, but at the same time gate and thus constrain its perception. At the sensory periphery, photoreceptors in the retina capture only certain wavelength ranges of light, while hair cells in the inner ear capture only a certain spectrum of auditory frequencies. Further downstream, these primary information channels converge and integrate to discern key features of the sensory environment. In many cases, hard-wired feature detectors recognize a specific ethologically significant stimuli such as the sight of an approaching predator or the scent of a conspecific. Activation of these feature detectors can then initiate innate, stereotyped behaviors - such as escape or mating - that increase survival prospects. The brain of the developing zebrafish employs hard-wired feature detectors to enable several innate behavioral responses to salient sensory features right after hatching, from prey detecting retinal ganglion cells to thalamic neurons that respond to looming stimuli.

In my thesis, I studied feature detectors for social recognition and molecular underpinnings of different sets of feature detectors in the visual system of developing zebrafish. I discovered an information pathway that detects visual features of conspecifics. Thalamic neurons equip zebrafish with the ability to recognize motion patterns, so-called ‘swim bouts’ of other larvae soon after hatching and innervate brain areas that are conserved nodes for mediating social behaviors. Ultimately, the individual filter properties of these neurons might be a requirement for the formation of a fish shoal. Secondly, I investigated the relationship between functional responses of visual neurons to ethological stimuli and their transcriptomic identities in the larval zebrafish tectum, the main center of sensorimotor transformation. Shainer and I discovered that that a combination of both transcriptomic identity and cell body position in this topographically structured brain region are important determinants neuronal phenotypic traits.

In the following, I will discuss how a hard-wired visual circuit could give rise to a matched filter for bout motion and propose a wiring diagram for a swim-bout motion detector. I will consider whether this visual circuit can be deemed dedicated for social recognition. I will propose multiple roles for this thalamic circuit in different

aspects of affiliative social behavior and draw parallels to thalamic circuits described in other vertebrate species.
I will then elaborate on our definitions of transcriptomic and functional cell types in the tectum. Finally, I will speculate on functional and anatomical diversity of transcriptomic cell types in the larval zebrafish tectum and their role in generating adaptive behavioral responses to ethological stimuli.

3.1 A dedicated circuit for detecting visual social features

In juvenile zebrafish, the replay of characteristic burst-and-glide motion termed bout motion of conspecifics is sufficient to trigger social affiliation (Larsch and Baier, 2018), warranting the hypothesis that specialized circuits of the visual system readily detect these conspecific signals. I have discovered a nucleus in the juvenile zebrafish thalamus that comprises a high concentration of neurons with selective responses to bout motion (Kappel et al., 2022). In my study, a reduced motion stimulus replaced a real conspecific to discover the neural basis of social recognition. Interestingly, the bout motion stimulus is akin to a type of optical illusion called beta motion: An object briefly appears at a certain location, disappears, and reappears at a different location, thereby creating the illusion of directed motion in a human observer (Wertheimer, 1912). In my imaging experiments, juvenile zebrafish perceived systematic variations of these stimuli with altered apparent motion frequencies and distances between individual locations, ranging from large distances between objects and low temporal frequencies to increasingly small distances and high temporal frequencies, i.e. from discontinuous to continuous motion. I recorded the strongest response in dorsal thalamus neurons to the bout frequency matching conspecific motion. When I further refined the experiment to only adjust distances while maintaining the same frequency the preferred overall stimulus speed of dorsal thalamus neurons still matched conspecific swimming speed. Moreover, I changed the degree of beta-like motion by morphing a positional step function via sinusoidal functions into a linear function while keeping bout frequency constant. Here, the stimulus with the strongest apparent motion elicited the strongest response. To exclude that these responses were signaling changes of the visual scene that match self-motion speed, I showed whole-field motion stimuli with the same spatial and

temporal frequencies. These stimuli, alongside grating and looming stimuli, did not yield strong responses in this nucleus. Finally, the acceleration of a naturalistic conspecific motion stimulus was well captured by the mean population response of dorsal thalamus neurons. While only a small fraction of the potential stimulus space was probed, the inferred tuning curves and selective responses argue that this anatomical nucleus acts specifically as a matched filter for conspecific motion statistics.

How could a neural circuit achieve such a selective response? The most common and biologically relevant models for local motion detection are correlation-type models based on spatiotemporal cross-correlation (Borst and Egelhaaf, 1989). The first and most established of them is the Hassenstein-Reichardt model, which takes the difference between two filtered and multiplied luminance signals separated in space (Fig 6a). The distance between two sensors in visual space, or sampling base φ, as well as the delay term ε define the minimal spatial frequency and velocity of the motion stimulus that generate a signal. In the special case of bout motion, Larsch and Baier showed that, in addition to bout frequency, the overall velocity and stimulus size modulate behavioral attraction. Moreover, juvenile zebrafish maintain a preferred distance to virtual and real conspecifics.

3.2 The bout motion detector as an elementary unit for social recognition

A simple bout detector could be a derivation of the Hassenstein-Reichardt detector with overlapping spatial center-surround inhibition, so that only discontinuous, beta-like motion would generate a signal (Fig 6b). The delay and sampling base could be set so that conspecific displacement at the preferred inter-animal-distance results in the biggest downstream signal. Such a dedicated bout motion detector could reside already in the eye: Bipolar cells with center-surround receptive fields are described in many vertebrate species (Euler et al., 2014). Given an appropriate spacing of receptive field centers and inhibitory surround, multiple bipolar cells in series could provide a downstream saliency signal in retinal ganglion cells that detects the preferred distance, speed and bout frequency of a conspecific.

While this implementation is a possible solution to a motion detector for preferred bout frequency, speed and distance simultaneously, it would not be a sufficient

signal in the context of affiliative behavior. To maintain a preferred distance to conspecifics, juvenile zebrafish have to detect each other's motion patterns from a range of distances and respond with approach or avoidance accordingly. Approach and avoidance in response to motion cues are elementary behaviors that also underlie hunting and escape, which are implemented in the larval zebrafish tectum (Barker and Baier, 2015; Helmbrecht et al., 2018).

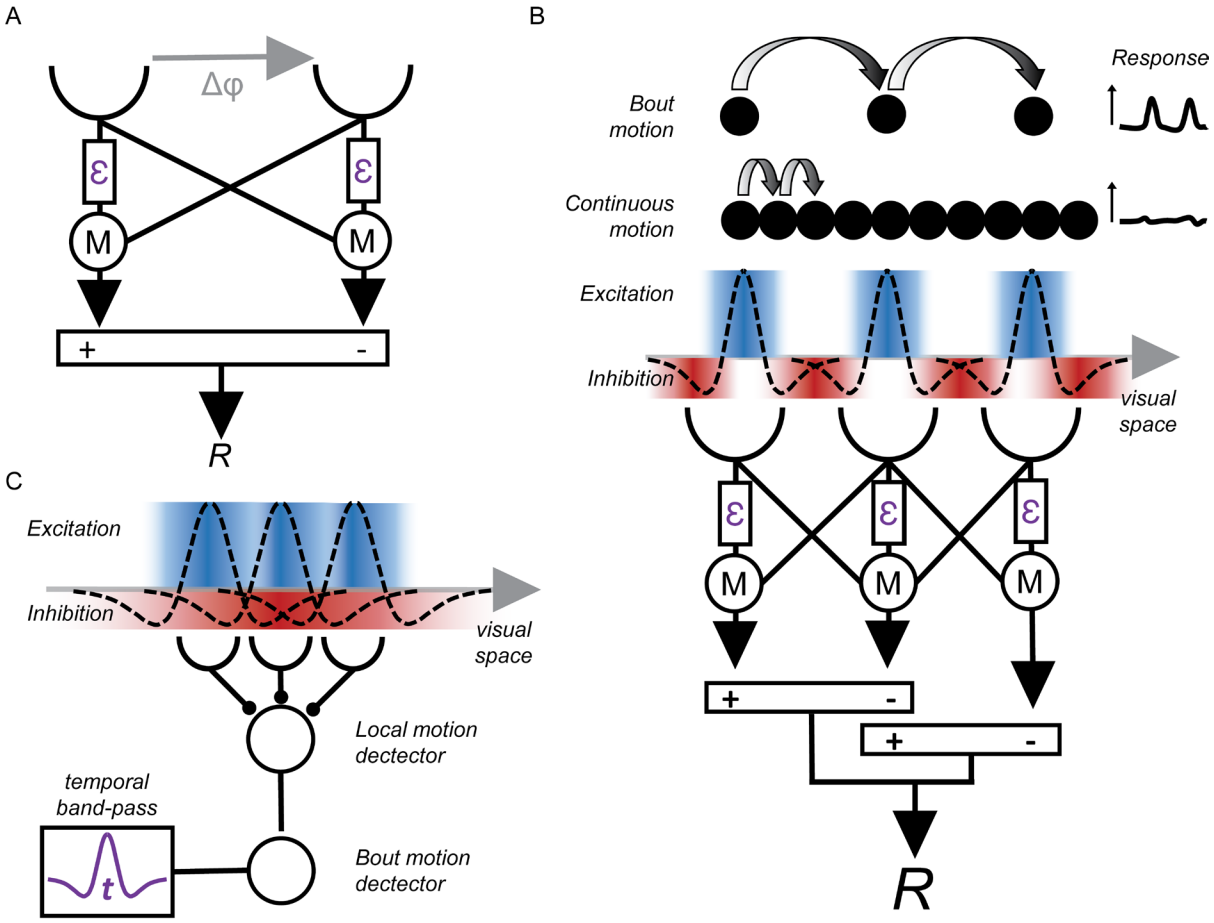

Figure 6: Hassenstein-Reichardt detector as a basis for processing bout motion

(A) The classical Hassenstein-Reichardt detector model is based on two sensors that are reciprocally connected, and whose signals are multiplied (M) and summed (+/-). Through a delay term $\mathcal{E}$, the preferred direction of motion and speed can be specified, while the sampling base φ limits the spatial frequencies that can be detected.

(B) By adding non-linear spatial band-pass filters on top that represent particularly arranged center-surround inhibition in space, the model responds only to apparent motion of a specific bout frequency, speed and stimulus size.

(C) A canonical local motion detector model can be turned into a bout detector downstream through an intracellular temporal band-pass filter for the preferred bout frequency.

Distance-invariant bout detection could be achieved by separating spatial and temporal components of the stimulus: Neurons that selectively respond to conspecific motion frequencies across a range of stimulus sizes or distances could serve as a parallel, contextual signal (Fig. 6C). These types of flicker responses via temporal bandpass filters are common in the visual system across species, from salamander retina to monkey visual cortex (Armstrong-Gold and Rieke, 2003; Hawken et al., 1996). Hypothetical bout frequency detectors in the zebrafish retina or tectum could innervate tectal neurons with spatial high- or low-pass filters, in combination generate approach or avoidance signals when a conspecific stimulus is too far away or too close, respectively. Since size-selective visual tuning for decision-making is a hallmark of sensory processing in the tectum (Barker and Baier, 2015), it might also compute stimulus size dependent social approach and avoidance in this structure. Indeed, we have found neurons tuned to bout motion in the tectum, distributed broadly along its anatomical retinotopic map. If tectal neurons mediate the instantaneous behavioral response to a bout motion stimulus, what could be the role of the dorsal thalamus?

3.3 Diverse functions for the tectothalamic bout detection circuit

We discovered that motion frequency tuning of DT-BPNs in juvenile zebrafish recapitulates the stimulus optimum for behavioral attraction. Upon fixing bout frequency to the optimum of 1.5 Hz but modulating overall velocity, we found that DT neurons show an optimum response to conspecific speed. Recording DT-BPN responses to naturalistic conspecific motion stimuli revealed that their collective activity represents stimulus acceleration. We showed through electron microscopic reconstruction of the DT circuit that sensory input is most likely coming from the tectum, with multiple tectal periventricular projection neurons (PVPNs) converging on individual DT neurons.

In turn, the diverse downstream connectivity of individual DT neurons suggests multiple roles for this node: First, reciprocal loops between tectal BPNs and DT-BPNs as well as between DT-BPNs could selectively amplify tectal representation of conspecifics during social affiliation and thus enable sustained pursuit over hours, as

observed by Larsch and Baier. This recurrent amplification could serve to keep the conspecific locked in a preferred area of the visual field.

Additionally, DT neurons might regulate competition between multiple conspecific stimuli or social and non-social stimuli (Fig. 7A). Traditionally, the tectum/superior colliculus is thought to contain a ‘saliency map’ that selectively amplifies certain visual stimuli through focal excitation and global inhibition (Ben-Tov et al., 2015; Knudsen, 2018). Previous work showed that developing zebrafish turn preferentially towards the side with more conspecifics (Hinz and de Polavieja, 2017). This competition between visual hemifields and tectal hemispheres could be resolved through DT neurons that weigh incoming bout motion information from the tectum and either selectively enhance or suppress stimulus representations on one tectal hemisphere indirectly through the nucleus isthmi or directly via connections to the tectum. This role would be in accordance with the axonal projections to the tectum and nucleus isthmi we found as well as a recent study that detailed tectal-isthmic interactions during stimulus competition (Fernandes et al., 2021).

In our connectomics analysis, DT neurons also project to the medulla oblongata, part of the brainstem. Here, incoming activity driven by bout motion might instruct the temporal alignment of motion between conspecifics, which has been described previously for juvenile as well as adult zebrafish (Dreosti et al., 2015; Stednitz et al., 2018). In the adult stage, social orienting behavior is dependent on a group of cholinergic neurons in the ventral telencephalon (Stednitz et al., 2018). Other studies have also focused on the role of the teleost telencephalon in social behavior (Cabrera-Álvarez et al., 2017; Shinozuka and Watanabe, 2004). The *mapzebrain.org* atlas contains several light-microscopic reconstructions of DT neurons that project to the telencephalon, suggesting that social visual information is transmitted to this brain region via DT (Fig. 7B). In our electron-microscopic dataset we did not yet find a direct projection from DT to the telencephalon. This discrepancy might be due to undersampling DT neurons or due to the young age of only 5 dpf in the EM dataset, where this connection might not be established yet.

Lastly, DT responses to conspecific motion might further report the close presence of conspecifics as a homeostatic social signal. It is widely studied that social isolation has long-lasting effects on behavior and physiology in humans and other animals,

and the drive to maintain a social connection is akin to physiological homeostatic systems that regulate hunger or thirst (Matthews and Tye, 2019). Social interactions alleviate stress responses through modulation of the hypothalamic-pituitary-adrenocortical (HPA) system, termed social buffering (Hennessy et al., 2009).

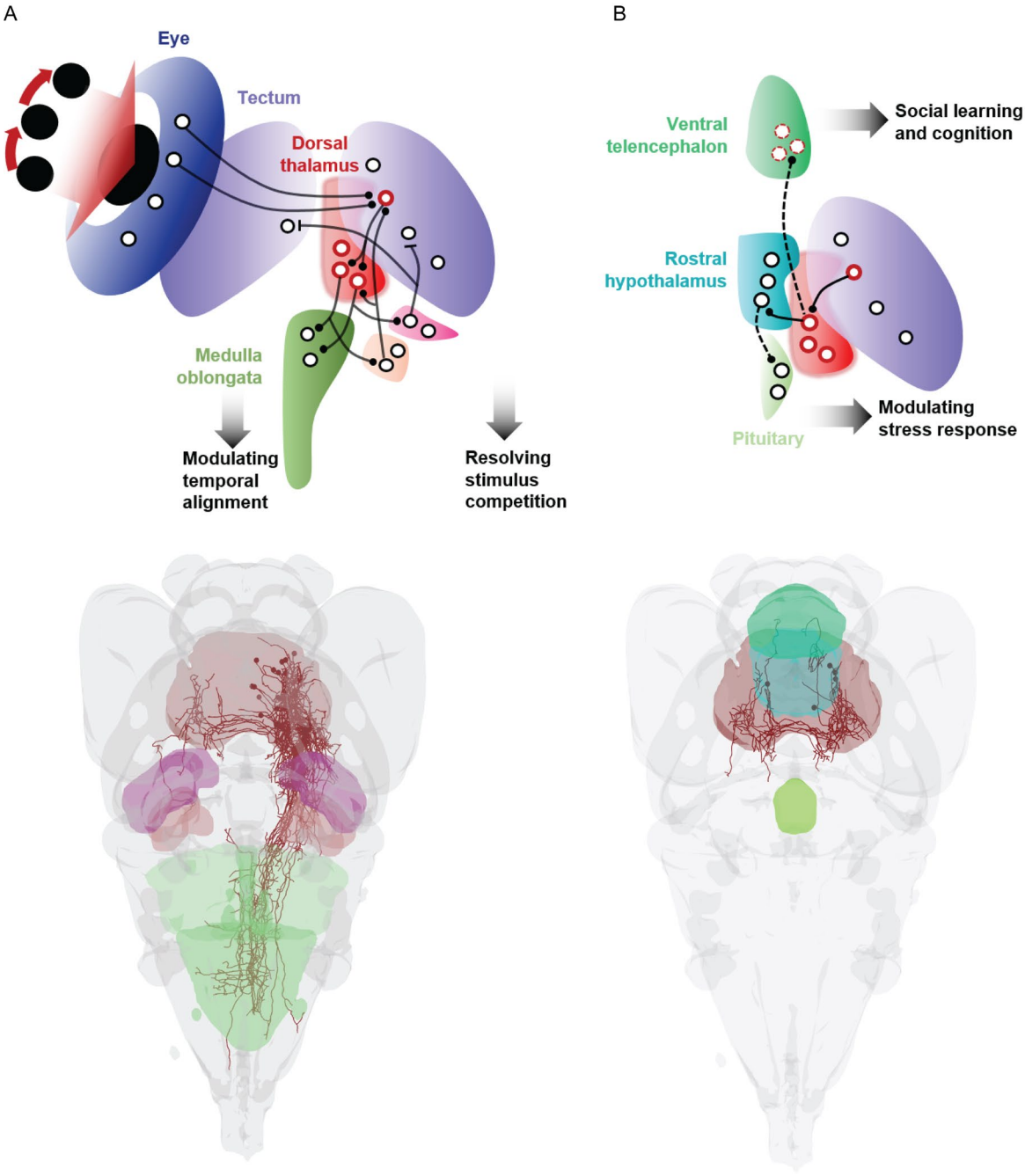

Figure 7: Functional roles of broadly connected dorsal thalamus (DT) neurons for social behavior

(A) Top: DT circuit model for sensorimotor functions. Incoming visual information of tectal BPNs (red circle) reaches DT-BPNs. DT neurons project to both the GABAergic and glutamatergic

regions of nucleus isthmi, which facilitates focal enhancement and global suppression in the tectum to increase saliency of the social stimulus compared to other stimuli in the environment. In parallel, DT neurons project to neurons in the medulla oblongata, where they modulate activity of oscillatory circuits to synchronize bouts between the animal and conspecifics based on perceived bout motion. Bottom: Individual DT neurons from the *mapzebrain* single-cell atlas project to both the nucleus isthmi and medulla oblongata. Tectal neurons and tectum volume are omitted for clarity.

(B) Top: DT circuit model for homeostatic and stateful functions. DT neurons project to the preoptic area (PoA), where the homolog of the mammalian paraventricular nucleus (PVN) resides. Their activity decreases release of corticotropin-releasing hormone (CRH) by PVN neurons, which in turn regulates adrenocorticotropic hormone (ACTH) release by the anterior pituitary, thereby modulating the HPA stress axis. In parallel, DT neurons directly or indirectly project to the telencephalon, where sensory information about conspecifics is integrated for cognitive functions such as social learning. Bottom: DT neurons project to the preoptic area and the telencephalon.

We have demonstrated axonal projections of DT neurons to the preoptic area, anterior (rostral) and intermediate hypothalamus. The homolog of the mammalian paraventricular nucleus (PVN) in zebrafish is likely the preoptic area, whose neurons form axonal contacts with the pituitary gland (Nagpal et al., 2019; Wulliman et al., 2012). Taken together, zebrafish DT neurons might relay conspecific motion cues to the PVN as a social buffering signal that modulates the HPA axis (Fig. 7B). In line with this proposed homeostatic signaling, a recent study showed that selective gene expression level of *parathyroid hormone 2* (*pth2*) in DT of larval and juvenile zebrafish scales with the presence and density of conspecifics, mediated through the detection of social touch (Anneser et al., 2020). The neuropeptide Pth2 has been implicated in the regulation of social behaviors such as maternal care (Cservenák et al., 2013; Gellén et al., 2017). Interestingly, multisensory integration of conspecific signals in combination with *pth2* expression has also been reported for a dorsal thalamic region in rats (Keller et al., 2022). Future studies will show whether individual neurons in zebrafish DT integrate visual and somatosensory conspecific motion cues and whether the information about social environment in DT modulates wider brain and body functions on longer time scales.

Taken together, the DT node for processing bout motion is likely a multi-functional hub that, as we have shown, drives affiliative behavior and likely has additional roles

for social interactions such as social homeostasis, stimulus competition or social cognition.

Is the implication of DT in social behavior a conserved function in other clades and species? Anatomically, the pulvinar complex in the mammalian thalamus is the most likely homolog of the zebrafish DT. Like the zebrafish posterior DT, it receives direct visual input from the superior colliculus, the optic tectum homologe and is further interconnected with different cortical structures such as the visual cortex, prefrontal cortex and amygdala (Bridge et al., 2016; Grieve et al., 2000). In line with the previous speculation on the role of DT in shoaling, the pulvinar nucleus is a central node for visual attention (Benarroch, 2015). In addition, subsets of pulvinar neurons in monkeys and humans respond selectively to face-like stimuli (Nguyen et al., 2013) and emotional facial expressions (Maior et al., 2010), respectively. These analogies make the pulvinar a potential mammalian homolog of the larval zebrafish DT in terms of anatomy as well as function.

3.4 Multimodal identification of tectal cell types in the larval zebrafish

Larval zebrafish DT neurons respond selectively to bout motion without previous exposure, and animals raised in social isolation instantly perform shoaling behavior, implying hard-wired preference to specific bout motion frequency independent of social experience. This is in line with other studies that reported experience-independent functionality of sensory behaviors such as prey capture, though here experience improves hunting skills (Avitan et al., 2020; Oldfield et al., 2020). The larval zebrafish brain needs to be functional right upon hatching, even though the animal is still developing and naïve to many stimuli. To accommodate those two processes simultaneously, transcriptomically defined cell types could make up hard-wired circuits that enable individual behaviors. Recently, Sherman and colleagues showed that even without RGC input, the visual system comprises all transcriptomic cell types or t-types in the correct anatomical locations and fractions in the brain, corroborating the idea that t-types make up building blocks for functional circuits (Sherman et al., 2021). In Shainer, Kappel et al. (2023, in prep.), my colleagues and I aimed at unraveling these building blocks in the larval zebrafish tectum, the main brain area for sensorimotor transformation. We identified t-types in the larval

zebrafish tectum and related them to functional and morphological cell types (Fig. 8). We discovered that a combination of both transcriptomic identity and cell-body position in this topographically structured tissue are important determinants of a neuron's phenotype. Our study detailed for the first time the relationship of functional and transcriptomic identity of neuronal cell types in a brain region that contains a topographic map of sensory and motor space.

3.5 Functional and anatomical diversity of cell types in the larval zebrafish tectum

In our study, we defined f-types as functional clusters based on response scores to 8 discrete visual stimuli. Two recent studies defined functional cell types in V1 and superior colliculus based on visual stimulus responses (Bugeon et al., 2022; Li and Meister, 2022). In our study, we cannot exclude that more exhaustive sampling of stimulus space would reveal additional functional response types that individual t-types would converge on as the smallest common denominator. Yet, our results show that despite the comparatively sparse sampling of the vast potential stimulus space, responses are certainly heterogeneous across all t-types for the given stimulus set. This response diversity within t-types already strictly excludes a one-to-one correspondence between a functional and transcriptomic cell type for the tested marker genes. Further, we found diverse projection patterns within two out of four t-types. This is consistent with previous studies that found diverse morphological traits within cortical interneuron and projection neurons (Peng et al., 2021; Scala et al., 2021). Yet, these studies limited their scope to one type of morphological class, whereas we find both interneurons and projection neurons in individual t-types (Fig. 8B).

Multiple confounding factors could be the source of the observed phenotypic variability within t-types. First, the transcriptomic resolution of our t-type definition might be too shallow. For instance, *atf5b* and *sp5l* are broadly expressed in the tectum and both comprise local interneurons as well as projection neurons. Additional marker genes could further increase the resolution of these cell types: *atf5b*+ and *sp5l*+ cells might be further separated according to *foxb1a* and *barhl1a* expression, respectively, or other genes for which the RNA sequencing depth was not sufficient. While we cannot exclude additional markers that would, in

combination, lead to coherent phenotypic traits, the identified marker genes certainly label neuronal classes that are largely transcriptomically coherent.

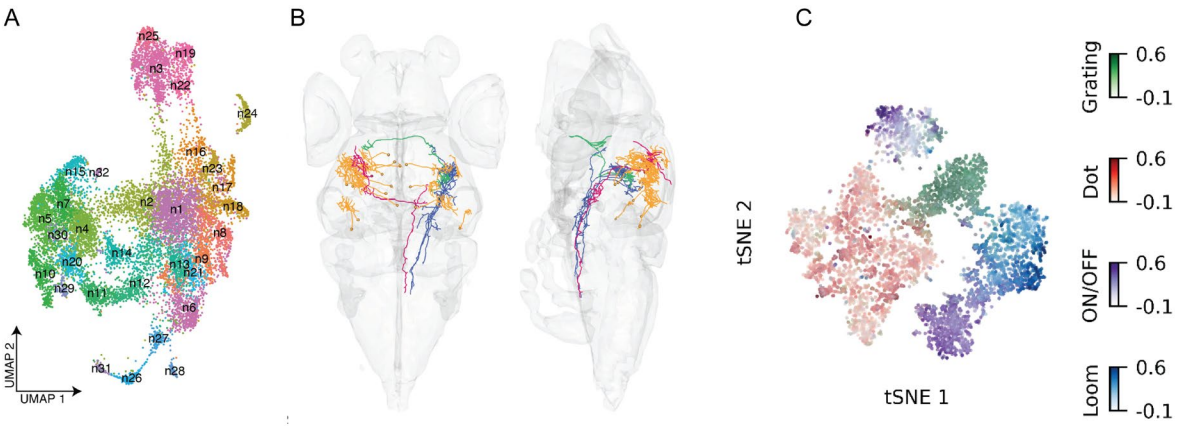

Figure 8: Cell type modalities of the larval zebrafish tectum in their respective spaces

(A) Low-dimensional embedding of tectal neurons according to their transcriptomic profile.
(B) Different morphological types of *atf5b+* tectal neurons in the larval zebrafish standard brain.
(C) Low-dimensional embedding of tectal neurons according to functional activity. Colors indicate response strength to different visual stimuli.

Our discovery of anatomically localized functional subclusters results instead suggest that the more likely explanation for diverse phenotypic traits within t-types are extrinsic factors arising from differential cell-body position within the tectal volume. Whether additional marker genes would anatomically separate t-types in the same fashion as functional preference remains to be established.

Another potential pitfall of our study are the different means of identifying the t-type throughout the study. RNA sequencing determines t-type membership through gene expression across hundreds of genes via a machine-learning algorithm that assigns it a certain cluster. In the imaging experiment, t-types are determined based on the chemically amplified marker gene expression that is largely specific to a cluster and subsequently scored as positive or negative by a human. Finally, neuronal morphologies of different t-types are based marker gene expression where the QF2 RNA sequence was knocked into the native locus as well as the protein concentration of the translated QF2 protein in the neurons. The differences between these categorizations might lead to false positives or false negatives. False

negatives would have few effects on our current interpretation, since un-assigned neurons would not lead to phenotypic variability in the analysis. On the other hand, assigning a given cell to the false cluster might add phenotypic traits that do not match those of the true positive neurons. Yet, we have demonstrated in our studies that neurons of the same t-type share broad functional response preferences between the HCR-based approach and the transgenic lines. Further, we have shown that neurons categorically do not co-express any t-type specific marker genes in our multiplexed HCR labeling approach, demonstrating that these markers are non-overlapping between neuronal populations and thus suited for labeling transcriptomic identity.

With variable visual response profiles and morphology, individual t-types might still have coherent electrophysiological properties. Recent studies in mammals have compared resting membrane potential or spike frequency for the functional characterization of cell types, often finding large consensus between t-type and electrophysiological type. This might also be the case in the tectum. While neurons of the same t-type might be involved in mediating behaviors to different stimuli, their respective circuit function might be stereotyped. For instance, long-range projections of *atf5b*+ tectal neurons could regulate gain control for forward swims either towards a local object of interest or in the context of an optomotor response. Tectal neurons that express *pitx2* might facilitate contrast enhancement across stimuli. Along these lines, t-types might be individual cogs and screws of a machine that have the same functional properties within different circuits, based on where they localize anatomically. Future studies on the individual tectal t-types will show whether transcriptomic identity defines respective circuit functions within tectal neurons.

Lastly, the larval zebrafish brain is still undergoing profound developmental changes. While the tectum needs to provide essential functions for survival throughout this process, its structural and functional architecture probably still changes drastically until adulthood, which is a timespan of more than two months for zebrafish larvae. A recent study of retinal ganglion cell types in the zebrafish retina suggests that many larval RGC t-types split up into multiple t-types during maturation, while other t-types ostensibly vanish (Kölsch et al., 2021). The described functional-anatomical-transcriptomic relationship we observed is therefore a snapshot of a marvelous system that accomplishes to both function and develop at the same time. A one-to-

one correspondence for the encoding of visual features and transcriptomic identity is probably too rigid in such a dynamic system. Along these lines, animals need to learn throughout their lifetime and adjust their behavioral responses dynamically to changing environments. This calls for flexible underlying circuits that can respond to the same visual stimulus with different responses based on situational context, inner state or individual experience. A system made up of rigid information channels solidified by differential gene expression for each ethologically relevant stimulus might not be suitable to a system that grows, transforms and learns over its lifetime.

4. References

Adolphs, R., 1999. Social cognition and the human brain. Trends Cogn. Sci. 3, 469–479. https://doi.org/10.1016/S1364-6613(99)01399-6

Ahrens, M.B., Orger, M.B., Robson, D.N., Li, J.M., Keller, P.J., 2013. Whole-brain functional imaging at cellular resolution using light-sheet microscopy. Nat. Methods 10, 413–420. https://doi.org/10.1038/nmeth.2434

Allison, T., Puce, A., McCarthy, G., 2000. Social perception from visual cues: role of the STS region. Trends Cogn. Sci. 4, 267–278. https://doi.org/10.1016/S1364-6613(00)01501-1

Anderson, D.J., 2016. Circuit modules linking internal states and social behaviour in flies and mice. Nat. Rev. Neurosci. 17, 692–704. https://doi.org/10.1038/nrn.2016.125

Anneser, L., Alcantara, I.C., Gemmer, A., Mirkes, K., Ryu, S., Schuman, E.M., 2020. The neuropeptide Pth2 dynamically senses others via mechanosensation. Nature 588, 653–657. https://doi.org/10.1038/s41586-020-2988-z

Antinucci, P., Folgueira, M., Bianco, I.H., 2019. Pretectal neurons control hunting behaviour. eLife 8, e48114. https://doi.org/10.7554/eLife.48114

Armstrong-Gold, C.E., Rieke, F., 2003. Bandpass Filtering at the Rod to Second-Order Cell Synapse in Salamander (Ambystoma tigrinum) Retina. J. Neurosci. 23, 3796–3806. https://doi.org/10.1523/JNEUROSCI.23-09-03796.2003

Avants, B.B., Tustison, N.J., Song, G., Cook, P.A., Klein, A., Gee, J.C., 2011. A reproducible evaluation of ANTs similarity metric performance in brain image registration. NeuroImage 54, 2033–2044. https://doi.org/10.1016/j.neuroimage.2010.09.025

Avitan, L., Pujic, Z., Mölter, J., McCullough, M., Zhu, S., Sun, B., Myhre, A.-E., Goodhill, G.J., 2020. Behavioral Signatures of a Developing Neural Code. Curr. Biol. 30, 3352-3363.e5. https://doi.org/10.1016/j.cub.2020.06.040

Báez-Mendoza, R., Mastrobattista, E.P., Wang, A.J., Williams, Z.M., 2021. Social agent identity cells in the prefrontal cortex of interacting groups of primates. Science 374, eabb4149. https://doi.org/10.1126/science.abb4149

Baier, H., Wullimann, M.F., 2021. Anatomy and function of retinorecipient arborization fields in zebrafish. J. Comp. Neurol. 529, 3454–3476. https://doi.org/10.1002/cne.25204

Bakken, T.E., Jorstad, N.L., Hu, Q., Lake, B.B., Tian, W., Kalmbach, B.E., Crow, M., Hodge, R.D., Krienen, F.M., Sorensen, S.A., Eggermont, J., Yao, Z., Aevermann, B.D., Aldridge, A.I., Bartlett, A., Bertagnolli, D., Casper, T., Castanon, R.G., Crichton, K., Daigle, T.L., Dalley, R., Dee, N., Dembrow, N., Diep, D., Ding, S.-L., Dong, W., Fang, R., Fischer, S., Goldman, M., Goldy, J., Graybuck, L.T., Herb, B.R., Hou, X., Kancherla, J., Kroll, M., Lathia, K., van Lew, B., Li, Y.E., Liu, C.S., Liu, H., Lucero, J.D., Mahurkar, A., McMillen, D., Miller, J.A., Moussa, M., Nery, J.R., Nicovich, P.R., Niu, S.-Y., Orvis, J., Osteen, J.K., Owen, S., Palmer, C.R., Pham, T., Plongthongkum, N., Poirion, O., Reed, N.M., Rimorin, C., Rivkin, A., Romanow, W.J., Sedeño-Cortés, A.E., Siletti, K., Somasundaram, S., Sulc, J., Tieu, M., Torkelson, A., Tung, H., Wang, X., Xie, F., Yanny, A.M., Zhang, R., Ament, S.A., Behrens, M.M., Bravo, H.C., Chun, J., Dobin, A., Gillis, J., Hertzano, R., Hof, P.R., Höllt, T., Horwitz, G.D., Keene, C.D., Kharchenko, P.V., Ko, A.L., Lelieveldt, B.P., Luo, C., Mukamel, E.A., Pinto-Duarte, A., Preissl, S., Regev, A., Ren, B., Scheuermann, R.H., Smith, K., Spain, W.J., White, O.R., Koch, C., Hawrylycz, M., Tasic, B., Macosko, E.Z., McCarroll, S.A., Ting, J.T., Zeng, H., Zhang, K., Feng, G., Ecker, J.R., Linnarsson, S., Lein, E.S., 2021. Comparative cellular analysis of motor cortex in human, marmoset and mouse. Nature 598, 111–119. https://doi.org/10.1038/s41586-021-03465-8

Bao, P., She, L., McGill, M., Tsao, D.Y., 2020. A map of object space in primate inferotemporal cortex. Nature 583, 103–108. https://doi.org/10.1038/s41586-020-2350-5

Barker, A.J., Baier, H., 2015. Sensorimotor Decision Making in the Zebrafish Tectum. Curr. Biol. 25, 2804–2814. https://doi.org/10.1016/j.cub.2015.09.055
Benarroch, E.E., 2015. Pulvinar: Associative role in cortical function and clinical correlations. Neurology 84, 738–747. https://doi.org/10.1212/WNL.0000000000001276
Ben-Tov, M., Donchin, O., Ben-Shahar, O., Segev, R., 2015. Pop-out in visual search of moving targets in the archer fish. Nat. Commun. 6, 6476. https://doi.org/10.1038/ncomms7476
Bergan, J.F., Ben-Shaul, Y., Dulac, C., 2014. Sex-specific processing of social cues in the medial amygdala. eLife 3, e02743. https://doi.org/10.7554/eLife.02743
Bergmann, K., Meza Santoscoy, P., Lygdas, K., Nikolaeva, Y., MacDonald, R.B., Cunliffe, V.T., Nikolaev, A., 2018. Imaging Neuronal Activity in the Optic Tectum of Late Stage Larval Zebrafish. J. Dev. Biol. 6, 6. https://doi.org/10.3390/jdb6010006
Bianco, I.H., Engert, F., 2015. Visuomotor Transformations Underlying Hunting Behavior in Zebrafish. Curr. Biol. 25, 831–846. https://doi.org/10.1016/j.cub.2015.01.042
Borst, A., Egelhaaf, M., 1989. Principles of visual motion detection. Trends Neurosci. 12, 297–306. https://doi.org/10.1016/0166-2236(89)90010-6
Bridge, H., Leopold, D.A., Bourne, J.A., 2016. Adaptive Pulvinar Circuitry Supports Visual Cognition. Trends Cogn. Sci. 20, 146–157. https://doi.org/10.1016/j.tics.2015.10.003
Bruzzone, M., Chiarello, E., Albanesi, M., Miletto Petrazzini, M.E., Megighian, A., Lodovichi, C., dal Maschio, M., 2021. Whole brain functional recordings at cellular resolution in zebrafish larvae with 3D scanning multiphoton microscopy. Sci. Rep. 11, 11048. https://doi.org/10.1038/s41598-021-90335-y
Bshary, R., Gingins, S., Vail, A.L., 2014. Social cognition in fishes. Trends Cogn. Sci. 18, 465–471. https://doi.org/10.1016/j.tics.2014.04.005
Bugeon, S., Duffield, J., Dipoppa, M., Ritoux, A., Prankerd, I., Nicoloutsopoulos, D., Orme, D., Shinn, M., Peng, H., Forrest, H., Viduolyte, A., Reddy, C.B., Isogai, Y., Carandini, M., Harris, K.D., 2022. A transcriptomic axis predicts state modulation of cortical interneurons. Nature 607, 330–338. https://doi.org/10.1038/s41586-022-04915-7
Burrill, J.D., Easter Jr., S.S., 1994. Development of the retinofugal projections in the embryonic and larval zebrafish (Brachydanio rerio). J. Comp. Neurol. 346, 583–600. https://doi.org/10.1002/cne.903460410
Byrne, R.W., 1996. Machiavellian intelligence. Evol. Anthropol. Issues News Rev. 5, 172–180. https://doi.org/10.1002/(SICI)1520-6505(1996)5:5<172::AID-EVAN6>3.0.CO;2-H
Cabrera-Álvarez, M.J., Swaney, W.T., Reader, S.M., 2017. Forebrain activation during social exposure in wild-type guppies. Physiol. Behav. 182, 107–113. https://doi.org/10.1016/j.physbeh.2017.10.012
Chen, K.H., Boettiger, A.N., Moffitt, J.R., Wang, S., Zhuang, X., 2015. Spatially resolved, highly multiplexed RNA profiling in single cells. Science 348, aaa6090. https://doi.org/10.1126/science.aaa6090
Chen, P., Hong, W., 2018. Neural Circuit Mechanisms of Social Behavior. Neuron 98, 16–30. https://doi.org/10.1016/j.neuron.2018.02.026
Choi, H.M.T., Schwarzkopf, M., Fornace, M.E., Acharya, A., Artavanis, G., Stegmaier, J., Cunha, A., Pierce, N.A., 2018. Third-generation in situ hybridization chain reaction: multiplexed, quantitative, sensitive, versatile, robust. Development 145, dev165753. https://doi.org/10.1242/dev.165753
Chow, D.M., Sinefeld, D., Kolkman, K.E., Ouzounov, D.G., Akbari, N., Tatarsky, R., Bass, A., Xu, C., Fetcho, J.R., 2020. Deep three-photon imaging of the brain in intact adult zebrafish. Nat. Methods 17, 605–608. https://doi.org/10.1038/s41592-020-0819-7
Cong, L., Wang, Z., Chai, Y., Hang, W., Shang, C., Yang, W., Bai, L., Du, J., Wang, K., Wen, Q., 2017. Rapid whole brain imaging of neural activity in freely behaving larval zebrafish (Danio rerio). eLife 6, e28158. https://doi.org/10.7554/eLife.28158

Cowley, B.R., Calhoun, A.J., Rangarajan, N., Pillow, J.W., Murthy, M., 2022. One-to-one mapping between deep network units and real neurons uncovers a visual population code for social behavior (preprint). Neuroscience. https://doi.org/10.1101/2022.07.18.500505
Cservenák, M., Szabó, É.R., Bodnár, I., Lékó, A., Palkovits, M., Nagy, G.M., Usdin, T.B., Dobolyi, A., 2013. Thalamic neuropeptide mediating the effects of nursing on lactation and maternal motivation. Psychoneuroendocrinology 38, 3070–3084. https://doi.org/10.1016/j.psyneuen.2013.09.004
Del Bene, F., Wyart, C., Robles, E., Tran, A., Looger, L., Scott, E.K., Isacoff, E.Y., Baier, H., 2010. Filtering of Visual Information in the Tectum by an Identified Neural Circuit. Science 330, 669–673. https://doi.org/10.1126/science.1192949
Denk, W., Strickler, J.H., Webb, W.W., 1990. Two-Photon Laser Scanning Fluorescence Microscopy. Science 248, 73–76. https://doi.org/10.1126/science.2321027
Dittrich, W.H., Troscianko, T., Lea, S.E.G., Morgan, D., 1996. Perception of Emotion from Dynamic Point-Light Displays Represented in Dance. Perception 25, 727–738. https://doi.org/10.1068/p250727
Dreosti, E., Lopes, G., Kampff, A., Wilson, S., 2015. Development of social behavior in young zebrafish. Front. Neural Circuits 9.
Dulac, C., Torello, A.T., 2003. Molecular detection of pheromone signals in mammals: from genes to behaviour. Nat. Rev. Neurosci. 4, 551–562. https://doi.org/10.1038/nrn1140
Dunbar, R.I.M., Shultz, S., 2007. Evolution in the Social Brain. Science 317, 1344–1347. https://doi.org/10.1126/science.1145463
Dunn, T.W., Gebhardt, C., Naumann, E.A., Riegler, C., Ahrens, M.B., Engert, F., Del Bene, F., 2016. Neural Circuits Underlying Visually Evoked Escapes in Larval Zebrafish. Neuron 89, 613–628. https://doi.org/10.1016/j.neuron.2015.12.021
Elwood, R.W., Stolzenberg, D.S., 2020. Flipping the parental switch: from killing to caring in male mammals. Anim. Behav. 165, 133–142. https://doi.org/10.1016/j.anbehav.2020.05.001
Engeszer, R.E., Da Barbiano, L.A., Ryan, M.J., Parichy, D.M., 2007. Timing and plasticity of shoaling behaviour in the zebrafish, Danio rerio. Anim. Behav. 74, 1269–1275. https://doi.org/10.1016/j.anbehav.2007.01.032
Engeszer, R.E., Ryan, M.J., Parichy, D.M., 2004. Learned Social Preference in Zebrafish. Curr. Biol. 14, 881–884. https://doi.org/10.1016/j.cub.2004.04.042
Euler, T., Haverkamp, S., Schubert, T., Baden, T., 2014. Retinal bipolar cells: elementary building blocks of vision. Nat. Rev. Neurosci. 15, 507–519. https://doi.org/10.1038/nrn3783
Ewert, J.-P., 1987. Neuroethology of releasing mechanisms: Prey-catching in toads. Behav. Brain Sci. 10, 337–368. https://doi.org/10.1017/S0140525X00023128
Fernandes, A.M., Mearns, D.S., Donovan, J.C., Larsch, J., Helmbrecht, T.O., Kölsch, Y., Laurell, E., Kawakami, K., dal Maschio, M., Baier, H., 2021. Neural circuitry for stimulus selection in the zebrafish visual system. Neuron 109, 805-822.e6. https://doi.org/10.1016/j.neuron.2020.12.002
Förster, D., Helmbrecht, T.O., Mearns, D.S., Jordan, L., Mokayes, N., Baier, H., 2020. Retinotectal circuitry of larval zebrafish is adapted to detection and pursuit of prey. eLife 9, e58596. https://doi.org/10.7554/eLife.58596
Franklin, T.B., Silva, B.A., Perova, Z., Marrone, L., Masferrer, M.E., Zhan, Y., Kaplan, A., Greetham, L., Verrechia, V., Halman, A., Pagella, S., Vyssotski, A.L., Illarionova, A., Grinevich, V., Branco, T., Gross, C.T., 2017. Prefrontal cortical control of a brainstem social behavior circuit. Nat. Neurosci. 20, 260–270. https://doi.org/10.1038/nn.4470
Gahtan, E., Tanger, P., Baier, H., 2005. Visual Prey Capture in Larval Zebrafish Is Controlled by Identified Reticulospinal Neurons Downstream of the Tectum. J. Neurosci. 25, 9294–9303. https://doi.org/10.1523/JNEUROSCI.2678-05.2005

Gellén, B., Zelena, D., Usdin, T.B., Dobolyi, Á., 2017. The parathyroid hormone 2 receptor participates in physiological and behavioral alterations of mother mice. Physiol. Behav. 181, 51–58. https://doi.org/10.1016/j.physbeh.2017.09.005

Geng, Y., Peterson, R.T., 2019. The zebrafish subcortical social brain as a model for studying social behavior disorders. Dis. Model. Mech. 12, dmm039446. https://doi.org/10.1242/dmm.039446

Goodson, J.L., 2005. The vertebrate social behavior network: Evolutionary themes and variations. Horm. Behav., Society for Behavioral Neuroendocrinology Annual Meeting Issue 2005 48, 11–22. https://doi.org/10.1016/j.yhbeh.2005.02.003

Grieve, K.L., Acuña, C., Cudeiro, J., 2000. The primate pulvinar nuclei: vision and action. Trends Neurosci. 23, 35–39. https://doi.org/10.1016/S0166-2236(99)01482-4

Grossman, Y.S., Fillinger, C., Manganaro, A., Voren, G., Waldman, R., Zou, T., Janssen, W.G., Kenny, P.J., Dumitriu, D., 2022. Structure and function differences in the prelimbic cortex to basolateral amygdala circuit mediate trait vulnerability in a novel model of acute social defeat stress in male mice. Neuropsychopharmacology 47, 788–799. https://doi.org/10.1038/s41386-021-01229-6

Hahn, J., Monavarfeshani, A., Qiao, M., Kao, A.H., Kölsch, Y., Kumar, A., Kunze, V.P., Rasys, A.M., Richardson, R., Wekselblatt, J.B., Baier, H., Lucas, R.J., Li, W., Meister, M., Trachtenberg, J.T., Yan, W., Peng, Y.-R., Sanes, J.R., Shekhar, K., 2023. Evolution of neuronal cell classes and types in the vertebrate retina. Nature 624, 415–424. https://doi.org/10.1038/s41586-023-06638-9

Hain, D., Gallego-Flores, T., Klinkmann, M., Macias, A., Ciirdaeva, E., Arends, A., Thum, C., Tushev, G., Kretschmer, F., Tosches, M.A., Laurent, G., 2022. Molecular diversity and evolution of neuron types in the amniote brain. Science 377, eabp8202. https://doi.org/10.1126/science.abp8202

Halpern, M., 1987. The Organization and Function of the Vomeronasal System.

Hampson, K.M., Turcotte, R., Miller, D.T., Kurokawa, K., Males, J.R., Ji, N., Booth, M.J., 2021. Adaptive optics for high-resolution imaging. Nat. Rev. Methods Primer 1, 1–26. https://doi.org/10.1038/s43586-021-00066-7

Hartline, H.K., 1938. The response of single optic nerve fibers of the vertebrate eye to illumination of the retina. Am. J. Physiol.-Leg. Content 121, 400–415. https://doi.org/10.1152/ajplegacy.1938.121.2.400

Hawken, M.J., Shapley, R.M., Grosof, D.H., 1996. Temporal-frequency selectivity in monkey visual cortex. Vis. Neurosci. 13, 477–492. https://doi.org/10.1017/S0952523800008154

Heap, L.A.L., Vanwalleghem, G., Thompson, A.W., Favre-Bulle, I.A., Scott, E.K., 2018. Luminance Changes Drive Directional Startle through a Thalamic Pathway. Neuron 99, 293-301.e4. https://doi.org/10.1016/j.neuron.2018.06.013

Helmbrecht, T.O., dal Maschio, M., Donovan, J.C., Koutsouli, S., Baier, H., 2018. Topography of a Visuomotor Transformation. Neuron 100, 1429-1445.e4. https://doi.org/10.1016/j.neuron.2018.10.021

Hennessy, M.B., Kaiser, S., Sachser, N., 2009. Social buffering of the stress response: Diversity, mechanisms, and functions. Front. Neuroendocrinol., Hormones & Social Behavior 30, 470–482. https://doi.org/10.1016/j.yfrne.2009.06.001

Hesse, J.K., Tsao, D.Y., 2020. The macaque face patch system: a turtle's underbelly for the brain. Nat. Rev. Neurosci. 21, 695–716. https://doi.org/10.1038/s41583-020-00393-w

Hindmarsh Sten, T., Li, R., Otopalik, A., Ruta, V., 2021. Sexual arousal gates visual processing during Drosophila courtship. Nature 595, 549–553. https://doi.org/10.1038/s41586-021-03714-w

Hinz, R.C., de Polavieja, G.G., 2017. Ontogeny of collective behavior reveals a simple attraction rule. Proc. Natl. Acad. Sci. 114, 2295–2300. https://doi.org/10.1073/pnas.1616926114

Hoopfer, E.D., Jung, Y., Inagaki, H.K., Rubin, G.M., Anderson, D.J., 2015. P1 interneurons promote a persistent internal state that enhances inter-male aggression in Drosophila. eLife 4, e11346. https://doi.org/10.7554/eLife.11346

Huang, K.-H., Rupprecht, P., Frank, T., Kawakami, K., Bouwmeester, T., Friedrich, R.W., 2020. A virtual reality system to analyze neural activity and behavior in adult zebrafish. Nat. Methods 17, 343–351. https://doi.org/10.1038/s41592-020-0759-2

Hubel, D.H., Wiesel, T.N., 1962. Receptive fields, binocular interaction and functional architecture in the cat's visual cortex. J. Physiol. 160, 106-154.2.

Johansson, G., 1973. Visual perception of biological motion and a model for its analysis. Percept. Psychophys. 14, 201–211. https://doi.org/10.3758/BF03212378

Kappel, J.M., Förster, D., Slangewal, K., Shainer, I., Svara, F., Donovan, J.C., Sherman, S., Januszewski, M., Baier, H., Larsch, J., 2022. Visual recognition of social signals by a tectothalamic neural circuit. Nature 608, 146–152. https://doi.org/10.1038/s41586-022-04925-5

Kato, S., Kaplan, H.S., Schrödel, T., Skora, S., Lindsay, T.H., Yemini, E., Lockery, S., Zimmer, M., 2015. Global Brain Dynamics Embed the Motor Command Sequence of Caenorhabditis elegans. Cell 163, 656–669. https://doi.org/10.1016/j.cell.2015.09.034

Katz, Y., Tunstrøm, K., Ioannou, C.C., Huepe, C., Couzin, I.D., 2011. Inferring the structure and dynamics of interactions in schooling fish. Proc. Natl. Acad. Sci. 108, 18720–18725. https://doi.org/10.1073/pnas.1107583108

Kawakami, K., Asakawa, K., Hibi, M., Itoh, M., Muto, A., Wada, H., 2016. Chapter Three - Gal4 Driver Transgenic Zebrafish: Powerful Tools to Study Developmental Biology, Organogenesis, and Neuroscience, in: Foulkes, N.S. (Ed.), Advances in Genetics, Genetics, Genomics and Fish Phenomics. Academic Press, pp. 65–87. https://doi.org/10.1016/bs.adgen.2016.04.002

Keller, D., Láng, T., Cservenák, M., Puska, G., Barna, J., Csillag, V., Farkas, I., Zelena, D., Dóra, F., Küppers, S., Barteczko, L., Usdin, T.B., Palkovits, M., Hasan, M.T., Grinevich, V., Dobolyi, A., 2022. A thalamo-preoptic pathway promotes social grooming in rodents. Curr. Biol. 32, 4593-4606.e8. https://doi.org/10.1016/j.cub.2022.08.062

Kelly, A.M., 2022. A consideration of brain networks modulating social behavior. Horm. Behav. 141, 105138. https://doi.org/10.1016/j.yhbeh.2022.105138

Kim, D.H., Kim, J., Marques, J.C., Grama, A., Hildebrand, D.G.C., Gu, W., Li, J.M., Robson, D.N., 2017. Pan-neuronal calcium imaging with cellular resolution in freely swimming zebrafish. Nat. Methods 14, 1107–1114. https://doi.org/10.1038/nmeth.4429

Klein, S., Staring, M., Murphy, K., Viergever, M.A., Pluim, J.P.W., 2010. elastix: A Toolbox for Intensity-Based Medical Image Registration. IEEE Trans. Med. Imaging 29, 196–205. https://doi.org/10.1109/TMI.2009.2035616

Knudsen, E.I., 2018. Neural Circuits That Mediate Selective Attention: A Comparative Perspective. Trends Neurosci. 41, 789–805. https://doi.org/10.1016/j.tins.2018.06.006

Kölsch, Y., Hahn, J., Sappington, A., Stemmer, M., Fernandes, A.M., Helmbrecht, T.O., Lele, S., Butrus, S., Laurell, E., Arnold-Ammer, I., Shekhar, K., Sanes, J.R., Baier, H., 2021. Molecular classification of zebrafish retinal ganglion cells links genes to cell types to behavior. Neuron 109, 645-662.e9. https://doi.org/10.1016/j.neuron.2020.12.003

Krueger, F., Barbey, A.K., Grafman, J., 2009. The medial prefrontal cortex mediates social event knowledge. Trends Cogn. Sci. 13, 103–109. https://doi.org/10.1016/j.tics.2008.12.005

Kubo, F., Hablitzel, B., Dal Maschio, M., Driever, W., Baier, H., Arrenberg, A.B., 2014. Functional Architecture of an Optic Flow-Responsive Area that Drives Horizontal Eye Movements in Zebrafish. Neuron 81, 1344–1359. https://doi.org/10.1016/j.neuron.2014.02.043

Kunst, M., Laurell, E., Mokayes, N., Kramer, A., Kubo, F., Fernandes, A.M., Förster, D., Dal Maschio, M., Baier, H., 2019. A Cellular-Resolution Atlas of the Larval Zebrafish Brain. Neuron 103, 21-38.e5. https://doi.org/10.1016/j.neuron.2019.04.034

Larsch, J., Baier, H., 2018. Biological Motion as an Innate Perceptual Mechanism Driving Social Affiliation. Curr. Biol. 28, 3523-3532.e4. https://doi.org/10.1016/j.cub.2018.09.014

Li, Y., Mathis, A., Grewe, B.F., Osterhout, J.A., Ahanonu, B., Schnitzer, M.J., Murthy, V.N., Dulac, C., 2017. Neuronal Representation of Social Information in the Medial Amygdala of Awake Behaving Mice. Cell 171, 1176-1190.e17. https://doi.org/10.1016/j.cell.2017.10.015
Li, Y., Meister, M., 2022. Functional Cell Types in the Mouse Superior Colliculus (preprint). Neuroscience. https://doi.org/10.1101/2022.04.01.486789
Lin, D., Boyle, M.P., Dollar, P., Lee, H., Lein, E.S., Perona, P., Anderson, D.J., 2011. Functional identification of an aggression locus in the mouse hypothalamus. Nature 470, 221–226. https://doi.org/10.1038/nature09736
Liu, M., Kim, D.-W., Zeng, H., Anderson, D.J., 2022. Make war not love: The neural substrate underlying a state-dependent switch in female social behavior. Neuron 110, 841-856.e6. https://doi.org/10.1016/j.neuron.2021.12.002
Lopes, G., Monteiro, P., 2021. New Open-Source Tools: Using Bonsai for Behavioral Tracking and Closed-Loop Experiments. Front. Behav. Neurosci. 15.
Lovett-Barron, M., Andalman, A.S., Allen, W.E., Vesuna, S., Kauvar, I., Burns, V.M., Deisseroth, K., 2017. Ancestral Circuits for the Coordinated Modulation of Brain State. Cell 171, 1411-1423.e17. https://doi.org/10.1016/j.cell.2017.10.021
Lu, R., Liang, Y., Meng, G., Zhou, P., Svoboda, K., Paninski, L., Ji, N., 2020. Rapid mesoscale volumetric imaging of neural activity with synaptic resolution. Nat. Methods 17, 291–294. https://doi.org/10.1038/s41592-020-0760-9
Maior, R.S., Hori, E., Tomaz, C., Ono, T., Nishijo, H., 2010. The monkey pulvinar neurons differentially respond to emotional expressions of human faces. Behav. Brain Res. 215, 129–135. https://doi.org/10.1016/j.bbr.2010.07.009
Marquart, G.D., Tabor, K.M., Horstick, E.J., Brown, M., Geoca, A.K., Polys, N.F., Nogare, D.D., Burgess, H.A., 2017. High-precision registration between zebrafish brain atlases using symmetric diffeomorphic normalization. GigaScience 6, gix056. https://doi.org/10.1093/gigascience/gix056
Martin, A., Babbitt, A., Pickens, A.G., Pickett, B.E., Hill, J.T., Suli, A., 2022. Single-Cell RNA Sequencing Characterizes the Molecular Heterogeneity of the Larval Zebrafish Optic Tectum. Front. Mol. Neurosci. 15.
Maruska, K.P., Zhang, A., Neboori, A., Fernald, R.D., 2013. Social Opportunity Causes Rapid Transcriptional Changes in the Social Behaviour Network of the Brain in an African Cichlid Fish. J. Neuroendocrinol. 25, 145–157. https://doi.org/10.1111/j.1365-2826.2012.02382.x
Mather, G., Murdoch, L., 1997. Gender discrimination in biological motion displays based on dynamic cues. Proc. R. Soc. Lond. B Biol. Sci. 258, 273–279. https://doi.org/10.1098/rspb.1994.0173
Matthews, G.A., Tye, K.M., 2019. Neural mechanisms of social homeostasis. Ann. N. Y. Acad. Sci. 1457, 5–25. https://doi.org/10.1111/nyas.14016
Milne, E., Grafman, J., 2001. Ventromedial Prefrontal Cortex Lesions in Humans Eliminate Implicit Gender Stereotyping. J. Neurosci. 21, RC150–RC150. https://doi.org/10.1523/JNEUROSCI.21-12-j0001.2001
Mueller, T., 2012. What is the Thalamus in Zebrafish? Front. Neurosci. 6.
Münch, T.A., da Silveira, R.A., Siegert, S., Viney, T.J., Awatramani, G.B., Roska, B., 2009. Approach sensitivity in the retina processed by a multifunctional neural circuit. Nat. Neurosci. 12, 1308–1316. https://doi.org/10.1038/nn.2389
Murugan, M., Jang, H.J., Park, M., Miller, E.M., Cox, J., Taliaferro, J.P., Parker, N.F., Bhave, V., Hur, H., Liang, Y., Nectow, A.R., Pillow, J.W., Witten, I.B., 2017. Combined Social and Spatial Coding in a Descending Projection from the Prefrontal Cortex. Cell 171, 1663-1677.e16. https://doi.org/10.1016/j.cell.2017.11.002
Muto, A., Ohkura, M., Abe, G., Nakai, J., Kawakami, K., 2013. Real-Time Visualization of Neuronal Activity during Perception. Curr. Biol. 23, 307–311. https://doi.org/10.1016/j.cub.2012.12.040

Nagpal, J., Herget, U., Choi, M.K., Ryu, S., 2019. Anatomy, development, and plasticity of the neurosecretory hypothalamus in zebrafish. Cell Tissue Res. 375, 5–22. https://doi.org/10.1007/s00441-018-2900-4

Naumann, E.A., Fitzgerald, J.E., Dunn, T.W., Rihel, J., Sompolinsky, H., Engert, F., 2016. From Whole-Brain Data to Functional Circuit Models: The Zebrafish Optomotor Response. Cell 167, 947-960.e20. https://doi.org/10.1016/j.cell.2016.10.019

Neri, P., 2012. Feature binding in zebrafish. Anim. Behav. 84, 485–493. https://doi.org/10.1016/j.anbehav.2012.06.005

Neri, P., Morrone, M.C., Burr, D.C., 1998. Seeing biological motion. Nature 395, 894–896. https://doi.org/10.1038/27661

Nevin, L.M., Robles, E., Baier, H., Scott, E.K., 2010. Focusing on optic tectum circuitry through the lens of genetics. BMC Biol. 8, 126. https://doi.org/10.1186/1741-7007-8-126

Newman, S.W., 1999. The Medial Extended Amygdala in Male Reproductive Behavior A Node in the Mammalian Social Behavior Network. Ann. N. Y. Acad. Sci. 877, 242–257. https://doi.org/10.1111/j.1749-6632.1999.tb09271.x

Nguyen, M.N., Hori, E., Matsumoto, J., Tran, A.H., Ono, T., Nishijo, H., 2013. Neuronal responses to face-like stimuli in the monkey pulvinar. Eur. J. Neurosci. 37, 35–51. https://doi.org/10.1111/ejn.12020

Niell, C.M., Smith, S.J., 2005. Functional Imaging Reveals Rapid Development of Visual Response Properties in the Zebrafish Tectum. Neuron 45, 941–951. https://doi.org/10.1016/j.neuron.2005.01.047

Northcutt, R.G., 2006. Connections of the lateral and medial divisions of the goldfish telencephalic pallium. J. Comp. Neurol. 494, 903–943. https://doi.org/10.1002/cne.20853

O'Connell, L.A., Hofmann, H.A., 2012. Evolution of a Vertebrate Social Decision-Making Network. Science 336, 1154–1157. https://doi.org/10.1126/science.1218889

Oldfield, C.S., Grossrubatscher, I., Chávez, M., Hoagland, A., Huth, A.R., Carroll, E.C., Prendergast, A., Qu, T., Gallant, J.L., Wyart, C., Isacoff, E.Y., 2020. Experience, circuit dynamics, and forebrain recruitment in larval zebrafish prey capture. eLife 9, e56619. https://doi.org/10.7554/eLife.56619

Ölveczky, B.P., Baccus, S.A., Meister, M., 2003. Segregation of object and background motion in the retina. Nature 423, 401–408. https://doi.org/10.1038/nature01652

Pandey, S., Moyer, A.J., Thyme, S.B., 2023. A single-cell transcriptome atlas of the maturing zebrafish telencephalon. Genome Res. 33, 658–671. https://doi.org/10.1101/gr.277278.122

Panser, K., Tirian, L., Schulze, F., Villalba, S., Jefferis, G.S.X.E., Bühler, K., Straw, A.D., 2016. Automatic Segmentation of Drosophila Neural Compartments Using GAL4 Expression Data Reveals Novel Visual Pathways. Curr. Biol. 26, 1943–1954. https://doi.org/10.1016/j.cub.2016.05.052

Peng, H., Xie, P., Liu, L., Kuang, X., Wang, Yimin, Qu, L., Gong, H., Jiang, S., Li, A., Ruan, Z., Ding, L., Yao, Z., Chen, C., Chen, M., Daigle, T.L., Dalley, R., Ding, Z., Duan, Y., Feiner, A., He, P., Hill, C., Hirokawa, K.E., Hong, G., Huang, L., Kebede, S., Kuo, H.-C., Larsen, R., Lesnar, P., Li, L., Li, Q., Li, X., Li, Yaoyao, Li, Yuanyuan, Liu, A., Lu, D., Mok, S., Ng, L., Nguyen, T.N., Ouyang, Q., Pan, J., Shen, E., Song, Y., Sunkin, S.M., Tasic, B., Veldman, M.B., Wakeman, W., Wan, W., Wang, P., Wang, Q., Wang, T., Wang, Yaping, Xiong, F., Xiong, W., Xu, W., Ye, M., Yin, L., Yu, Y., Yuan, Jia, Yuan, Jing, Yun, Z., Zeng, S., Zhang, S., Zhao, S., Zhao, Z., Zhou, Z., Huang, Z.J., Esposito, L., Hawrylycz, M.J., Sorensen, S.A., Yang, X.W., Zheng, Y., Gu, Z., Xie, W., Koch, C., Luo, Q., Harris, J.A., Wang, Yun, Zeng, H., 2021. Morphological diversity of single neurons in molecularly defined cell types. Nature 598, 174–181. https://doi.org/10.1038/s41586-021-03941-1

Portugues, R., Feierstein, C.E., Engert, F., Orger, M.B., 2014. Whole-Brain Activity Maps Reveal Stereotyped, Distributed Networks for Visuomotor Behavior. Neuron 81, 1328–1343. https://doi.org/10.1016/j.neuron.2014.01.019

Raj, B., Wagner, D.E., McKenna, A., Pandey, S., Klein, A.M., Shendure, J., Gagnon, J.A., Schier, A.F., 2018. Simultaneous single-cell profiling of lineages and cell types in the vertebrate brain. Nat. Biotechnol. 36, 442–450. https://doi.org/10.1038/nbt.4103

Randlett, O., Wee, C.L., Naumann, E.A., Nnaemeka, O., Schoppik, D., Fitzgerald, J.E., Portugues, R., Lacoste, A.M.B., Riegler, C., Engert, F., Schier, A.F., 2015. Whole-brain activity mapping onto a zebrafish brain atlas. Nat. Methods 12, 1039–1046. https://doi.org/10.1038/nmeth.3581

Regolin, L., Tommasi, L., Vallortigara, G., 2000. Visual perception of biological motion in newly hatched chicks as revealed by an imprinting procedure. Anim. Cogn. 3, 53–60. https://doi.org/10.1007/s100710050050

Ribeiro, I.M.A., Drews, M., Bahl, A., Machacek, C., Borst, A., Dickson, B.J., 2018. Visual Projection Neurons Mediating Directed Courtship in Drosophila. Cell 174, 607-621.e18. https://doi.org/10.1016/j.cell.2018.06.020

Robles, E., Laurell, E., Baier, H., 2014. The Retinal Projectome Reveals Brain-Area-Specific Visual Representations Generated by Ganglion Cell Diversity. Curr. Biol. 24, 2085–2096. https://doi.org/10.1016/j.cub.2014.07.080

Rohlfing, T., Maurer, C.R., 2003. Nonrigid image registration in shared-memory multiprocessor environments with application to brains, breasts, and bees. IEEE Trans. Inf. Technol. Biomed. 7, 16–25. https://doi.org/10.1109/TITB.2003.808506

Romero-Ferrero, F., Bergomi, M.G., Hinz, R.C., Heras, F.J.H., de Polavieja, G.G., 2019. idtracker.ai: tracking all individuals in small or large collectives of unmarked animals. Nat. Methods 16, 179–182. https://doi.org/10.1038/s41592-018-0295-5

Scala, F., Kobak, D., Bernabucci, M., Bernaerts, Y., Cadwell, C.R., Castro, J.R., Hartmanis, L., Jiang, X., Laturnus, S., Miranda, E., Mulherkar, S., Tan, Z.H., Yao, Z., Zeng, H., Sandberg, R., Berens, P., Tolias, A.S., 2021. Phenotypic variation of transcriptomic cell types in mouse motor cortex. Nature 598, 144–150. https://doi.org/10.1038/s41586-020-2907-3

Scott, E., Baier, H., 2009. The cellular architecture of the larval zebrafish tectum, as revealed by Gal4 enhancer trap lines. Front. Neural Circuits 3.

Semmelhack, J.L., Donovan, J.C., Thiele, T.R., Kuehn, E., Laurell, E., Baier, H., 2014. A dedicated visual pathway for prey detection in larval zebrafish. eLife 3, e04878. https://doi.org/10.7554/eLife.04878

Shainer, I., Kuehn, E., Laurell, E., Al Kassar, M., Mokayes, N., Sherman, S., Larsch, J., Kunst, M., Baier, H., 2023. A single-cell resolution gene expression atlas of the larval zebrafish brain. Sci. Adv. 9, eade9909. https://doi.org/10.1126/sciadv.ade9909

Sherman, S., Kawakami, K., Baier, H., 2021. Retinal input influences pace of neurogenesis but not cell-type configuration of the visual forebrain. https://doi.org/10.1101/2021.11.15.468630

Sherrington, C.S., 1906. Observations on the scratch-reflex in the spinal dog. J. Physiol. 34, 1–50. https://doi.org/10.1113/jphysiol.1906.sp001139

Shinozuka, K., Watanabe, S., 2004. Effects of telencephalic ablation on shoaling behavior in goldfish. Physiol. Behav. 81, 141–148. https://doi.org/10.1016/j.physbeh.2004.01.005

Skocek, O., Nöbauer, T., Weilguny, L., Martínez Traub, F., Xia, C.N., Molodtsov, M.I., Grama, A., Yamagata, M., Aharoni, D., Cox, D.D., Golshani, P., Vaziri, A., 2018. High-speed volumetric imaging of neuronal activity in freely moving rodents. Nat. Methods 15, 429–432. https://doi.org/10.1038/s41592-018-0008-0

Stednitz, S.J., McDermott, E.M., Ncube, D., Tallafuss, A., Eisen, J.S., Washbourne, P., 2018. Forebrain Control of Behaviorally Driven Social Orienting in Zebrafish. Curr. Biol. 28, 2445-2451.e3. https://doi.org/10.1016/j.cub.2018.06.016

Striedter, G.F., 1990. The Diencephalon of the Channel Catfish, Ictalurus punctatus. Brain. Behav. Evol. 36, 355–377. https://doi.org/10.1159/000115319

Stuermer, C.A., 1988. Retinotopic organization of the developing retinotectal projection in the zebrafish embryo. J. Neurosci. 8, 4513–4530. https://doi.org/10.1523/JNEUROSCI.08-12-04513.1988

Suryadi, Cheng, R.-K., Jesuthasan, S., Chew, L.Y., 2020. Percolation in the resting zebrafish habenula. https://doi.org/10.1101/481358
Tambalo, M., Mitter, R., Wilkinson, D.G., 2020. A single cell transcriptome atlas of the developing zebrafish hindbrain. Development 147, dev184143. https://doi.org/10.1242/dev.184143
Temizer, I., Donovan, J.C., Baier, H., Semmelhack, J.L., 2015. A Visual Pathway for Looming-Evoked Escape in Larval Zebrafish. Curr. Biol. 25, 1823–1834. https://doi.org/10.1016/j.cub.2015.06.002
Tosches, M.A., Yamawaki, T.M., Naumann, R.K., Jacobi, A.A., Tushev, G., Laurent, G., 2018. Evolution of pallium, hippocampus, and cortical cell types revealed by single-cell transcriptomics in reptiles. Science 360, 881–888. https://doi.org/10.1126/science.aar4237
Tsao, D.Y., Freiwald, W.A., Knutsen, T.A., Mandeville, J.B., Tootell, R.B.H., 2003. Faces and objects in macaque cerebral cortex. Nat. Neurosci. 6, 989–995. https://doi.org/10.1038/nn1111
Tsao, D.Y., Freiwald, W.A., Tootell, R.B.H., Livingstone, M.S., 2006. A Cortical Region Consisting Entirely of Face-Selective Cells. Science 311, 670–674. https://doi.org/10.1126/science.1119983
Venet, L., Pati, S., Yushkevich, P., Bakas, S., 2019. Accurate and Robust Alignment of Variable-stained Histologic Images Using a General-purpose Greedy Diffeomorphic Registration Tool. https://doi.org/10.48550/arXiv.1904.11929
Wang, F., Flanagan, J., Su, N., Wang, L.-C., Bui, S., Nielson, A., Wu, X., Vo, H.-T., Ma, X.-J., Luo, Y., 2012. RNAscope: A Novel in Situ RNA Analysis Platform for Formalin-Fixed, Paraffin-Embedded Tissues. J. Mol. Diagn. 14, 22–29. https://doi.org/10.1016/j.jmoldx.2011.08.002
Wang, K., Hinz, J., Haikala, V., Reiff, D.F., Arrenberg, A.B., 2019. Selective processing of all rotational and translational optic flow directions in the zebrafish pretectum and tectum. BMC Biol. 17, 29. https://doi.org/10.1186/s12915-019-0648-2
Wertheimer, M., 1912. Experimentelle Studien uber das Sehen von Bewegung. Z. Psychol. 61, 161–165.
Wulliman, M.F., Rupp, B., Reichert, H., 2012. Neuroanatomy of the Zebrafish Brain: A Topological Atlas. Birkhäuser.
Wullimann, M.F., Mueller, T., 2004. Teleostean and mammalian forebrains contrasted: Evidence from genes to behavior. J. Comp. Neurol. 475, 143–162. https://doi.org/10.1002/cne.20183
Yoshimatsu, T., Bartel, P., Schröder, C., Janiak, F.K., St-Pierre, F., Berens, P., Baden, T., 2021. Ancestral circuits for vertebrate color vision emerge at the first retinal synapse. Sci. Adv. 7, eabj6815. https://doi.org/10.1126/sciadv.abj6815
Zhang, B., Yao, Y., Zhang, H., Kawakami, K., Du, J., 2017. Left Habenula Mediates Light-Preference Behavior in Zebrafish via an Asymmetrical Visual Pathway. Neuron 93, 914-928.e4. https://doi.org/10.1016/j.neuron.2017.01.011
Zhang, Y., Huang, R., Nörenberg, W., Arrenberg, A.B., 2022. A robust receptive field code for optic flow detection and decomposition during self-motion. Curr. Biol. 32, 2505-2516.e8. https://doi.org/10.1016/j.cub.2022.04.048
Zhao, Z., Zeng, F., Wang, H., Wu, R., Chen, Liping, Wu, Y., Li, S., Shao, J., Wang, Y., Wu, J., Feng, Z., Gao, W., Hu, Y., Wang, A., Cheng, H., Zhang, J., Chen, Liangyi, Wu, H., 2022. Encoding of social novelty by sparse GABAergic neural ensembles in the prelimbic cortex. Sci. Adv. 8, eabo4884. https://doi.org/10.1126/sciadv.abo4884
Zong, W., Obenhaus, H.A., Skytøen, E.R., Eneqvist, H., de Jong, N.L., Vale, R., Jorge, M.R., Moser, M.-B., Moser, E.I., 2022. Large-scale two-photon calcium imaging in freely moving mice. Cell 185, 1240-1256.e30. https://doi.org/10.1016/j.cell.2022.02.017

4. Acknowledgements

I would like to express my deep gratitude to the people that helped me learn, grow and complete this thesis in the last 5 years.
First, thank you Marco Sr, Marco Jr., Miguel and Thomas for all the support getting started in the lab. A big shout-out to all the Baier lab PhD students past and present during my time. Duncan, I miss our conversations. Lisa & Lukas, you guys really elevated the last chapter of my PhD. Ash, thank you for your throughout the years. Martin, for playdates.
Trace, I enjoyed sharing an office and lots of laughs with you. Joe, for so many ideas, planking and metal. Manuel, the best climbing partner I have had. Mariam, for all the laughs in the kitchen. Greg, for a short, good run as office mates, and all the podcasts. Swantje, for exchanging parent ordeal stories. Enrico, for lots of support, music and quiz. Irene, for wet lab support and a little bit of boarisch in the institute. Karin, Anne, thank you for helping out in dire situations. Drago, for fun banter and future advice. Fluffable, for Killing In The Name Of.

Thank you Axel and Benjamin for your time and good advice and making my TAC meetings so enjoyable.

Katja, you were the best first Master's student I could have ever had. Thank you for joining team social and contributing with your great ideas and hard work.
Inbal, I learned so much from you. Your dedication, work ethic and brilliance is just impressive. Thank you for letting me join your project and letting me grow. I am proud how far we have come.

Herwig, you gave me all the freedom I needed during this time. Thank you for keeping track of the greater goals and sharpening spoken words, texts and figures. You always supported my decision to start a family as a PhD student and acknowledged the underlying challenges. I am very grateful for that.

Johannes, thank you for this unique experience. Certainly, you have shaped the way I do research with your logic, creativity, ingenuity. I will never forget these intense last months before submission, and re-submission. I hope that many more young researchers will have the chance to benefit from your mentoring.

∞

I am very grateful to my parents, siblings and broader family that fully supported me and always believed in me. Thank you Susanne, Jürgen, Eva, Daniel & Anna.

Taavi & Viljo, if you can read this, DON'T DO A PHD!!! Do something useful with your time, like gardening or woodworking. Daddy loves you.

Sofia, you have had my back in during all challenging times. Thank you for starting the family adventure with me. Thank you for listening. Thank you for being there for me. Thank you for believing in me and supporting my dream. I love you.

5. Appendices

5.1 Declaration of author contributions

Positional information drives distinct traits in transcriptomically identified neuronal types

Inbal Shainer*, **Johannes M. Kappel***, Eva Laurell, Joseph C. Donovan, Martin Winfried Schneider, Enrico Kuehn, Irene Arnold-Ammer, Manuel Stemmer, Johannes Larsch, Herwig Baier

*These authors contributed equally to this work.

J.M.K. and I.S. performed functional two-photon imaging experiment. J.M.K. and I.S. performed registration of two-photon and HCR data. I.S. and E.K. performed HCR staining and imaging. I.S. performed scRNAseq and analyzed the data. J.C.D. advised on imaging data analysis. J.L. and M.W.S. performed pilot behavior experiments. J.M.K. analyzed functional imaging data. M.S. designed CRISPR constructs. I.A.A. constructed plasmids. I.S. and E.L. performed sparse labeling of neurons. E.L. performed neuronal tracings. I.S., J.M.K. and H.B. interpreted the data. I.S., J.M.K. and H.B. wrote the paper with input from J.L. All of the authors reviewed and edited the manuscript. H.B. supervised the project.

Visual recognition of social signals by a tectothalamic neural circuit

Johannes M. Kappel, Dominique Förster, Katja Slangewal, Inbal Shainer, Fabian Svara, Joseph C. Donovan, Shachar Sherman, Michał Januszewski, Herwig Baier* & Johannes Larsch*

*Corresponding authors

J.M.K. and K.S. performed two-photon imaging experiments. J.M.K. performed laser ablations, registration of two-photon and HCR data. M.J. segmented the EM volume with FFNs. D.F. proofread and traced presegmented EM data. I.S. performed HCR staining and imaging. F.S. generated the EM data and performed EM brain area registration. S.S. performed pilot HCR in situ experiments in juvenile fish. J.C.D. helped with the two-photon hardware and remote focusing, and advised on

microscopy and analysis. J.L. performed behavior experiments, transgenesis and brain area segmentation. J.M.K., K.S., D.F. and J.L. analyzed the data. J.M.K., K.S., D.F., H.B. and J.L. interpreted the data. J.M.K., D.F., H.B. and J.L. wrote the paper with input from all of the authors. All of the authors reviewed and edited the manuscript. H.B. and J.L. supervised the project.

5.2 Permissions

All figures are reproduced with permission.

5.3 List of publications

Shainer, I.*, **Kappel, J. M.***, Laurell, E., Donovan, J. C., Schneider, M., Kuehn, E., Arnold-Ammer, I., Stemmer, M., Larsch, L., Baier, H. (2023) '*Positional information drives distinct traits in transcriptomically identified neuronal types*', submitted
* These authors contributed equally to this work.

Kappel, J. M., Förster, D., Slangewal, K., Shainer, I., Svara, F., Donovan, J.C., Sherman, S., Januszewski, M., Baier, H., Larsch, J. (2022) '*Visual recognition of social signals by a tectothalamic neural circuit*', Nature, 608(7912), pp. 146-152.

Volkenhoff, A., Hirrlinger, J., **Kappel, J. M.**, Klämbt, C., Schirmeier, S. (2018) '*Live imaging using a FRET glucose sensor reveals glucose delivery to all cell types in the Drosophila brain', Journal of Insect Physiology*, 106, pp. 55–64.